UNIVERSITY OF SÃO PAULO
SCHOOL OF ENGINEERING

Barbara Pozzan dos Santos Duarte

# One-dimensional hydrodynamic modeling of reservoirs and the impact of climate change scenarios over their thermal behavior

São Paulo

2022

BARBARA POZZAN DOS SANTOS DUARTE

# One-dimensional hydrodynamic modeling of reservoirs and the impact of climate change scenarios over their thermal behavior

**Revised Version**

Dissertation presented to the School of Engineering of the University of São Paulo to obtain the degree of Master of Science.

Concentration area: Civil Engineering

Advisor: Prof. Dr. José Carlos de Melo Bernardino

São Paulo

2022

Este exemplar foi revisado e corrigido em relação à versão original, sob responsabilidade única do autor e com a anuência de seu orientador.

São Paulo,_____de_____de _____

Assinatura do autor: _____

Assinatura do orientador: _____

Catalogação-na-publicação

Duarte, Barbara Pozzan dos Santos

One-dimensional hydrodynamic modeling of reservoirs and the impact of climate change scenarios over their thermal behavior / B. P. S. Duarte -- versão corr. -- São Paulo, 2022.

157 p.

Dissertação (Mestrado) - Escola Politécnica da Universidade de São Paulo. Departamento de Engenharia de Hidráulica e Ambiental.

1.Reservatórios 2.Hidrodinâmica dos Lagos 3.Modelagem Computacional 4.Mudanças Climáticas I.Universidade de São Paulo. Escola Politécnica. Departamento de Engenharia de Hidráulica e Ambiental II.t.

# ACKNOLEDMENTS

I begin by thanking my family for all the opportunities I was given and all the support I received during my studies, as they endured endless (but informative) lectures and inspired me to follow through any difficulties. A special acknowledgement to my mother Geanete, my father Rogério and my sisters Beatriz e Mariana, who share their lives with me.

Most of my gratitude to my grandmas Berta and Julia, who, even though are not here to share this moment with me, have taught me so much and will always be remembered with all my love.

I would also like to thank my professor, José Rodolfo Scarati Martins, for believing in me from the beginning, supporting me during the whole process and always inspiring me to aim higher. Thank you for being an inspiration as teacher, a professional and a friend, when I needed. I would like to acknowledge my advisor Professor José Carlos de Melo Bernardino, who always helped me during this process, made me feel supported and, mainly, trusted my work in every moment. Thank you so much.

I extend my gratitude to all my friends, who have always been there for me when I needed, sharing with me good and bad moments and helping me navigate life in a lighter note. Among many who are so special to me, I would like to highlight the ones who made my Master's experience such an amazing path: Laís, Ariel, Maria Cristina, Fábio F.N. and Fábio P. Thank you all for the advices, the patience and the moments we shared.

I also take this opportunity to acknowledge all the infrastructure, faculty and staff at the Polytechnic School that collaborated with this work. I highlight the faculty from the Environmental Engineering course, - who helped me from the beginning as a Pre-Master student -, the collaborators Wandrea (who is always helpful and caring), Fábio Campos from LabSan, and the entire team of the Hydraulic Technology Centre.

This study was financed in part by the Coordenação de Aperfeiçoamento de Pessoal de Nível Superior - Brasil (CAPES) - Finance Code 001, Fundação Centro Tecnológico de Hidráulica – FCTH. Gratitude to ICMBIO and colleagues at MOMA-SE.

# EVALUATION SHEET

Name: DUARTE, Barbara Pozzan dos Santos

Title: One-dimensional hydrodynamic modeling of reservoirs and the impact of climate change scenarios over their thermal behavior

Dissertation presented to the Polytechnic School at Universidade de São Paulo (USP) to obtain the degree of Master of Science.

Approved in:

Examining Board

Prof. Dr. _____

Institute: _____

Decision: _____

Prof. Dr. _____

Institute: _____

Decision: _____

Prof. Dr. _____

Institute: _____

Decision: _____

# ABSTRACT

DUARTE, B. P. S. **One-dimensional hydrodynamic modeling of reservoirs and the impact of climate change scenarios over their thermal behavior.** 2022. Thesis (Master degree) – School of Engineering. University of São Paulo, São Paulo, 2022.

The occurrence of stratification and mixing events determines the thermal regime of lakes and reservoirs, influencing their physical, chemical, and biological characteristics. The frequency and duration of these events are determined by local atmospheric conditions, the morphology of the lake basin and the presence of in and outflows. Small-tropical lakes are essential to the development of many cities due to their multiple uses. However, studies about these environments are still scarce and restricted. In this context, this work aims to investigate the thermal behavior representation of a small-polymictic-tropical reservoir with a one-dimensional mathematical model and to assess the impacts of climate change scenarios over this behavior. The case study was focused on the Hedberg Dam, a 0.23 km²-4.5m depth pond, built in the beginnings of the 19th century, located about 90 km from Sao Paulo city, in Brazil. Its hydrological catchment area is partially protected by the Floresta Nacional de Ipanema, with sparse urban infrastructure and intense agricultural and pasture occupations. The mathematical modeling software applied was the General Lake Model (GLM), a one-dimensional hydrodynamic model, which uses a deterministic, mechanistic, time-dependent and numerical solving approach. With hourly time-steps, the model used morphology characteristics, atmospheric variables and inflow as input data. High-frequency thermal sensor data were used for the model calibration and validation, performed during the years 2017 and 2020. The results were considered reliable, since the model satisfactorily represents daily and seasonal patterns observed in the Hedberg Dam. For the climate change scenarios, the Eta regional climate model was used, with a 20 km spatial resolution. The chosen scenarios were the RCP 4.5 (optimistic) and RCP 8.5 (pessimistic), proposed by the IPCC, which indicate the increase in the mean global temperature of 1.8°C and 3.6°C, respectively, by the end of the century. The scenarios were simulated between 2021 and 2099 and their results assessed with five parameters (water level, epilimnion and hypolimnion temperatures,

the Schmidt Number and the thermocline depth). Results indicate the strengthening of the stratification stability over time, suggesting possible alterations of the lake's thermal regime, with the reduction of mixing events and the predominance of stratified conditions.

**Keyword:** Reservoir. Lakes Hydrodynamic**.** Computational Modeling. Climate Change.

# RESUMO

DUARTE, B. P. S. **Modelagem unidimensional hidrodinâmica de reservatórios e o impacto de cenários de mudanças climáticas sobre seu comportamento térmico.** 2022. Dissertação (Mestrado) – Escola Politécnica. Universidade de São Paulo, São Paulo, 2022.

A ocorrência de eventos de estratificação e mistura determina o regime térmico de lagos e reservatórios, influenciando em suas características físicas, químicas e biológicas. A frequência e duração desses eventos são determinadas pelas condições atmosféricas locais, pela morfologia e pela presença de vazões de entrada e saída em um lago. Lagos tropicais pequenos são essenciais para o desenvolvimento de muitas cidades, em vista de seus usos múltiplos. No entanto, estudos sobre esses ambientes ainda são escassos e restritos. Nesse contexto, este trabalho tem como objetivo investigar a representação do comportamento térmico de um pequeno reservatório polimítico-tropical com um modelo matemático unidimensional e avaliar os impactos de cenários de mudanças climáticas sobre esse comportamento. O estudo de caso foi focado na Barragem de Hedberg, uma lagoa de 0,23 km²-4,5m de profundidade, construída no início do século XIX, localizada a cerca de 90 km da cidade de São Paulo, no Brasil. Sua bacia hidrográfica é parcialmente protegida pela Floresta Nacional de Ipanema, com escassa presença de infraestrutura urbana e intensa ocupação agropecuária. O software aplicado foi o General Lake Model (GLM), um modelo hidrodinâmico unidimensional, que utiliza uma abordagem determinística, mecanicista, dependente do tempo e com resolução numérica. Com intervalos de tempo horários, o modelo utiliza como dados de entrada: características morfológicas, variáveis atmosféricas e vazões. Dados de sensores térmicos de alta frequência foram utilizados para a calibração e validação do modelo, entre os anos de 2017 e 2020. Os resultados foram considerados adequados, visto que o modelo representa satisfatoriamente os padrões diários e sazonais observados no reservatório. Para os cenários de mudanças climáticas, utilizou-se o modelo climático regional Eta, com resolução espacial de 20 km. Os cenários escolhidos foram o RCP 4.5 (otimista) e o RCP 8.5 (pessimista), propostos pelo IPCC, que indicam o aumento da temperatura média global em 1,8°C e 3,6°C, respectivamente, até o final do século. Os

cenários foram simulados entre 2021 e 2099 e seus resultados avaliados através de cinco indicadores (nível da água, temperatura do epilímnio e do hipolímnio, número de Schmidt e profundidade da termoclina). Os resultados indicam o fortalecimento da estabilidade térmica ao longo do tempo, sugerindo possíveis alterações do regime térmico do lago, com a redução de eventos de mistura e predominância de condições estratificadas.

**Palavra-chave:** Reservatório. Hidrodinâmica de Lagos. Modelagem Computacional. Mudança Climática.

# LIST OF FIGURES

# LIST OF TABLES

# ACRONYMS AND SYMBOLS

| | |
|---|---|
| 1D | One-dimension |
| 1DV | One-dimensional vertical model |
| AED | Aquatic EcoDynamic |
| AR5 | Fifth Assessment Report |
| FCTH | Hydraulic Technology Centre Foundation |
| GLEON | Global Lake Ecological Observatory Network |
| GLM | General Lake Model |
| INMET | National Institute of Meteorology |
| IPCC | Intergovernmental Panel on Climate Change |
| KE | Kinect Energy; |
| KH | Kevin-Helmholtz |
| L | Length Unit; |
| M | Mass Unit; |
| MAE | Mean Absolut Error |
| MOMA | Modeling Program for Strategic Metropolitan Waters as an Input for Water and Territory Management in the Face of Climate Change |
| NMAE | Normalized Mean Absolut Error |
| NSE | Nash Sutcliffe Efficiency |
| r | Correlation coefficient; |
| R | Programming Language |
| RCP | Representative Concentration Pathways |
| RMSE | Root Mean Square Error |
| T | Time Unit; |
| UWA | University of Western Australia |

# SUMMARY

# 1 INTRODUCTION

Limnology can be defined as the study of all bodies of water located inside a continental boundary. Lakes, reservoirs, rivers, streams, ponds, groundwater and estuaries. Among this extensive range of environments, lentic bodies of water (i.e., lakes, reservoirs and ponds) present some unique dynamic characteristics, which will influence their physical, chemical and biological structures.

The two main physical processes brought about on these environments are the stratification and mixing of the water column. As the solar radiation reaches the lake' surface, the water column is heated in a non-homogeneous pattern, generating a thermal-density gradient that, through the buoyancy forces at place, defines a stratified vertical profile. When these vertical buoyancy forces are overcome by the kinetic turbulent energy available in the system, provided by convective cooling, wind stirring and/or internal waves, the mixing processes take place, allowing for the transportation of water, nutrients, dissolved gases and the local biota along the vertical layers (Tundisi and Tundisi, 2008).

Understanding these processes, predicting their characteristics and assessing their impacts are of great interest for decision-makers, who have been, more and more, relying on mathematical models to support the planning and application of management practices onto lentic environments. However, the selection of an adequate model to perform a study must take into account: the study objectives, the available dataset, the model approach on modeling the phenomena of interest, as well as its limitations and biases (Ji, 2008).

One-dimensional vertical (1DV) models have been widely applied for the study of the physical and chemical characteristics of lakes and reservoirs whenever the longitudinal dynamics can be overlooked in the face of the predominance of the vertical processes. These models' great computational efficiency and minimal calibration requirements, back their use as an interesting tool for large cross-lakes comparisons and long-term analysis, like climate change impacts assessment (Read *et al.*, 2014) (Bruce *et al.*, 2018) (Janssen, Teurlincx, *et al.*, 2019).

For the past decade, many studies have used 1DV hydrodynamic lake models to evaluate the representation of the thermal behavior of lakes and reservoirs with distinct characteristics across the globe. These studies focused on large deep lakes in tropical (Thiery *et al.*, 2014; Polli and Bleninger, 2019) and temperate (Fenocchi *et al.*, 2017; Huang *et al.*, 2017; Huang *et al.*, 2019; Farrell *et al.*, 2020) zones, large shallow lakes in subtropical (Deng *et al.*, 2013; Soares *et al.*, 2020) and temperate zones (Saloranta and Andersen, 2007; Woolway *et al.*, 2017) and temperate small shallow lakes (Kirillin, 2010; Prats and Danis, 2019; Shatwell *et al.*, 2019).

Among these studies, different mixing regimes were evaluated, as meromictic (Thiery *et al.*, 2014), monomict (Fenocchi *et al.*, 2017; Soares *et al.*, 2020), dimictic (Kirillin, 2010; Huang *et al.*, 2019; Farrell *et al.*, 2020) and polymictic (Kirillin, 2010; Woolway *et al.*, 2017; Soares *et al.*, 2020) lakes were simulated. However, few studies have been developed for small-polymictic-tropical lakes.

Small-tropical lakes and reservoirs are essential to many tropical cities. Their multiple uses can range from water supply, fishery, recreation, landscape, to flow regulation on arid regions (Mendoza *et al.*, 2019; Zhang *et al.*, 2019). Yet, the study of this set of tropical environments is still scarce and restricted, as many tropical developing countries struggle to fill the knowledge gaps about the impact of the climatic drivers over small and shallow lakes, their thermal behavior and productivity (Talling, 2001; Augusto-Silva *et al.*, 2019; Mendoza *et al.*, 2019).

In this study, the 1DV hydrodynamic model, General Lake Model (GLM), was selected to perform the simulation of the Hedberg reservoir, located in Iperó (São Paulo, Brazil). The Hedberg reservoir is a 0.2 $km^2$-4.5 m depth tropical dam, built in the beginning of the $19^{th}$ century, that presents a polymictic thermal behavior. The model was simulated between the years 2017-2020 (calibration and validation) and its results were assessed in the light of the model's performance, limitation, and biases. As a next step, two distinct regional climate change scenarios, an optimistic (RCP 4.5) and a pessimistic one (RCP 8.5), were simulated and their impacts assessed over a 79-year period (2021 – 2099).

This study was supported by CAPES (Coordenação de Aperfeiçoamento de Pessoal de Nível Superior) (finance code: 88887.599403/2021-00), within the MOMA-SE project (Project call

CAPES-ANA 19/2015 - Modeling Program for Strategic Metropolitan Waters as an Input for Water and Territory Management in the Face of Climate Change).

# 2 OBJECTIVES AND METHODOLOGICAL APPROACH

## 2.1 OBJECTIVES

The general objective of this study is to investigate the vertical thermal behavior, here defined by stratification and mixing events, of a tropical-polymictic-shallow lake and assess the climate change impact over it, through the application of a one-dimensional vertical model, the General Lake Model (GLM), in the Hedberg reservoir (Iperó, São Paulo).

The specific objectives of this study are:

1. To investigate the thermal vertical behavior observed in lakes and reservoir and the influence of its driving forces;
2. To compile, analyze and organize the observed and projected data, filling inconsistencies and supplying them to the model;
3. To calibrate and validate the GLM model for the Hedberg reservoir, evaluating the model performance, limitation and biases over the thermal behavior characterization;
4. To simulate two distinct climate change scenarios: an optimistic and a pessimistic one;
5. To investigate and evaluate, quantitatively and qualitatively, the climate change impacts trends over the vertical thermal behavior of the Hedberg reservoir.

## 2.2 METHODOLOGICAL APPROACH

The methodological approach applied for this study included:

1. Literature review of the thermal dynamics governing the vertical structures on lakes and reservoirs, focused on the stratification and mixing processes and the main driving forces;
2. Literature review of hydrodynamic modeling and its governing principles;
3. Investigation of the General Lake Model hydrodynamic approach;
4. Data compilation, preparation and analysis, through field monitoring campaigns and public access databases;
5. The General Lake Model set up, calibration (2017 - 2018), validation (2019 - 2020) and performance evaluation;
6. Climate change simulations of optimistic and pessimistic scenarios (between 2021 and 2099);
7. Assessment of the climate change scenarios impact over the Hedberg thermal behavior.

# 3 LITERATURE REVIEW

This chapter presents the literature review of lakes and reservoirs hydrodynamic structures and processes, with a focus on stratification and mixing events and their main meteorological driving forces: solar radiation and wind. The representation of these phenomena through a mathematical modeling approach is discussed in the light of its governing principles, hydrodynamic equations and model performance assessment. At last, a literature review on the study of climate change impact over lentic environments is presented.

Therefore, this chapter aims to address the first specific objective of this study.

## 3.1 LAKES AND RESERVOIRS STRUCTURES

Lakes and reservoirs differ from river and estuarine systems due to important characteristics, as: long detention time, reduced longitudinal velocity, a noteworthy vertical stratification structure and the accumulation of nutrients, organic matter and sediments (James, 1993). The hydrodynamic processes on these environments rely on morphology characteristics, meteorological conditions and hydrological patterns, whereas the water quality processes are results of the interaction between these hydrodynamic structures and the watershed incoming loads (Janssen, Van Wijk, *et al.*, 2019) (Amorim, 2020).

In order to better understand the internal structure of a lake and identify its patterns, distinct zones are defined (*Figure 1*). The presence or absence of light determines, respectively, the photic and aphotic zone. The photic (or euphotic) zone extends from the free surface down to where the PAR (photosynthetically active radiation) is about 1% of the total incident radiation on the lake' surface (Goldman and Horne, 1985). In most cases, this zone is related to a lighted and productive water volume layer, where the photosynthetic rate is positive and greater than the consumption of oxygen. Beneath the photic zone, all the way to the bottom of the lake, the aphotic zone establishes itself as a region of oxygen consumption, due to organisms' respiration and organic matter decomposition (Imberger and Patterson, 1989) (Tundisi and Tundisi, 2008).

In shallow and transparent lakes, the whole lake can be lighted. whereas in some deeper lakes, there can be areas where light never reaches, and, therefore, depend on diffusion and mixing processes to gain access to the lighted layers properties.

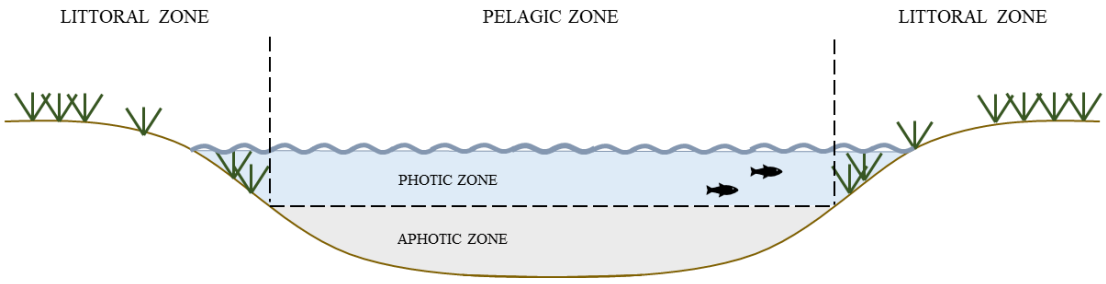


**Figure 1 - Zonation diagram of a lentic environment. Source: Author.**

Far from the banks influence, on the pelagic zone, the vertical structures of these environments are related to the heat and density variations within the system. On low salinity lakes, the density profile is mainly governed by the thermal structure and can be decomposed into three distinct layers: epilimnion, metalimnion and hypolimnion.

The epilimnion is the upper, warmer and less dense layer. It can be described as a well-mixed reactor, where the main heating and cooling processes come about.

The metalimnion is the layer on which the rate of temperature changes expressively over the depth. Its limits are not clearly defined, but its placement can be determined around the greater inflection on the temperature x depth curve. The depth of the greater inflection is called the thermocline. (*Figure 2*)

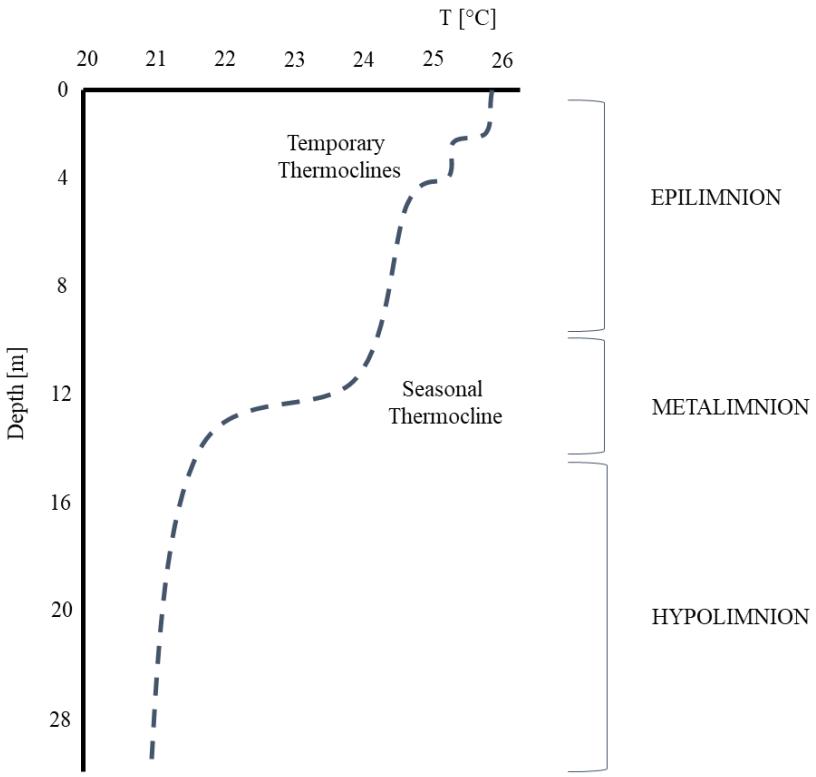


**Figure 2 - The vertical thermal structure of a stratified lake. Source: Author.**

More than one thermocline can be identified on the vertical thermal profile of a lake. The seasonal thermocline is usually the lower one and represents the accumulation of past diurnal mixed-layer events, establishing itself as the main barrier to the mass exchange processes upon the vertical dimension of a lake. The temporary thermoclines, formed by diurnal stratification events, are described as step like structures associated to the surface-induced turbulent activity and heat fluxes occurring on the related day (Imberger, 1985).

On large lakes, longitudinal differences on the thermocline conformation can be observed, with the littoral zone stratifying earlier than the pelagic zone (Imberger, 1985). However, these differences are not going to be discussed on this study.

The hypolimnion is the deeper, colder and denser layer. This quiescent layer has its main heat and momentum exchanges taking place through the metalimnion-hypolimnion interface or in the bottom of the lake, on the water-soil boundary (Goldman and Horne, 1985) (Tundisi and Tundisi, 2008).

## 3.2 HYDRODYNAMIC PROCESSES

Stratification and mixing are the two main hydrodynamic processes occurring in lentic environments. Their impacts affect not only the thermal-density structure, but also the circulation of nutrients, sediments, dissolved gases and the lake's biota. Algae blooming, hypolimnetic anoxia and presence of toxins on the water are some of the problems associated with the occurrence of strong or prolongated stratification events. Therefore, the comprehension of the hydrodynamic processes is essential to improve the management and operation of these systems (Chin, 2012).

### 3.2.1 Stratification events

The vertical stratification of the water column, into the physical structure presented in *Figure 2*, is formed and maintained due to the transfer of heat and momentum from the surface down to the base of the epilimnion, and, also, due to gravity forces acting on water masses of distinct densities (Imberger and Patterson, 1989). The transfers of heat and momentum onto the lake' surface are associated with energy inputs from the solar radiation and wind stress, respectively (Chapra, 2008).

Over the course of a year, the thermal structure of a lake may undergo some abrupt changes, such as: the onset of stratification and the overturning events. The onset of stratification can be described by the heating of the upper layer in response to the incident solar radiation (3.3.1 Solar Radiation) that, as it penetrates the water column, is reflected, scattered, transmitted and absorbed. The absorbed radiation is, then, transformed into heat (Boehrer and Schultze, 2008). Most of the heat is generated in the first few meters, depending on the water transparency, since the radiation intensity decreases exponentially with depth (Kirillin, 2010).

On the other hand, wind stirring onto the lake' surface produces momentum that will be transmitted from the air-water interface downward, until it is dissipated by turbulence, promoting, with it, the homogeneous mixing of the upper layer (Wüest and Lorke, 2003) (Tundisi and Tundisi, 2008). The lower boundary of the mixed-layer will be defined by the

thermocline, indicating the depth bellow which the difference of densities prevents the mixing forces to prevail (Imberger and Patterson, 1989).

Density differences between layers indicate the strength of the stratified structure. In warm waters, the density change per degree of temperature is greater than in colder temperatures, therefore, it takes more energy to break the stratification, for example, between layers of 19°C and 20°C, than it takes between layers of 9°C and 10°C (Goldman and Horne, 1985).

In order to define the ratio of energy required to overcome the buoyancy forces by the stirring currents on a lake, the Richardson Number is proposed:

$$Ri = \frac{g\frac{d\rho}{dz}}{\rho\left(\frac{dU}{dz}\right)^2} \quad (1)$$

where Ri is the Richardson Number [dimensionless]; g is the gravity acceleration [$LT^{-2}$]; ρ is the density of the fluid [$ML^{-3}$]; U is the horizontal current velocity [$LT^{-1}$]; and z is depth [L].

Comparing the water buoyancy forces (inertia), through the density rate over depth, with the energy from current stirring (kinetic), Equation ((1) qualifies the analysis of the energy required to destroy the stratification event in comparison with the available Kinetic Energy (KE) on the system. The critical Richardson Number, valued at 0.25, indicates, for lower values, that the kinetic forces available were able to overcome the stratification and, for higher values, that the stratification is preserved (Martins, 2017).

The Schmidt Stability also provides an estimation for the lake' stratification strength since its numerical value is a measure of the amount of energy (in J/m²) required to mix the whole lake. Using the center of volume and not portraying any meteorological driver, the index weights out the influence of morphometric features, as well as of the external environment (Read *et al.*, 2011).

$$S_T = \frac{g}{A_S}\int_0^{z_D}(z - z_v)\rho_z A_z \partial z \quad (2)$$

where $S_T$ is the Schmidt Stability number [$MT^{-2}$]; g is the gravity acceleration [$LT^{-2}$]; $\rho$ is the density of the fluid [$ML^{-3}$]; $A_S$ is the superficial area [$L^2$]; Az is the area at depth z [$L^2$]; $z_D$ is maximum depth [L]; $z_v$ is the depth at the lake's center of volume [L]; and z is depth [L].

The available energy on each layer is a function of the meteorological forces acting on the system and of its previous state. Daily events alter the system state, building up the conditions for the occurrence of the major events. During these diurnal cycles the thermocline will rise and deepen according to the heat inputs, wind stirring and convective induced turbulences, altering the former composition of the layers (Imberger, 1985). The interaction between each layer will determine the whole lake dynamic.

The epilimnion, through its air-water boundary, is the layer where the main heating and cooling processes reach the system. Its main energy sources are the solar radiation, inflows and outflow, evaporative losses and sensible heat exchanges. The energy balance of the upper layer varies in a day-to-day basis due to weather and hydrological conditions, but its energy budget is higher than any other, with a warmer water volume, the presence of currents and wind action supplying momentum to the water column (Imberger and Patterson, 1989).

As a dynamic mobile layer, the metalimnion rises and falls throughout the year in response to the energy budget available on the epilimnion. Therefore, its main source of energy is the layer placed above it, the epilimnion itself. The occurrence of turbulence due to natural convection, propagation of internal waves and Kevin-Helmholtz instabilities also provide energy to the layer (Simpson *et al.*, 2015).

Above all, the metalimnion mediates the energy and mass exchanges between the upper and lower layers. The hypolimnetic entrainment process, for example, transfers water from the hypolimnion to the metalimnion during calm weather conditions, expanding the metalimnion volume. With a strong wind event, this former hypolimnetic volume of water will be incorporated by the epilimnion, as a result of the thermocline deepening (Goldman and Horne, 1985). Even if small volumes of water do not significantly affect the epilimnion temperature, the transport of nutrients enriches the upper layer.

The hypolimnetic energy sources are the geothermal exchanges, submerged inflows and outflows, gravity currents, the upper layers interactions and direct solar radiation. In transparent lakes, where the light can reach bellow the thermocline, the direct solar radiation in the hypolimnion can be the main heating source.

The hypolimnetic temperature, during the stratified period, depends on the moment of the first onset of a density profile and the system state at the time (Goldman and Horne, 1985). This moment varies each year and will influence the hypolimnetic organism activity (Ladwig *et al.*, 2021).

### 3.2.2 Mixing events

Turbulent water movement processes induce the homogenization of water masses, depending on its energetic capability to break the stratified structure. Mixing events inside the layers or throughout the whole lake promote the distribution of energy, momentum, dissolved gases, nutrient, sediments and even organisms, impacting on the productivity of a lake (Boehrer and Schultze, 2008). The mass transport can also affect water transparency, turbidity and coloration, as well as quality parameters through the resuspension of sediments, organic matter, nutrients and toxins (Tundisi and Tundisi, 2008).

The two main mechanisms of mass movement in water bodies are the advective and diffusive (or dispersion) transports (Imboden and Wüest, 1995). The advective transport represents the motion of a particle due to a velocity vector, thus, it reflects the effect of currents and convective motions. The diffusive transport, on the other hand, assess the molecular and turbulent aspects of a fluid motion. On the molecular level, it represents the flux of a particle in response to a difference in the spatial gradient between an infinitesimal volume and its surrounding water (Chapra, 2008). Therefore, it reproduces the mass exchange at the interface of volumes with distinct characteristics. As on the turbulent aspect, the chaotic and random motion of the fluid instigate a dispersive transport in all dimensions (Martins, 2017).

On vertically stratified environments, however, higher rates of diffusive transport are observed on longitudinal dimensions, once the buoyancy forces do not have to be overcome on them. (Goldman and Horne, 1985)

Overturning processes, which breaks the stratified structure and mixes the whole lake, happen in response to changes in the system potential energy budget. The reduction of heat inputs, because of meteorological events (winter, cloudy days, topographic shading) or evaporative losses, affects the density distribution and its buoyancy forces, reducing the stratification stability (Boehrer and Schultze, 2008). In this scenario, strong wind stirring events, which are able to transmit sufficient kinetic energy to the surface layer of the lake, can alter the former energy budget, promoting the erosion of the thermocline, due to the turbulence produced on the metalimnion that overcomes the resistance of density gradients (Imberger and Patterson, 1989) (Wüest and Lorke, 2003) .

The relation proposed by Amorim (2020) indicates if a lake is undergoing an event of structure alteration, the onset of stratification or the overturn of the water column. With radiation and wind data, representing the external forces, and the Schmidt Stability number (Equation (2)) as a measure of the lake state, within the prior 24-hour period, Equation (3) and (4) determines the chance of an instability occurrence within the system

$$W* = C_D \rho_a \Delta U^2 \Delta z \tag{3}$$

$$log\left(\frac{S*}{Rad}\right) = -1.1885 \log\left(\frac{W*}{S*}\right) - 6.5341 \tag{4}$$

where $S^*$ is the mean Schmidt Stability number of the prior 24hs [$MT^{-2}$]; Rad is the total amount of incident radiation of the prior 24hs [$MT^{-2}$]; W* is the wind speed hourly variance in a 24hs period of time [$LT^{-1}$]; $\rho_a$ is the density of the air [$ML^{-3}$]; U is the wind velocity [$LT^{-1}$]; $C_D$ is the drag coefficient [dimensionless]; and z is depth [L].

The critical boundaries to be observed are determined by the equation curve (Figure 3). For mixing events $\log\left(\frac{W*}{S*}\right)$ > -1.8 and $log\left(\frac{S*}{Rad}\right)$ < -3.8, indicating the predominance of the wind as main force, and for the onset of stratification $\log\left(\frac{W*}{S*}\right)$ < -1.9 and $log\left(\frac{S*}{Rad}\right)$ > -3.7, with radiation prevailing as the overall energy source of the lake.

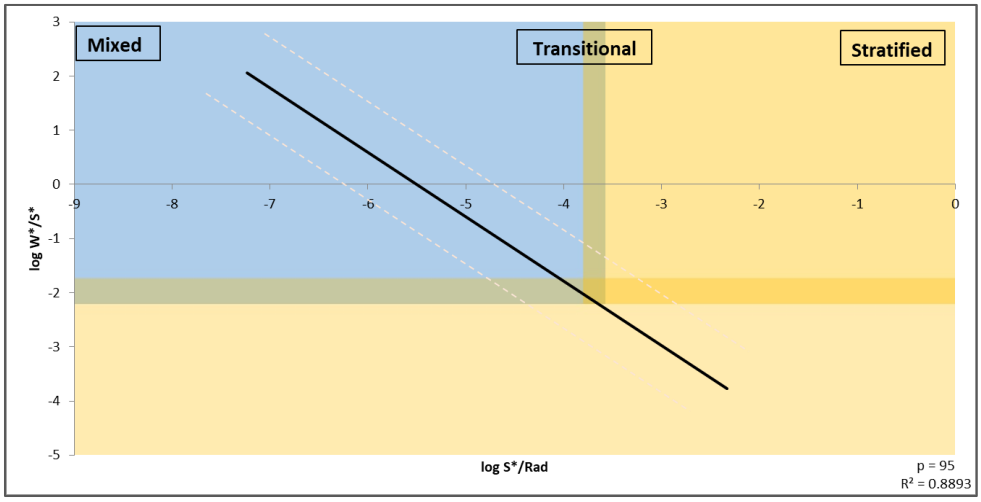


**Figure 3 - Thermal stability limit curve diagram, with the areas that explains the water column thermal structure Source: Amorim (2020).**

During stratification events, water masses motion can be observed in all density delimited layers: the epilimnion, metalimnion and hypolimnion (Wüest and Lorke, 2003) (Simpson *et al.*, 2015).

The epilimnion receives direct wind stir, through the air-water interface. Therefore, the wind energy input onto the system is concentrated on this layer and cascades downwards, prompting distinct water movement processes (Boehrer and Schultze, 2008).

Most of the applied energy is carried-out by surface horizontal currents, formed as the air moves close to the water, producing shear stress on the interface. The stress will originate a corresponding current, with the same direction and reduced velocity, compared to the wind. Through the vertical diffusion of momentum, the inputted energy descends over the water column, being dissipated in its way down, to a point of zero net flow (Goldman and Horne, 1985) (Wüest and Lorke, 2003).

Larger circulation events also can be set up by the wind action (Fernández Castro *et al.*, 2021). As the wind drives water from the upper layer to lee shore, it piles up water masses, establishing an unequal pressure force field. The piled water mass is pushed down, tilting the vertical structure over a longitudinal plane. Upwind, depending on the strength of the wind event, the thermocline can be exposed and cold, denser and nutrient enriched hypolimnetic water can upwells to the surface. On large lakes, the upwelling can produce horizontal and

vertical temperature gradients, before its total incorporation by the epilimnion (Imberger and Patterson, 1989) (Henderson and Deemer, 2012).

The Wedderburn Number (Equation (5), proposed by Thompson and Imberger (Thompson and Imberger, 1980), discusses the prospect of an upwelling or overturn event to take place in a stratified environment. The index compares the inertial and kinetic mechanisms at place on the system (as the Richardson Number (Equation (1)), adding the lake basin influence through its aspect ratio.

$$W = \frac{g' {z_e}^2}{{u_*}^2 L_S} \tag{5}$$

where W is the Wedderburn Number [dimensionless]; g'= g ($\Delta\rho/\rho$) is the reduced gravity acceleration [$LT^{-2}$]; $\rho$ is the density of the fluid [$ML^{-3}$]; $u_*$ is the superficial shear stress [$LT^{-1}$]; $L_S$ is the fetch distance [L]; and $z_e$ is the depth at the bottom of the epilimnion [L].

The critical Wedderburn Number is 1, when the inertial and kinetic forces are balanced. For $W < 1$, it is likely for the system to suffer an upwelling or overturn event. If $W > 1$ the stratification is maintained. (Read *et al.*, 2011)

On the metalimnion, motion, if not produced by natural convection, is mainly determined by the presence of internal waves and the set off turbulences. (Imberger and Patterson, 1989) (Wüest and Lorke, 2003) (Henderson and Deemer, 2012) (Simpson *et al.*, 2015)

Diffusive transport, on the metalimnion, occurs at very low rates, because of the density gradient influence. On the hypolimnion, on the other hand, it is the main transport process to take place. However, some motion may also be a result of the vertical displacement of the thermocline, triggered by the passage of internal waves, which can cause turbulence near the bed of the lake (Wüest and Lorke, 2003).

The Lake Number (Equation (6), also proposed by Imberger (Imberger and Patterson, 1989), is another index used to assess the internal mixing of lakes, in response to wind forcing. Like the Wedderburn Number (Equation (5), lower values indicate potential mixing events. However, since the index uses the metalimnion to evaluate the inertial and kinetic

characteristics of the system, it can provide an insight of the thermocline stability in response to the system state (Read *et al.*, 2011)

$$L_N = \frac{S_T(z_e + z_h)}{2\,\rho_h {u_*}^2 {A_s}^{1/2} z_v} \quad (6)$$

where $L_N$ is the Lake Number [dimensionless]; $S_T$ is the Schmidt Stability number [$MT^{-2}$]; $\rho_h$ is the density of the fluid at the bottom of the metalimnion [$ML^{-3}$]; $u_*$ is the superficial shear stress [$LT^{-1}$]; $A_S$ is the superficial area [$L^2$]; $z_v$ is the depth at the lake's center of volume [L]; $z_e$ is the depth at the top of the metalimnion [L]; and $z_h$ is the depth at the bottom of the metalimnion [L].

### 3.2.3 Thermal Classification

Lakes and reservoirs can be classified accordingly to their thermal behavior throughout the year climatological cycle (Kirillin and Shatwell, 2016). An amictic lake is kwon for never mixing completely, whilst an oligomictic will mix once every few years. Monomict lakes undergo only one mixing event a year, usually during winter. While a dimitic environment mixes twice a year, during the spring and fall. Most lakes located at temperate zones are dimitic.

Polymictic lakes, on the other hand, undergo many mixing events during the year. Depending on the local conditions, stratification can last for only a few days before a storm or strong winds breaks its stability. Daily events can, sometime, have a more relevant role in the thermal pattern of these systems than seasonal variations. Most polymictic lakes are located on tropical zones. (Goldman and Horne, 1985) (Chin, 2012)

## 3.3 DRIVING FORCES

The two main driving forces of the systems are the meteorological variables: solar radiation and wind. Current circulation due to advection (inflow and outflow) and freezing/melting can also be included as additional forcing factors, when appropriate. This section will better define the two atmospheric drivers, describing their main characteristics and how they interact with the studied environments.

### 3.3.1 Solar Radiation

Solar radiation is the primarily energy source of the Earth, being responsible for the surface heating of land and water bodies, atmospheric patterns formation – as world winds movements –, photosynthetic processes and life distribution throughout the globe (Goldman and Horne, 1985). As a wave phenomenon, the solar radiation can be described by its wavelength and frequency; as energy, by its intensity and direction (Varejão-Silva, 2000).

In this study, the word radiation will be used to define the radiant energy, specifically the solar incoming energy, in the totality of its wavelength spectrum. Whilst the word light will be restricted to the visible portion of the solar radiation spectrum, from approximately 360 to 740 nm.

The incoming radiation, on the top of the Earth's atmosphere, has a wide range of wavelengths and an irregular spectral distribution. As it crosses the atmosphere, the distinct wavelengths are reflected, scattered and absorbed by clouds, fog and the suspended particles that composes the atmosphere. Nonetheless, the solar radiation reaching the Earth surface is a fraction of the incoming total, with reduced intensity and a narrower wavelength spectrum. (*Figure 4*) (Varejão-Silva, 2000).

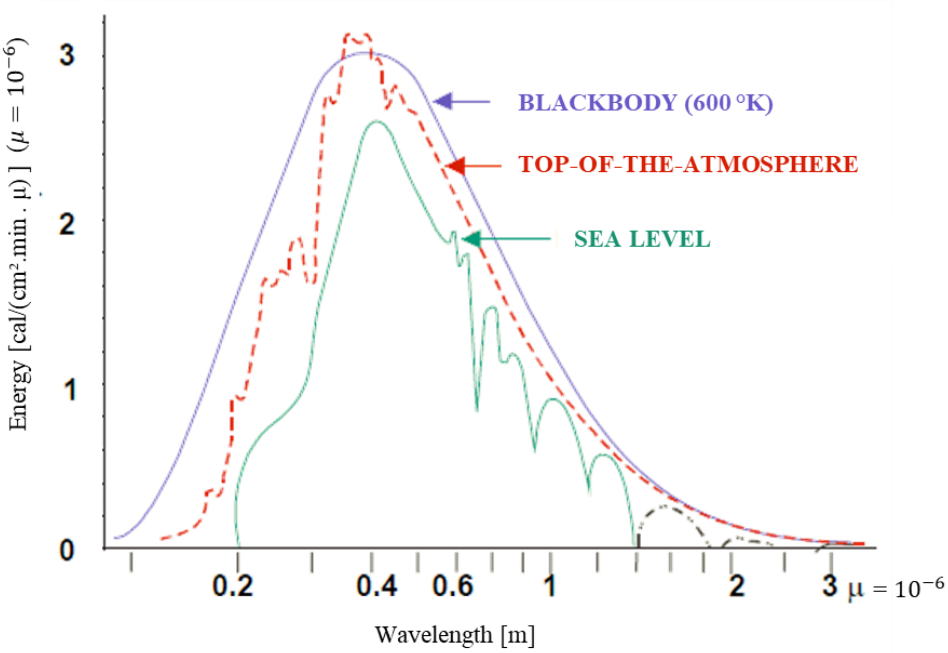


**Figure 4 - Spectral distribution of solar radiation on the top-of-the-atmosphere(red) and at sea level(green), compared to the emission of a blackbody at 6000°K. Source: VAREJÃO-SILVA (2000) – Adapted.**

Two sets of radiation wavelengths can be defined: shortwave and longwave. Most of the solar incoming radiation is defined as shortwave, comprehending the ultraviolet, visible and near infrared parts of the spectrum. Meanwhile, the longwave comprehends the infrared part of the spectrum and its main source is the energy emission by the Earth' surface.

On lakes and reservoirs, the shortwave portion may reach the water as direct or diffuse (indirect) radiation (Naghib *et al.*, 2018). The direct fraction is provided by the sun, during the lighted time of the day – the photoperiod. As the diffuse fraction is due to the scattering across the atmosphere or by topology features. The longwave emissions from the Earth are backed to the surface by clouds, as indirect radiation (Varejão-Silva, 2000).

Hence, the incoming solar radiation is a function of the sun emission characteristics and its distance and angle of incidence, represented by the local latitude. The season of the year, hour of the day, local cloud cover and the watershed topography also determine how and how much of this driving force is going to be applied onto the system (Tundisi and Tundisi, 2008).

Once the radiation reaches the water surface, it will first be refracted, then reflected, scattered and selectively absorbed, bringing about the hydrodynamic processes described in 3.2.1 Stratification events (Naghib *et al.*, 2018). The longwave radiation is absorbed in the initial meters, whereas the visible portion penetrates down the water column, triggering photosynthetic responses and being partially scattered back to the surface, where it composes the observed lake color (*Figure 5*) (Goldman and Horne, 1985) (Tundisi and Tundisi, 2008).

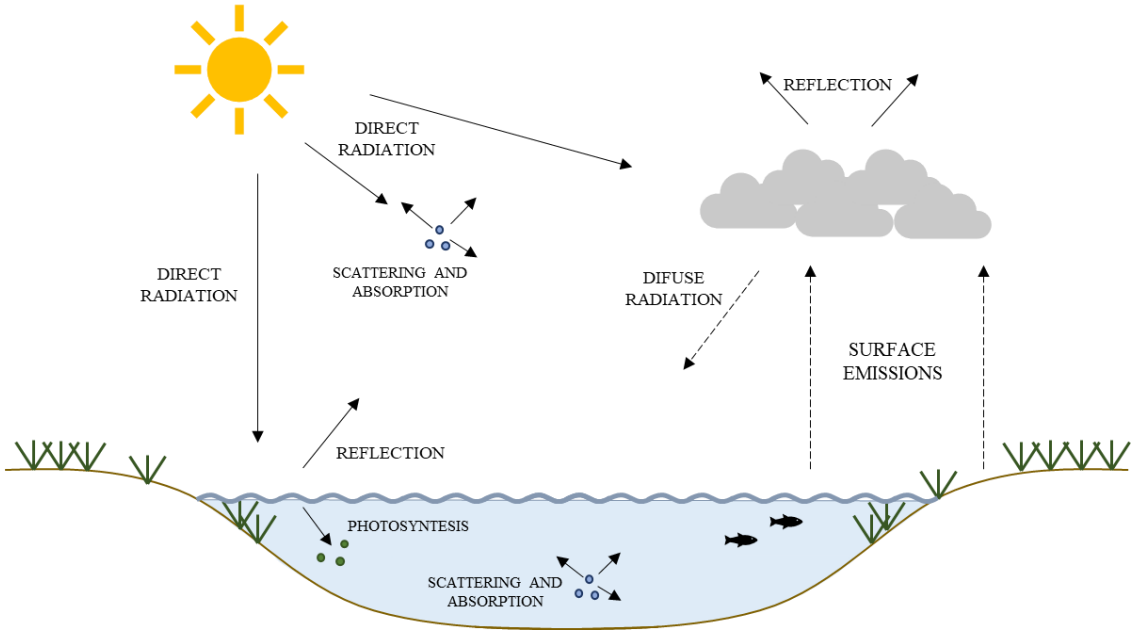


**Figure 5 - Solar radiation and its interactions with the environment. Source: Author.**

In order to represent the exponential loss of light intensity, as the radiation penetrates the water column, the light extinction coefficient (Kw) is used. It represents the fraction of light held back per meter of depth. The coefficient sums up the effects of the water, dissolved substances, particles in suspension and chlorophyl absorption and its value is inversely proportional to the Secchi depth (Equation (7). Thus, the lower the Kw value, the deeper the light is transmitted (Tundisi and Tundisi, 2008) (Martins, 2017).

$$Kw = \frac{1.7}{Z_{secchi}}. \qquad (7)$$

where Kw is the light extinction coefficient [$L^{-1}$]; and $Z_{secchi}$ is the Secchi depth (depth measured with the Secchi disk and determined by visual analysis of the observer) [L].

### 3.3.2 Wind

Wind is the second most important driver of hydrodynamic processes on lentic systems. It is defined as the horizontal component of the air velocity vector and, as a vector, can be described by its magnitude (velocity) and direction. Globally, the wind patterns are generated by the interaction between solar radiation and the Earth's rotation, whereas, locally, they are influenced by the topography and meteorological conditions (Varejão-Silva, 2000).

On lakes and reservoirs, wind acts on the air-water interface, creating shear stress and, thus, transmitting momentum to the water surface (Wüest and Lorke, 2003). However, the energy acquired by the upper layer is reduced, in comparison to the applied wind energy, due to the density differences of the fluids. If the interplay between air and water maintained a steady state, the wind would transmit around 3% of its energy to the lake' surface. Still, this rate is variable, since it can be influenced by surface conditions (smooth or rough surfaces). (Goldman and Horne, 1985) (Martins, 2017)

Other factors influencing the amount of energy to be made available for the upper layer, by wind stirring, are: local wind conditions – such as velocity, frequency and direction –, the basin topology and the fetch distance (Fernández Castro *et al.*, 2021). The fetch is defined as the longest distance over which the wind can blow onto the lake' surface (*Figure 6*) (Tundisi and Tundisi, 2008).

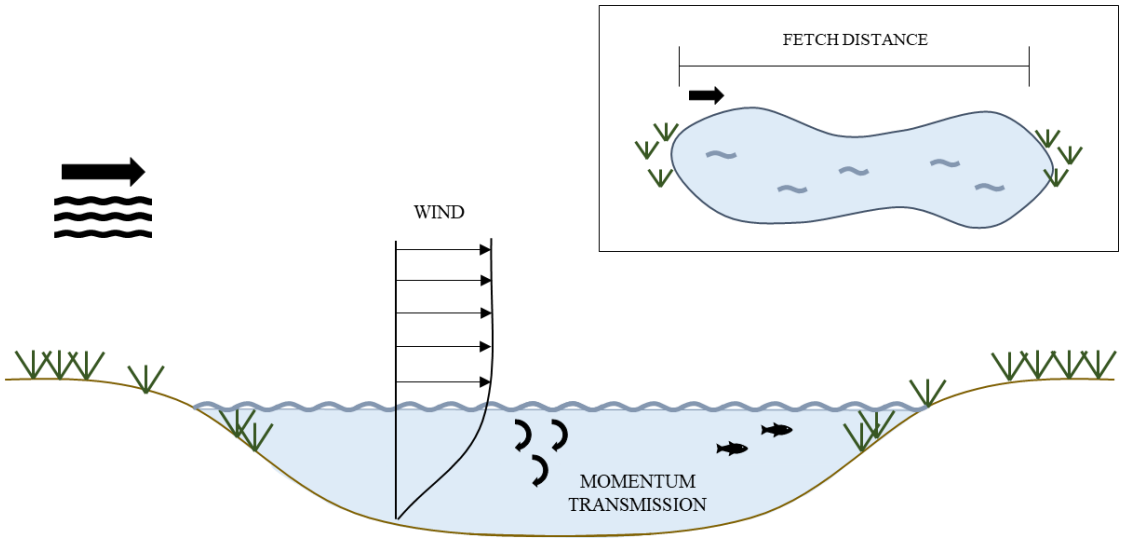


**Figure 6 - Wind and its interactions with the environment. Source: Author.**

To represent the influence of the wind stirring on lakes, the drag coefficient ($c_D$) is used. It represents the fraction of the wind velocity energy that becomes available for the shear stress operating on the water surface. (Equation (8) (Imberger, 2013) (Martins, 2017) .

$$u_*^2 = \frac{\tau_s}{\rho_a} = c_D U_z^2 \qquad (8)$$

where $u_*$ is the shear velocity associated to the wind [$LT^{-1}$]; $\tau_s$ is the surface stress [$ML^{-1}T^{-2}$]; $\rho_a$ is the density of the air [$ML^{-3}$]; $c_D$ is the drag coefficient [dimensionless]; and $U_Z$ is the wind velocity at a z height from the surface [$LT^{-1}$].

## 3.4 MATHEMATICAL MODELING

In engineering, models can be defined as simplified systems representations. Based on the physical, chemical and biological knowledge of a system, a mathematical model formulates and computes information about its initial conditions and main stimuli forces, in order to achieve a reliable portrayal of the simulated reality (Ji, 2008) (Chapra, 2008).

Mathematical models have been, more and more, used to investigate and assess a diverse set of problems in environmental sciences, mainly in the hydraulic field study. Their

applicability range from: comparing simulated and observed data to better understand the phenomena and identify patterns (Read *et al.*, 2014) (Saber *et al.*, 2018) (Amorim, 2020) (Soares *et al.*, 2020), evaluate and foresee hydrological, hydrodynamic, water-quality and biological problems (O'reilly *et al.*, 2015) (Rocha Junior *et al.*, 2018) (Harrison *et al.*, 2019) (Janssen, Janse, *et al.*, 2019), to simulate climate change scenarios and assess their impacts (O'reilly *et al.*, 2003) (Kirillin, 2010) (Woolway *et al.*, 2017) (Da Silva *et al.*, 2020) (Fernández Castro *et al.*, 2021), and to support decision-making processes on water bodies management (Baptistelli, 2008)

There are several different hydrodynamic and water quality models that can be used to simulate lentic environments. The decision-making process, on which model should be chosen to perform a study, will depend on the intended result, environment characteristics, the available dataset, the project resources and restrictions – budget, deadlines, expertise of the modelist –, and the existing literacy and documentation (Ji, 2008).

One of the differences between models is their spatial representation, more specifically, the number of dimensions taken into account and the spatial resolution applied to them. The majority of the hydrodynamic and water quality processes is brought about in a three-dimensional environment, however, not always will the modeling of all three dimensions, be relevant to the understanding and representation of the system or the studied process. Thus, the spatial representation boundaries should be defined considering the extent of the gradient to be observed and how important each dimension is from the study perspective (Ji, 2008).

Lakes and reservoirs can be represented by zero-, one-, two- and three-dimensional models (Ji, 2008) (Chin, 2012) (Martins, 2017).

- Zero-dimension: lakes work similarly to a well-mixed reactor, since wind-induced circulation is considered to be strong and the modeled time scale to be long;

- One-dimensional: the relevant gradients are on the vertical dimension, over the depth. The thermal and density profiles can be observed and the interactions between the epilimnion, metalimnion and hypolimnion are modeled.

- Two-dimensional: the 2DV model uses a vertical and a longitudinal dimension defining a plan to analyze the action over the thermal and density profile, as well as the

longitudinal variation; the 2DH model uses to longitudinal dimensions to assess the horizontal variations, representing, for example, the main process on shallow lakes.

- Three-dimensional: as the most complete model, it can simulate complex environments. Thereby, the processes and interactions simulated are the closest to represent reality.

While the number of dimensions determine which gradients will be observed, the spatial resolution defines the model spatial grid. The spatial and temporal resolution relationship affect the equations resolution, altering the accuracy, stability, and efficiency of the model. Therefore, they must be adjusted to increase performance (Ji, 2008).

### 3.4.1 Performance Evaluation

The comparison between measured field data and the output data from a mathematical model allows for the verification of the model, demonstrating its capability to reliably represent the observed processes. Comparing and analyzing data are two essential steps throughout the calibration and validation stages, when alterations on the modeled parameters not only serve to fit the simulated into the observed data, but also help the modelist to gain sensibility towards the model.

Two forms of analysis should be performed by the modelist, over the calibration process, a qualitative and a quantitative one. The qualitative analysis is performed through a visual comparison between the observed and simulated data. It allows the identification of data patterns in time and space and, also, provides a better assessment of the model sensitivity and its physical expressions. On the other hand, the quantitative analysis uses statical indexes to assess the model performance in the light of the measured data (Ji, 2008).

Four of the most common performance indexes, used to assess the quantitatively value of a hydraulic model error, are: Mean Absolute Error (MAE), NMAE (Normalized Mean Absolute Error), Root Mean Square Error (RMSE), Nash Sutcliffe Efficiency (NSE) and the correlation coefficient (r) (Bruce *et al.*, 2018).

$$MAE = \frac{1}{N}\sum_{i=1}^{N}|O_i - S_i| \quad (9)$$

$$RMSE = \sqrt{\frac{1}{N}\sum_{i=1}^{N}(O_i - S_i)^2} \quad (10)$$

$$NMAE = \frac{MAE}{\bar{O}} \quad (11)$$

where N is sample size; $O_i$ is the observed data at a specific time *i*; $S_i$ is the simulated data at a specific time *i*; and $\bar{O}$ is the mean of the observed data for the period.

The MAE index (Equation (9) represents the mean of the absolute difference between observed and simulated data. Its ideal value is zero, indicating no difference between the two datasets. By using the absolute value of the error, the MAE index does not admit the compensation of negative and positive values, avoiding underpredictions, but it also attributes the same weight to all errors, masking large deviations.

In parallel, the RSME (Equation (10), or the standard deviation, represents the averaged squared difference between the observed and simulated data. As the MAE index, its ideal value is zero. This widely applied performance index weights the errors by their deviations; thus, larger differences are more penalized in comparison to smaller ones, increasing the mean error value and exposing the problems. At the same time, the presence of outliers, within the series, and their impact on the RMSE value are a common concern (Ji, 2008) (Bruce *et al.*, 2018).

The NMAE (Equation (11), on its turn, represents the discrepancies presented by the Mean Absolute Error in percentage, related to the mean observed data. Unlike the MAE and RMSE indexes, which provide errors in absolute values, the NMAE, often used in hydrodynamic and water quality modeling, indicates how well the model is performing compared to the mean observed data. However, attention is required when working with large mean observed values, because the index may provide a false sense of accuracy (Ji, 2008).

The NSE index (Equation (12) corresponds to one minus the ratio of the simulated data error variance against the observed data. Its ideal value is 1, indicating that the variance of the simulated series would be 0; whilst if NSE equals 0, the simulated variance would equal the observed variance, suggesting that the prediction capability of the model is as good as the use of the observed mean. The lower limit for the NSE is - ∞ (Mccuen *et al.*, 2006).

$$NSE = 1 - \frac{\sum(S_i - O_i)^2}{\sum(O_i - \bar{O}_i)^2} \quad (12)$$

where $O_i$ is the observed data at a specific time i; and $S_i$ is the simulated data at a specific time i.; and $\bar{O}_i$ is the mean of the observed data.

The r coefficient (Equation (13) calculates the quantitative value for the linear relationship between two variables. This index may vary from -1 up to 1, with its outermost values representing perfect linear relationships (negative for -1 and positive for 1), whereas the middle values, closest to 0, indicate the randomicity of the correlation (Ji, 2008).

$$r = \frac{\sum(O_i - \bar{O}_i)(S_i - \bar{S}_i)}{\sqrt{\sum(O_i - \bar{O}_i)^2}\sqrt{\sum(S_i - \bar{S}_i)^2}} \quad (13)$$

where $O_i$ is the observed data at a specific time i; and $S_i$ is the simulated data at a specific time i.; $\bar{O}_i$ is the mean of the observed data; and $\bar{S}_i$ is the mean of the simulated data.

It is recommended, due to the limitation intrinsic to each error calculation, that the performance evaluation of a model should be done by combining the use of different indexes. (Ji, 2008)

Nevertheless, it is important to point out that a model result is a direct function of the available observed data. In other words, the dataset used for the calibration and validation will bound the simulation once the model parameters ought to be adjusted to better represent that information. Poorly measured field data, outlier events that are not filtered out, time

series periods of lacking data and measurements bias are some of the problems that can create an unreliable model.

### 3.4.2 Governing Principles

Two distinct approaches can be taken towards a fluid motion description, the Lagrangian and the Eulerian. The first proposes the observation of an infinitesimal fluid particle as it moves through a flow field, each property characteristic being determined as a function of time. Whereas, the second approach defines a control volume, a finite region located within the system, where its properties vary in space and time, as a flow field crosses it (Lamb, 1993) (White, 2011).

The Eulerian description is more commonly used to describe fluid motion, yet both can be applied to the formulation of the mechanical fluid governing principles, in a three-orthogonal coordinate system (x, y and z dimensions). The mathematical formulation of each governing principle can be done through a differential (fluid kinematics) or integral (fluid dynamics) method (Martins, 2017).

The three main governing principles regarding the motion of fluids are: Conservation of Mass, Conservation of Momentum and Conservation of Energy.

According to the Mass Conservation principle, within a finite fluid volume, the mass is neither created nor destroyed (Chapra, 2008). Thereby, inside a control volume, the mass variation rate equals the mass flow through its boundaries.

For incompressible fluids, whose density (ρ) is considered constant in time, the Continuity Equation can be simplified to the integral formulation, deducted by the Reynolds Transport Theorem (Equation (14):

$$\left.\frac{dM}{dt}\right|_{System} = \frac{\partial}{\partial t}\int_{\forall C} \rho d\forall + \int_{SC} \rho \vec{V} d\vec{A} = 0 \qquad (14)$$

The Momentum Conservation principle can be formulated applying, into a control volume, the Newton's Second Law. This physical law determines that the momentum variation, as a function of time, within a system, equals the sum of all acting forces.

The integral formulation, once again deducted by the Reynolds Transport Theorem, for the Momentum Conservation principle is (Equation (15):

$$\left.\frac{d(m\vec{V})}{dt}\right|_{System} = \frac{\partial}{\partial t}\int_{\forall C}\rho\vec{V}d\forall + \int_{SC}\vec{V}\rho\overrightarrow{V}d\vec{A} = \sum F \qquad (15)$$

At last, the Energy Conservation principle, based on the first law of thermodynamics, can be described, with Reynolds Transport Theorem, by Equation (16).

$$\left.\frac{dE}{dt}\right|_{System} = \frac{\partial}{\partial t}\int_{\forall C} e\rho d\forall + \int_{SC} e\rho\overrightarrow{V}d\vec{A} = \dot{Q} - \dot{W} \qquad (16)$$

where ρ is the density of the fluid [M/L³]; A is the area of the surface crossed by the velocity vector [M²]; $\overrightarrow{V}$ is the velocity vector [LT$^{-1}$]; g is the gravity acceleration [LT$^{-2}$]; $\forall C$ is the control volume [L³]; $SC$ is the control volume surface area [L²]; E represents the system energy [ML²T$^{-2}$], composed by internal, kinetic and potential parcels; e is the specific energy [L²T$^{-2}$]; Q is the system exchanged heat [ML²T$^{-1}$] and W is the total work [M L²T$^{-1}$]. (Equations (14) to (16))

### 3.4.3 Hydrodynamic Modeling

Based on the governing principles, hydrodynamic lake models solve the water and heat balances, to determine the energy budget within these systems, and, then, apply the advective and diffusive transport methods to assess a property variation over the lentic environment.

#### *3.4.3.1 Water Balance*

The water balance is calculated as the sum of all water sources and sinks within a system. Its solution is supported by the Mass Conservation principle and alters the volume and superficial water level of the lake (Chapra, 2008). The balance main components are: inflows, outflows, precipitation (rain or snow), evaporative losses, watershed runoff and seepage (*Figure 7*) (Equation (17) (Ji, 2008).

$$\frac{dV}{dt} = Q_{inflow} - Q_{outflow} + P * A_s - Evap * A_s - Q_{seepage} + Q_{runoff} \quad (17)$$

where Q is flow [$L^3T^{-1}$]; $A_s$ is the surface area [$L^2$]; P is precipitation [$LT^{-1}$]; and Evap is evaporation mass flux [$LT^{-1}$].

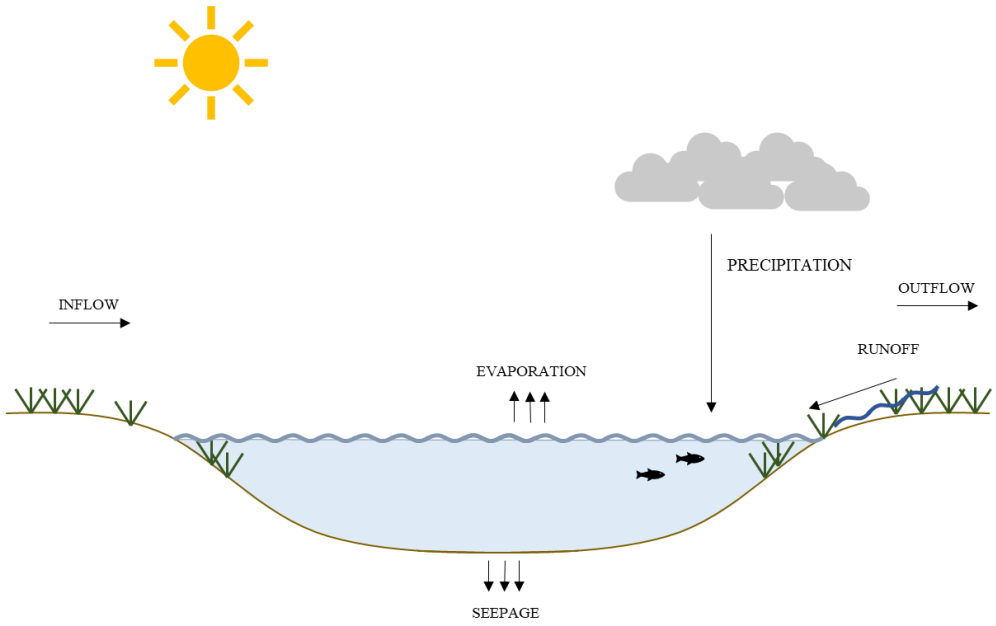


**Figure 7 - Water balance and its main components, in a lentic environment. Source: Author.**

Each component is modeled considering its own characteristics and interactions with the system. The inflows density, velocity and even the slope in relation to the standing water body will affect its intrusion rates and placement (overflow, interflow or underflow) (Hipsey *et al.*, 2019). The outflow depends on the discharge structure, and the seepage is a function of the bottom sediment properties. Meteorological variables and the lake' surface area define the evaporation and precipitation flows, whilst the runoff is a function of the basin area and exposed soil characteristics, like infiltration rate (Ji, 2008) (Imberger, 2013).

In one-dimensional vertical models, in order to solve the hydrodynamic and water-quality equations, the water column is divided into homogeneous layer, each representing a well-mixed reactor (Chin, 2012). The water balance of the system is, then, applied to the volume related with the discharge input (or output) layer (Hipsey *et al.*, 2019).

The evaporation, precipitation and runoff flows are applied to the surface layer. Seepage takes place on the bottom layer. Whereas the inflow and outflow can be admitted into different depths (Imberger and Patterson, 1989) (Hipsey *et al.*, 2019).

#### *3.4.3.2 Heat Balance*

The heat balance corresponds to the total account of the gain and losses of heat by the system, during a defined time period. Its solution is supported by the Momentum and Energy Conservation principles and affects the properties of each homogeneous layer, such as thickness, volume, temperature and density (Chapra, 2008). The balance main components are: advective fluxes (inflows and outflows), superficial heat fluxes (radiation, evaporation and sensible heat exchanges) and bottom heat fluxes (geothermal heat gain or loss) (*Figure 8*) (Equation (18)) (Ji, 2008).

$$\frac{dH}{dt} = H_{inflow} - H_{outflow} + \left(\emptyset_{net} - \emptyset_{Evap} + \emptyset_{H}\right) * A_s \pm \emptyset_{bottom} A_{bottom} \quad (18)$$

where H is heat [$ML^2T^{-2}$]; $A_s$ is the surface area [$L^2$]; $A_{bottom}$ is the bottom later, in contact with the sediment [$L^2$]; and $\emptyset$ is a heat flux [$MT^{-3}$].

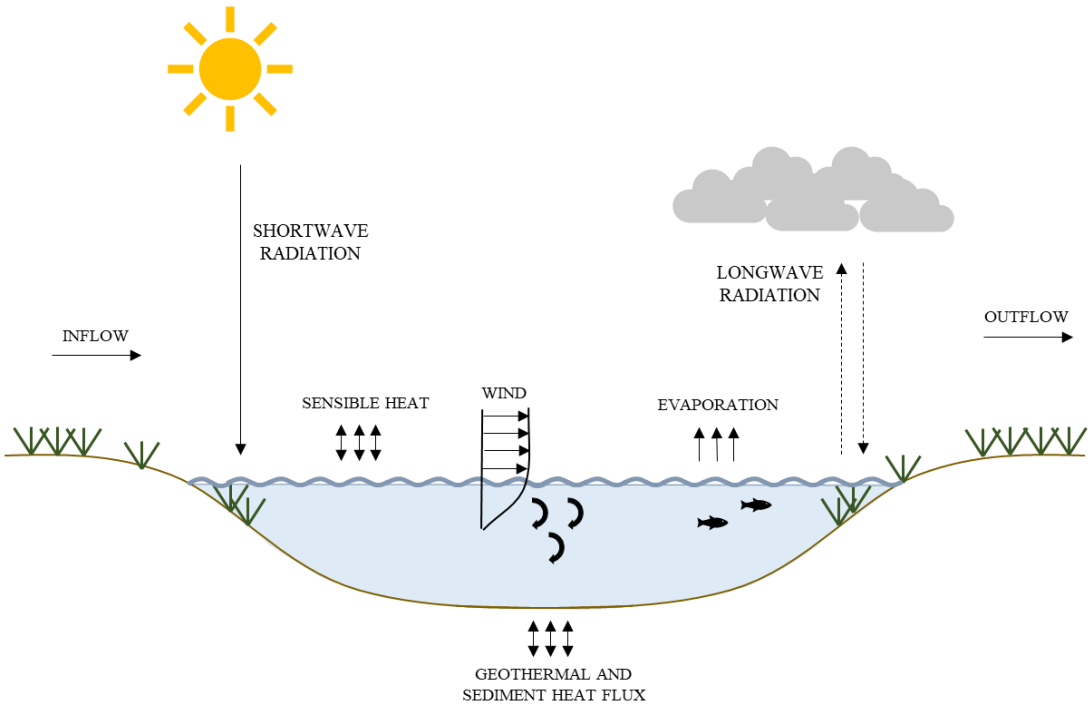


**Figure 8 - Heat balance and its main components, in a lentic environment. Source: Author.**

The surface heat fluxes are the main energy source for standing superficial waters. They can be clustered into three distinct processes: radiation, evaporation and sensible heat exchange.

Solar radiation, as discussed in 3.3.1 Solar Radiation, can be decomposed into short and longwave fractions. The sum of the incident, reflected and emitted portions of these fractions is defined as the net radiation. (Equation (19))

$$\emptyset_{net} = \emptyset_{sw\ incident} + \emptyset_{lw\ incident} - \emptyset_{sw\ reflected} - \emptyset_{lw\ reflected} - \emptyset_{lw\ emission} \quad (19)$$

where $\emptyset$ is a heat flux [$MT^{-3}$]; sw stands for shortwave radiation and lw for longwave radiation.

Modeling the net heat flux, involves the characterization of each radiation component. The shortwave heat flux is discussed as a function of its albedo (the percentage of the radiation that is reflected), the total incoming shortwave radiation, the water depth it is able to reach

and the fluid light extinction coefficient (Kw) (3.3.1 Solar Radiation) (Equation (20)) (Chapra, 2008) (Hipsey *et al.*, 2019).

$$\emptyset_{sw\,(z)} = (1 - \alpha_{sw})\emptyset_{sw} e^{-Kwz} \quad (20)$$

where ∅ is a heat flux [$MT^{-3}$]; $\alpha_{sw}$ is the shortwave radiation albedo [dimensionless]; $K_w$ is the light extinction coefficient [$L^{-1}$] and z is depth [L].

The longwave heat flux (Equations (21 and (22) is, also, a function of its albedo, as well as the air temperature, air and water emissivity coefficient (incident and emitted longwave, respectively) and the Stefan-Boltzmann constant (σ = 5.6704x$10^{-8}$ W/m²K) (Chapra, 2008) (Hipsey *et al.*, 2019).

$$\emptyset_{lw\,incident} = (1 - \alpha_{lw})\varepsilon_a \sigma [T_a + 273.15]^4 \quad (21)$$

$$\emptyset_{lw\,emission} = \varepsilon_w \sigma [T_w + 273.15]^4 \quad (22)$$

where ∅ is a heat flux [$MT^{-3}$]; $\varepsilon$ is the emissivity coefficient [dimensionless]; $T_a$ is the air temperature [Θ], $T_w$ is the water temperature [Θ] and σ is the Stefan-Boltzmann constant [$MT^{-3}\Theta^{-1}$].

The latent heat flux, or the evaporation, can be formulated by the Equation (23). It is subjected to the air density, the water latent heat of vaporization, wind velocity (measured 10 m from the surface), molecular weight ratio of water to air, atmospheric pressure and the air and saturation vapor pressure (both depended on the air temperature and relative humidity) (Ji, 2008). The flux equation proposes, as a calibration parameter, the coefficient $c_e$ defined as the bulk aerodynamic coefficient for latent heat transfer. Fischer suggests a $c_e$ value of 0.0013 (Fischer *et al.*, 1979) (Hipsey *et al.*, 2019).

$$\emptyset_{Evap} = -\rho_a c_e \lambda_v U_x \frac{k}{p} (e_s[T_s] + e_a[T_a]) \quad (23)$$

where ∅ is a heat flux [$MT^{-3}$]; $\rho_a$ is the air density [$ML^{-3}$]; $c_E$ is the bulk aerodynamic coefficient for latent heat transfer [dimensionless]; $\lambda_v$ is the water latent heat of vaporization [$L^2T^{-2}$]; $U_x$ is the wind velocity [$LT^{-1}$]; k is the molecular weight ratio of water to air [dimensionless]; p is atmospheric pressure [$ML^{-1}T^{-2}$]; e is the vapor pressure [$ML^{-1}T^{-2}$]; and T is temperature [Θ].

Along with the previous formulation, the sensible heat flux can be modeled using Equation (24). Its parameters are the air density, the water specific heat capacity, wind velocity (measured 10 m from the surface), and the difference between the surface water and the air temperatures. Used as a calibration parameter, the coefficient $C_H$ is defined as the bulk aerodynamic coefficient for sensible heat transfer. Fischer also suggests a value of 0.0013 for the $C_H$ (Fischer *et al.*, 1979).

$$\emptyset_H = -\rho_a c_p c_H U_x [T_w - T_a] \quad (24)$$

where ∅ is a heat flux [$MT^{-3}$]; $\rho_a$ is the air density [$ML^{-3}$]; $c_H$ is the bulk aerodynamic coefficient for sensible heat transfer [dimensionless]; $c_p$ is the water specific heat capacity [$L^2T^{-2}\,\Theta^{-1}$]; $U_x$ is the wind velocity [$LT^{-1}$]; and T is temperature [Θ].

At last, the heat flux at the bottom of the lake can be modeled by the Equation (25), considering the soil-sediment thermal conductivity, the temperature difference in the water-soil interface and the length scale associated with the heat (Ji, 2008) (Hipsey *et al.*, 2019).

$$\emptyset_{bottom} = K_{soil} \frac{[T_w - T_s]}{\delta z_{soil}} \quad (25)$$

where ∅ is a heat flux [$MT^{-3}$]; $K_{soil}$ is the soil-sediment thermal conductivity [$MLT^{-3}\,\Theta^{-1}$]; $\delta z_{soil}$ is the length scale associated with the heat flux [L]; and T is temperature [Θ].

The inflow and outflow provide the advective heat fluxes for the system. Therefore, both equations (Equation (26)) are a function of the discharge flow and temperature, the water specific heat capacity and the fluid density.

$$H_{\ inflow/outflow} = Q\rho c_p T_{in} \quad (26)$$

where H is a heat [$ML^2T^{-2}$]; Q is the discharge flow [$L^3T^{-1}$]; $\rho$ is the water density [$ML^{-3}$]; $c_p$ is the water specific heat capacity [$L^2T^{-2}\ \Theta^{-1}$]; and T is temperature [$\Theta$].

### *3.4.3.3 Constituents Transports*

Regarding the transport of a property, conservative or not, the advection and diffusive transports methods, defined in 3.2.2 Mixing events, are used. They can be modeled employing the discrete form of the Continuity Equation, with the variable φ representing the constituent sources and sinks (Martins, 2017).

The advection transport of a general property (C), on a three-dimensional system, is governed by the fluid velocity field (Equation (27)). Whereas, the diffusive transport uses the diffusion coefficient (E), defined by the first and second law of Fick, to account for the molecular and turbulent aspects of the property dispersion. (Equation (28)) The diffusion coefficient value can be estimated by different methods, such as: average dissipation rates of total KE, stability numbers, shear velocity due to wind stress, heat fluxes assessment (Saber *et al.*, 2018).

For practical purposes, even though the diffusion coefficient has different values in each dimension and at distinct stability conditions, a single value can be applied for the whole system considering almost isotropic environments (Martins, 2017).

$$\frac{\partial C}{\partial t} + u\frac{\partial C}{\partial x} + v\frac{\partial C}{\partial y} + w\frac{\partial C}{\partial z} = \pm\varphi \quad (27)$$

$$\frac{\partial C}{\partial t} - E_x\left(\frac{\partial^2 C}{\partial x^2}\right) - E_y\left(\frac{\partial^2 C}{\partial y^2}\right) - E_z\left(\frac{\partial^2 C}{\partial z^2}\right) = \pm\varphi \quad (28)$$

Considering both transports (Equation (29):

$$\frac{\partial C}{\partial t} + u\frac{\partial C}{\partial x} + v\frac{\partial C}{\partial y} + w\frac{\partial C}{\partial z} - E_x\left(\frac{\partial^2 C}{\partial x^2}\right) - E_y\left(\frac{\partial^2 C}{\partial y^2}\right) - E_z\left(\frac{\partial^2 C}{\partial z^2}\right) = \pm\varphi \quad (29)$$

where x, y and z are the system coordinate dimensions [L]; u, v and w are the velocity components for each dimension [$LT^{-1}$]; C is a general property of the system [dimension]; φ represents the sources and sinks of the property [dimension $T^{-1}$]; and $E$ is the diffusion coefficient [$L^2T^{-1}$].

On one-dimensional vertical models, the variations of a water property (i.e., temperature, density or a constituent concentration) can be assessed through the resolution of the advective and diffusive transports equations. The sources and sinks will vary in regard of the constituent. For example, for the temperature gradients evaluation across the system, the sources and sinks are described by the heat balanced discussed in 3.4.3.2 Heat Balance. (Chin, 2012)

Thereby, considering the relation between the temperature and the heat, expressed by Equation (30), the complete temperature transport formulation is presented in Equation (31).

$$T = \frac{H}{\rho c_p V} \tag{30}$$

$$\frac{\partial T}{\partial t} = -w\frac{\partial T}{\partial z} + Ez\frac{\partial^2 T}{\partial z^2} + \frac{\left[H_{inflow} - H_{outflow} + \left(\emptyset_{net} - \emptyset_{Evap} + \emptyset_H\right) * A_s \pm \emptyset_{bottom} A_{bottom}\right]}{\rho c_p V} \tag{31}$$

where H is a heat [$ML^2T^{-2}$]; V is volume [$L^3$]; $\rho$ is the water density [$ML^{-3}$]; $c_p$ is the water specific heat capacity [$L^2T^{-2}\,\Theta^{-1}$]; T is temperature [Θ]; ∅ is heat flux [$MT^{-3}$]; A is area [$L^2$]; t is time [T]; w is vertical velocity [$LT^{-1}$]; $Ez$ is the vertical diffusion coefficient [$L^2T^{-1}$]; and z is the vertical dimension [L]

In a strongly stratified environment, the vertical velocity component (w) may not be expressive, as so does the diffusive parcel, which has a hard time competing with the buoyancy forces. Thus, in the discussed environment, the temperature will vary in time, primarily, due to the external inputs and output.

## 3.5 CLIMATE CHANGE IMPACTS ON LENTIC ENVIRONMENTS

As discussed throughout this chapter, lakes and reservoirs hydrodynamic processes are driven by the relationship between basin characteristics and the local meteorological conditions. In this context, climate change has been arising concerns among scientists towards possible future impacts onto these environments' dynamics.

According to Adrian et al. (2009), lakes can be considered sentinels of climate since (1) their environment are well defined and studied in sustained fashion, (2) they respond to climate change variables, not only the ones that directly affect the water body, but also the ones that drive changes within its catchment area, (3) lakes are able to integrate responses over time, filtering random noises, and (4) their worldwide distribution allows them to respond to different climates and geographic locations, capturing different aspects of the phenomena.

Hereupon, to assess, correlate and compare the impacts of climate change scenarios onto lakes, the selection of the proper indicator is fundamental for the analysis.

Once the atmospheric variables are responsible for triggering a physical, chemical and/or biological response onto the system, the indicators are usually set as a measurable response variable, such as water temperature, dissolved oxygen or algae population.

Adrian et al. (2009) discussed and proposed indicators to compose this analysis. However, the efficacy of many indicators is affected by regional responses to climate change, the catchment characteristics and the lake mixing regimes. Therefore, combining indicators can be more effective and help overcome some of the limitations.

In the water balance analysis, its main components (precipitation, inflow, outflow and runoff), discussed in 3.4.3.1, have their flow rate directly affected by the precipitation regime across the watershed, whereas the evaporation flow depends on the air temperature, relative humidity, wind and the presence of aerosols, increasing proportionally to them. These variables impact on the volume and water level of the lake, prompting both responses as indicators (Rocha Junior *et al.*, 2018).

In this analysis, the operation of regulated reservoirs, which may influence the water balance dynamic, is a limitation. Groundwater levels, changes in vegetation and in the land use of the

catchment area are also considered cofounding factors and may influence the indicators (Adrian *et al.*, 2009).

The heat balance, on its turn, discussed in 3.4.3.2, is mainly affected by rising air temperatures and changes in the wind conditions. These drivers are responsible for important heat fluxes taking place at the lake surface, as the evaporation and sensible heat (Equations (23) and (24)). Air temperatures can, also, alter the longwave incidence and emission, as so the inflow temperatures. Whereas wind conditions influence current formations, shear production and, thus, the total energy budget of the upper layer.

Therefore, for the heat balance, a usually applied indicator is the water temperature, at distinct depths. The epilimnion temperature, or surface temperature, can be strongly correlated to variations in the air temperature and wind conditions. As for the hypolimnion temperature, or bottom temperature, the direct correlations with the air temperature and wind variations are not as strong, with the morphology of the lake, sediment characteristics and light penetration conditions having to be taken into account for the thermal structure assessment. However, both layers can be understood as an indicator of the lake energy integration over time.

The relation between both layer temperatures affects the water density profile and, with that, the thermal gradient of the lake. Long-term changes in the thermal structure can be responsible for significant and lasting alterations in the mixing regime of the lake. As indicators, the increase of the density profile stability can be assessed by the Schmidt Stability number, the depth of the thermocline or by the duration of summer stratifications. The limitations over these indicators are their dependency over the lake's morphology and transparency (for small lakes), and the difficulties in obtaining high spatial and temporal resolution data (Read *et al.*, 2011).

Since even a small increase in the overall temperature of a water volume results on the strengthening of the density gradient, buoyancy forces and the vertical stability, it is expected that most climate change scenarios will reveal a positive bias towards the occurrence of stratification events (Adrian *et al.*, 2009).

In small, shallow lakes these impacts are even more pronounced, due to the onset of strong vertical stability, their mixing regime can suffer significant changes; shifting, for example,

in a century-long period, from being a polymictic environment into becoming a monomict one (Kirillin, 2010).

Regarding lentic environments, climate change assessment studies indicate the reduction on the number of overturning events, intensification of stratification, with an increase on the number of days in this condition and on the required energy to break the density gradient created. Thereby, altering the thermal patterns once observed. (Kirillin, 2010) (Woolway *et al.*, 2017) (Huang *et al.*, 2017) (Farrell *et al.*, 2020)

Kirillin (2010) and Farrell et al. (2020) suggest the air temperature as the main proxy for the prediction of thermal changes, whilst Huang et al. (2017) also accounts for the longwave radiation influence. Woolway et al. (2017), on the other hand, proposes the reduction of wind, due to the atmospheric stilling processes, as the main parameter.

Kirillin (2010) and O'Reilly et al. (2003) applied, as indicators, the water temperature on the surface and bottom layer, as did Huang et al. (2017), with addition to the thermocline depth, number of stratified days and the start day of the stratification. Woolway et al. (2017) and Woolway et al. (2019) also used the epilimnion water temperature for analysis, and, the former complemented with the ice cover duration assessment. (O'reilly *et al.*, 2003) (Kirillin, 2010) (Woolway *et al.*, 2017) (Huang *et al.*, 2017) (Woolway and Merchant, 2019)

These climate dynamics, in addition to anthropogenic actions, impact not only the physical processes, but also chemical and biological characteristics of a lake. Some observed and predicted impacts are: the increase of nutrient and organic matter concentrations, as the volume of the lake is reduced, with disturbances on their cycling because of the stronger stratification patterns; with that, also, the reinforcement of a hypolimnion layer with higher potential to set anoxia events; the reduction on phytoplankton productivity; algae blooms and the intensification of eutrophication processes. (O'reilly *et al.*, 2003) (Menezes *et al.*, 2019) (Woolway *et al.*, 2017) (Rocha Junior *et al.*, 2018) (Farrell *et al.*, 2020) (Ladwig *et al.*, 2021)

In this scenarios, mathematical modeling can be an important tool for simulating, forecasting, and assessing future climate change conditions and their impacts on lentic environments. To adapt the systems and mitigate problems, decision-makers relying on hydrodynamic models are able to better understand the long-term responses of these environments to climate

change, assess the different impacts, then, propose and evaluate solutions for problems that already exist or that are yet to come.

# 4 THE GENERAL LAKE MODEL

This chapter introduces the 1D mathematical model General Lake Model (GLM). Its worldwide applications as well as Brazilian study cases are reviewed. The model overview is discussed, focusing on the mathematical approach applied for the assessment of the water and energy balance of a lake. Other 1D models are briefly presented.

Therefore, this chapter aims to provide information of the model's approach, limitation and biases to, then, address the third specific objective of this study over the next chapters.

## 4.1 THE GENERAL LAKE MODEL (GLM)

The General Lake Model is a one-dimension hydrodynamic model developed by the Aquatic EcoDynamic (AED) group of the University of Western Australia (UWA), in order to support the Global Lake Ecological Observatory Network (GLEON) initiative.

Aiming to create a global scientific community interested in observing, understanding, predicting and discussing the impacts of changing environments on lakes, through data sharing and experience exchanges, the GLEON project instigate and support the modeling of lentic environments around the globe (Bruce *et al.*, 2018) (Gleon, 2020). The GLM model, in this context, can be seen as a successful collaborative initiative.

Bruce et al. (2018) used data from a global observatory network to stress-test the GLM against 32 different lakes across the globe. The thermal dynamic simulation of the model was performed over a large range of freshwater environments, with distinct specific characteristics, to assess the model transferability (the main heating and mixing parameters were set to default values), its reliability in light of the input data uncertainties and the sensitivity analysis for nine dynamic parameters on local and global scales. Read et al. (2014) simulated 2368 temperate lakes with the GLM model, within a 33-year time interval, studying the regional coherence of stratification phenology. The model was fed with open-source data, for input variables, and residence time, light extinction and wind drag coefficient

of each lake. Results showed weak coherency between stratification events, indicating the role of regional and local heterogeneity on the thermal responses of lakes to changing conditions (Read *et al.*, 2014) (Bruce *et al.*, 2018).

As the GLM model is able to perform long-term simulations, with low computational requirements, its application to changing climate analysis, past and future, has great scientific value, fostering the understanding of lakes' thermal patterns variations and their ecological impacts. Huang et al. (2017) investigate the lake Nam Co, located on the Tibet Plateau, over a simulated period from 1979 to 2012, observing the increase tendency in the surface-layer temperature (0.52 ± 0.25°C per decade), along with the earlier occurrence of stratification onsetting, the expansion of the stratified days period and the shallowing of thermocline depths. Whereas, Farrell et al. (2020), through the GLM model application, coupled with the Aquatic EcoDynamic (AED) library, provided the analysis over the effects of climate warming on nutrient cycling in two distinct lakes: Lake Mendota (Wisconsin, USA) and Sunapee (New Hampshire, USA). During an 11-year simulation period, the study quantified the climate warming effects, of air temperature elevation (scenarios from +1°C up to +6°C), through the timing and duration of anoxia events on the hypolimnion (related to earlier and longer stratification), and the changes in nitrogen and phosphorus concentrations over the water column. Ladwig et al. (2021), also studying Lake Mendota (Wisconsin, USA), identified the main drivers of the lake's summer hypolimnetic anoxia events, over a 37-year simulation period, in order to assess the interannual variability of these events characteristics. (Huang *et al.*, 2017) (Farrell *et al.*, 2020) (Ladwig *et al.*, 2021)

In the Brazilian context, the GLM model has been used, for the past few years, to assess lakes and reservoirs' s thermal regimes, their main driving parameters, and the impacts on chemical and biological conditions. Silva et al. (2015) modeled the Pampulha Lake (Minas Gerais, Brazil), between 2011 and 2013, evaluating the impact of runoff inflow water on a tropical lake and demonstrating its correlation to the water column mixing and algae growth disruption, during wet seasons. On the other hand, Soares et al. (2017) studied the Serra Azul reservoir (Minas Gerais, Brazil) during drought periods, simulating years from 2009 to 2016, and indicating the reduction of the annual mean temperature over the water column and the intensification of mixing events. Pinto (2018) evaluated the influence of rainfall and air temperature variations over the thermal regime of the Descoberto reservoir (Distrito Federal,

Brazil). While, Sales (2020) modeled the thermal, chemical and biological regimes of the Passaúna reservoir (Paraná, Brazil), from 2017 to 2019. (Silva *et al.*, 2015) (Soares *et al.*, 2017) (Pinto, 2018) (Sales, 2020b)

Soares et al. (2020) carried out a study over a subtropical cascade on the Tietê river basin (São Paulo, Brazil), analyzing six different reservoirs, in order to perform a sensitivity analysis, simulate their thermal regimes (2009-2016) and, finally, propose a parametrization strategy for non-monitored reservoirs (the case of two of them) through regression curves application, based on the surface heat calibration of the monitored reservoirs. (Soares *et al.*, 2020)

Biological features have been modeled, through the GLM coupled library AED. Pujoni (2015) performed a sensitivity analysis of the light extinction coefficient (Kw) over the thermal regime of two lakes (Carioca and Gambazinho), from the Vale do Rio Doce lacustrine system (Minas Gerais, Brazil), aiming to assess the impact over phytoplankton community. Barbosa (2015) simulated the water quality and phytoplankton (blue and green algae) dynamics on the Paranoá Lake (Distrito Federal, Brazil), during the 2007-2009 period. Results showed good model performance for the thermal regime and phytoplankton concentrations, however, the other water quality parameters were not considerate suitable for the environment representation. At last, Soares (2018) performed simulations over the Serra Azul reservoir (Minas Gerais, Brazil) drought period in order to assess the thermal regime variations and the impacts on the biomass and composition of phytoplanktonic communities along the water column. The modeling results indicated the disruption of the former thermal regime (monomict) into a new one (polymictic), prompting the decrease of water quality conditions (increase of conductivity, turbidity, total solids and nutrients concentrations) and, thus, the alteration on the prevailing phytoplankton composition (from blue to green algae) and reduction of total biomass. (Pujoni, 2015) (Barbosa, 2015) (Soares, 2018)

Valid for the simulation of stratified and mixed columns, on environments where it is possible to assume the density vertical structure is the dominant one, while the horizontal profile is homogeneous, the GLM hydrodynamic model uses a deterministic, mechanistic, time-

dependent and numerical solving approach. (Hipsey *et al.*, 2019). As an open-source model, its code, written in C programming language, is freely available online and can be downloaded, compiled, and even changed. The R (R Core Team, 2020) and Matlab (**The Mathworks**, 2012) programming languages are extensively used for compiling the model, because they hold a series of developed packages to better run, calibrate and validate it, as so to visualize and post process its results (Read *et al.*, 2011) (Bueche *et al.*, 2020).

Furthermore, different platforms hold GLM modeling groups (Google groups, Slack, GitHub), with scientists exchanging experiences and helping each other into solving problems, which includes the original GLM developers. The free access to these groups, along with online workshops, published papers about the model structure and a very helpful website (Uwa, 2021), helps the fostering of a GLM global modeling community.

### 4.1.1 Model Overview

Based on the dynamic principles and structures proposed by Imberger and Patterson (1981), Hamilton and Schlandow (1997) and Chung et al. (2008), the GLM numerical model uses a flexible Lagrangian structure to solve the water and energy balance over a vertical dimension, simulating stratification and mixing processes (Imberger and Patterson, 1981) (Hamilton and Schladow, 1997) (Chung *et al.*, 2008) (Hipsey *et al.*, 2019).

The water column is divided into several homogeneous layers, of different thicknesses, in response to the vertical density gradient. The layers thickness varies dynamically over time, in order to better represent the gradient profile at place. Thereby, the vertical grid of the model may be refined near the depth of the thermocline, during a stratification event, for example, or expanded during mixing. The number of layers and their thickness are altered considering the inputs and outputs of mass and energy, along with the dynamic processes acting on the adjacent layers (Hipsey *et al.*, 2019).

Since the one-dimensional approach is used, the water column dynamic can be considered as a representation of the whole lake dynamic, and, thus, in order to properly scale it, the volume of each layer is determined by the local hypsographic curve, provided by the user. The overall volume of the lake is, then, calculated as the sum of each layer's volume (Equation (*32*), i.e., the integration of the area-height relationship (Hipsey *et al.*, 2019).

$$V_{máx} = \int_{h_0}^{h_{máx}} A\,[h]dh \qquad (32)$$

where $V_{máx}$ is the total volume [L³]; h is the water height (from the bottom of the lake) [L]; and A is the basin area of the lake, at the selected height [$L^2$].

Throughout the simulated time frame, the lake's water and energy balances (*Figure 9*) are solved at two distinct time resolutions. The GLM code is structured to firstly perform, hourly, all the surface fluxes, the mixing processes on the epilimnion, check the layers stability, calculate the diffusive processes bellow the thermocline and run the water quality simulations, then, afterward, to perform daily fluxes. At each time step, the respective fluxes are solved by their integration over time (Hipsey *et al.*, 2019).

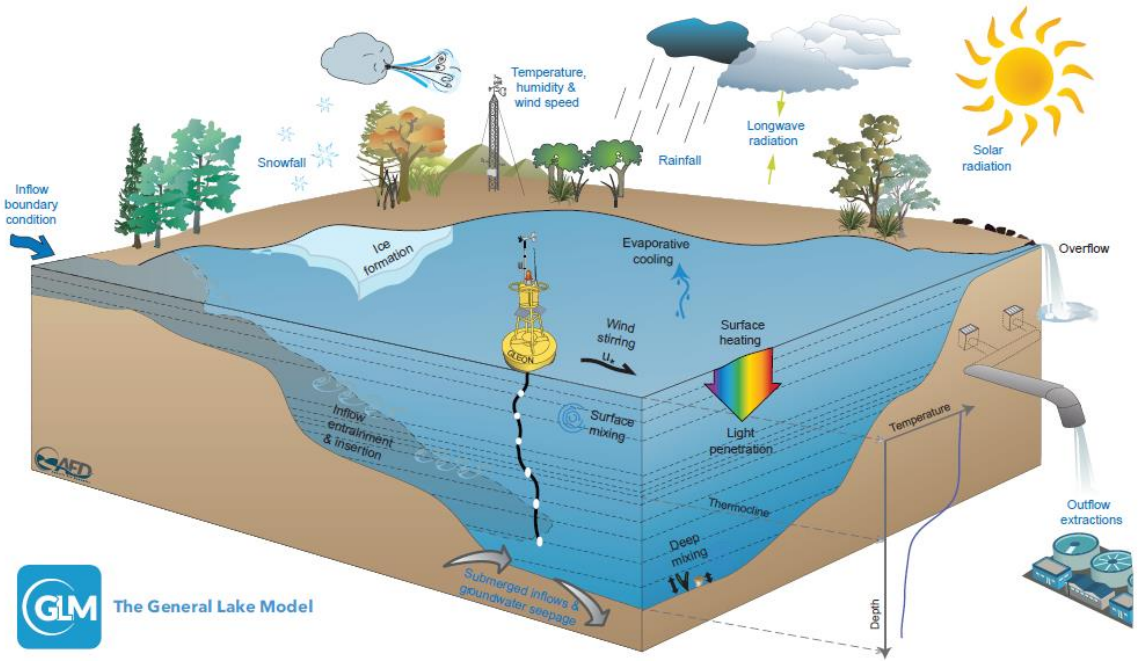


**Figure 9 - Schematic of a GLM simulation domain, input information (blue text), and key simulated processes (black text). Source: (Hipsey *et al.*, 2019).**

### *4.1.1.1 Water Balance*

The total water balance is governed by the same components and parameters discussed in 3.4.3.1 Water Balance. However, the GLM model computes the evaporation, precipitation and

runoff (surface fluxes) at an hourly time step and the inflows, outflows and seepage at daily intervals.

At the surface, evaporation mass fluxes are modeled by Equation (33), whereas the precipitation is an input data, provided along with the meteorological file, and can account for rain and snow. The runoff varies with the rain, the exposed bank area of the lake's basin, a threshold value (above which the rainfall will be considered as effective to the process) and a runoff coefficient (defining the fraction of rain transformed into runoff) (Equation (*34*)). With the runoff coefficient set to 0, this flux will not be considered.

$$Evap = \frac{\emptyset_{Evap}}{\rho_{surf}\ \lambda_v} \tag{33}$$

$$Q_R = max\ [0, f_{ro}\ \left(R_F - \frac{R_L}{c_{secday}}\right)](A_{máx} - A_s) \tag{34}$$

where Evap is evaporation mass flux [$LT^{-1}$]; $\emptyset$ is a heat flux [$MT^{-3}$]; $\rho_{surf}$ is the surface water density [$ML^{-3}$]; $\lambda_v$ is the water latent heat of vaporization [$L^2T^{-2}$]; $Q_R$ is the runoff flow [$L^3T^{-1}$]; $f_{ro}$ is the runoff factor [dimensionless]; $R_F$ is the rainfall intensity [$LT^{-1}$]; $R_L$ is the rainfall threshold [$LT^{-1}$]; $c_{secday}$ is the number of seconds per day (86400 s/day) [dimensionless]; $A_{máx}$ is the maximum basin area [$L^2$]; and $A_s$ is the surface area [$L^2$] of the lake.

At the daily time step, the inflows, outflows and seepage are considered. The inflows are required input data, characterized by flow, temperature and salinity. They can be defined as one or more rivers entering at the surface of the lake or as submerged inflows, contributing with water mass and kinetic energy.

For river entrances at the surface, the GLM model uses the provided temperature and salinity data to calculate the water flow buoyancy force in relation to the density profile set at the time. The inflow is considered to deepen until it reaches a neutral buoyancy depth, where it can be inserted into the water column. During its descends, the flow entrains water from the layers it crosses, increasing in volume and altering its density characteristics. Equations (35), (36) and (37) calculate the entrainment rate and the increase in thickness in response to it,

considering geometrical river parameters as the stream cross section half angle and slope. At each time step (daily) the inflow is estimated to increase as Equation (38).

$$E_{inf} = 1.6 \frac{C_{D\ inf}^{3/2}}{Ri_{inf}} \tag{35}$$

$$\Delta z_{inf_i} = 1.2 E_{inf} \Delta x_{inf} + \Delta z_{inf_{i-1}} \tag{36}$$

$$\Delta x_{inf} = \frac{\delta z_{inf_i}}{sin\beta_{inf}} \tag{37}$$

$$\Delta Q_{inf_i} = \Delta Q_{inf_{i-1}} \left[ \left( \frac{\Delta z_{inf_i}}{\Delta z_{inf_{i-1}}} \right)^{5/3} - 1 \right] \tag{38}$$

where $E_{inf}$ is the entrainment coefficient [dimensionless]; $C_{D\ inf}$ is the drag coefficient of the inflowing water [dimensionless]; $Ri_{inf}$ is the Richardson number of the inflowing water (characterized by the channel geometry) [dimensionless]; $\Delta z_{inf}$ is the intrusion thickness [L]; $\Delta x_{inf}$ is the distance travelled by the inflowing water parcel [L]; $\delta z_{inf_i}$ is the vertical distance travelled by the inflowing particle [L]; j is the time step [T]; $\beta_{inf}$ is angle of the slope of the inflow thalweg relative to horizontal [degree]; $\Delta Q_{inf}$ is the flow increment due to entrainment over the ith time step [$L^3T^{-1}$].

Once the inflow reaches the depth of buoyancy neutrality, its volume is inserted as a new layer with the same characteristics and a corresponding calculated thickness. The new layer will, then, be updated accordingly with the interaction within its neighbors, merging or splitting.

Submerged inflows, on the other hand, are applied at specific depths and change the corresponding volume and energy of the layer.

Four different types of outflows can be determined within the model. Specific depth withdraws, adaptative offtakes, vertical groundwater seepage and the overflow-outflow from the surface.

Specific depth withdraws represent a variety of structures, such as dam wall offtakes and piped water withdraws. At every time step, the provided discharge is removed from the specific-depth layer. However, in stratified environments, the outflow thickness may vary due to the flow strength and the water column stability, expanding, and, therefore, pulling water from the adjacent layers. As a step further, the adaptative offtakes allow the user to set a predefined range of possible heights and specify a target property (as the temperature, oxygen concentration, etc.), so the model is able to change the withdraw depth, in response to the stratified structure. This method can help on reservoirs management and ecological planning.

Seepage flux can be computed as a constant value or be defined by a Darcy flux, based on the water height. The water withdraw takes place at the bottom layer; however, the model ensures that, within a single time step, no more than 90% of this layer volume can be reduced. If that is the case, water will be drained from the upper layers towards the bottom. As the runoff, the seepage is an optional setting, and can be ignored once its coefficient is set to zero.

The surface overflow is due to the increase of the water level beyond the maximum height of the lake, defined by the height-area-volume curve, and, thereby, corresponds to all the exceeding volume that has to be discharged. The user can, also, define a surface outflow through a weir structure. The weir structure is described by a crest elevation (which lies lower than the maximum lake height) and a height-flow rating curve. (Equation (*39*)). The total overflow is expressed through Equation (40).

$$Q_{weir} = \begin{cases} 0, & V_s^* \leq V_{crest} \\ \frac{2}{3} c_{D_{weir}} \sqrt{2g} W_{weir} (h_s^* - h_{crest})^{\frac{3}{2}}, & V_s^* \geq V_{crest} \end{cases} \quad (39)$$

$$Q_{ovfl} = f(x) = \begin{cases} Q_{weir}, & V_s^* \leq V_{crest} \\ Q_{weir} + (V_s^* - V_{max})/\Delta t, & V_s^* \geq V_{crest} \end{cases} \quad (40)$$

where $Q_{weir}$ is the flow over the spillway crest [$L^3T^{-1}$]; $V_s^*$ is the volume of the lake prior to the overflow interaction [$L^3$]; $V_{crest}$ is the volume of the lake at the crest height [$L^3$]; $c_{D_{weir}}$ is the weir drag coefficient [dimensionless]; g is the gravity acceleration [$LT^{-2}$]; $W_{weir}$ is the width of the weir crest [L]; $h_s^*$ is the water surface height prior to the overflow [L]; $h_{crest}$ is the crest height [L]; $Q_{ovfl}$ is the overflow [$L^3T^{-1}$]; $V_{max}$ is the maximum volume of the lake [$L^3$]; and $\Delta t$ is the time step (daily) [T].

In summary, the lake's water balance is governed by several components. At an hourly time-step, the surface fluxes (runoff, evaporation and precipitation) are computed, altering the water level. At the end of a sub-daily loop, the integration of all hourly variations is computed and the inflows, outflows and seepage are accounted for, changing the overall volume of the lake. Depending on the inflow characteristics (density equal to or lower than the surface layer), it can be processed as a daily surface flow, also impacting on the water level.

#### *4.1.1.2 Energy Balance*

Two distinct approaches are applied to simulate mixing dynamics by the GLM model, the energy balance and the vertical diffuse transport. The first is applied to the surface mixed-layer (or the epilimnion), while the second performs the "deep mixing" process, i.e., the mixing below the thermocline.

On the surface mixed-layer, the energy balance is solved comparing the available kinetic energy, produced by convective overturn (in response to cooling), wind stirring and shear stress at the thermocline, to the required kinetic energy to trigger a mixing event. For that, at hourly intervals, the code compiles each energetic related process as sequential steps: (1) Heating; (2) Cooling and wind stirring; (3) Shear production and Kevin-Helmholtz (KH) billowing.

**(1) Heating**

Surface heating can be described by the same components and fluxes presented at (*Figure 8*): radiation, evaporation and sensible heat exchanges. Their modeling is similar to the Equations (18) to (31), already discussed, with the multiplication of a scaling factor to correct the inputted meteorological data (*Figure 9*).

Within the model, the solar radiation values can be provided by the user, through the meteorological file, in daily or hourly intervals, or calculated by a coupled routine called Bird Clear Sky Model (BCSM), which uses the global position of the lake, atmosphere constitution and surface albedo to predict the incoming radiation (Hipsey *et al.*, 2019).

The shortwave radiation (Equation (*41*) is computed by an adaptation to the Equation (20), accounting for a scaling factor for the inputted data ($f_{sw}$) and considering, only, the fraction of photosynthetically active radiation (about 45% of the incident light), with the $f_{PAR}$ factor. The $Kw$ can be provided as a constant value or, if the model is coupled with an ecological module, as a time series. Also, the shortwave albedo value can be calculated by one of three distinct methods, selected by the user.

$$\emptyset_{sw\,(z)} = f_{sw} f_{PAR} (1 - \alpha_{sw}) \emptyset_{sw} e^{-Kwz} \tag{41}$$

where $\emptyset$ is a heat flux [$MT^{-3}$]; $f_{sw}$ is the scaling factor for shortwave radiation [dimensionless]; $f_{PAR}$ is the photosynthetically active radiation factor; $\alpha_{sw}$ is the shortwave radiation albedo [dimensionless]; $K_w$ is the light extinction coefficient [$L^{-1}$] and z is depth [L].

Longwave radiation, sensible heat exchange and latent heat flux are modeled as proposed by the Equations (21), (22), (23) and (24), discussed previously. However, the longwave emissivity coefficient calculation method, as well as the vapor pressure, at the latent heat equation, can be opted by the user.

**(2) Convective Overturn and Wind Stirring**

Once the heating is compiled, the mixing dynamics take place. The available kinetic energy of the surface mixed-layer is compared to the kinetic energy required to lift up the water set bellow the bottom of this layer and accelerate it to the mixed-layer velocity. Physically, this energy balance indicates if the advective and turbulent forces can overcome the buoyancy forces on the metalimnion, breaking the density gradient at the layers interface.

Convective overturn, wind stirring, shear production and the Kevin-Helmholtz instabilities are the accounted sources of kinetic energy. Based on Imberger and Patterson (1981) algorithm, the convective overturn (due to cooling) is modeled by the vertical turbulent velocity scale, $w_*$, and the mixing efficiency coefficient for convection overturn $C_K$. During the deepening process of the mixed-layer, the momentum associated to each layer merged into the epilimnion is summed. The available convective energy parcel is determined by Equation (42) (Hipsey *et al.*, 2019).

$$E_{conv} = 0.5\, C_K (w_*^3) \Delta t \tag{42}$$

where $w_*$ is the turbulent velocity scale [$LT^{-1}$]; $\Delta t$ is the time step (hour) [T]; $E$ is the kinetic energy term [$L^3T^{-2}$]; and $C_K$ is the mixing efficiency coefficient for convection overturn [dimensionless].

The wind stirring contribution is calculated by the shear velocity ($u_*^2$) generated by the wind. The shear velocity (discussed in Equation (8), in 3.3.2 Wind) is a function of the wind strength and the drag coefficient. In the model, the density difference on the air and water surface is also accounted for. Applying the mixing efficiency coefficient for wind stirring, $C_W$, the available energy term related to wind stirring is shown in Equation (43).

$$E_{stirr} = 0.5\, C_K (C_W u_*^3) \Delta t \tag{43}$$

where $u_*$ is the shear velocity [$LT^{-1}$]; $E$ is the kinetic energy term [$L^3T^{-2}$]; $C_W$ is the mixing efficiency coefficient for wind stirring [dimensionless]; and $C_K$ is the mixing efficiency coefficient for convection overturn [dimensionless].

Together, Equations (42) and (43) compose the available kinetic energy term for convective and wind stirring dynamics, presented in Equation (44).

$$E_{TKE} = 0.5\, C_K(w_*^3 + C_W u_*^3)\Delta t \tag{44}$$

where $E$ is the kinetic energy term [$L^3T^{-2}$]; $w_*$ is the turbulent velocity scale [$LT^{-1}$]; $u_*$ is the shear velocity [$LT^{-1}$]; $C_W$ is the mixing efficiency coefficient for wind stirring [dimensionless]; and $C_K$ is the mixing efficiency coefficient for convection overturn [dimensionless].

As the first mixing analysis, Equation (44) is compared to the kinetic energy required for lifting and accelerating water particles placed at the bottom of the surface mixed-layer (i.e., on the top of the metalimnion). Lifting can be achieved as the potential energy set by the density differences is surpassed (Equation (*45*)). Whereas, the acceleration required energy (Equation (*46*)) depends on the velocities at place on the mixed-surface layer, represented by $w_*^3$ and $u_*^3$, and the mixing efficiency coefficients for wind stirring ($C_W$) and for the unsteady turbulence ($C_T$). Both terms can be summed to provide the required kinetic energy. (Equation (*47*))

$$E_{lifting} = \frac{\Delta\rho}{\rho_0} g z_{sml}\, \Delta z_{k-1} = g'_k z_{sml}\, \Delta z_{k-1} \tag{45}$$

$$E_{acceleration} = 0.5\, C_T(w_*^3 + C_W u_*^3)^{2/3}\Delta z_{k-1} \tag{46}$$

$$E_{PE} = \left(g'_k z_{sml} + 0.5\, C_T(w_*^3 + C_W u_*^3)^{2/3}\right)\Delta z_{k-1} \tag{47}$$

where $E$ is the kinetic energy term [$L^3T^{-2}$]; $\rho$ is the water density [$ML^{-3}$]; g is the gravity acceleration [$LT^{-2}$]; $g'_k$ is the reduced gravity acceleration between the mixed and the k-1 layer [$LT^{-2}$]; k is the layer number, starting from the bottom [dimensionless]; z is the depth [L]; $C_T$ is the mixing efficiency coefficient for the unsteady turbulence [dimensionless]; $w_*$

is the turbulent velocity scale [$LT^{-1}$]; $u_*$ is the shear velocity [$LT^{-1}$]; and $C_W$ is the mixing efficiency coefficient for wind stirring [dimensionless].

Thus, the GLM model will compared the energies, available and required, combining Equations (44) and (47), as Equation (48).

$$\underbrace{C_K(w_*^3 + C_W u_*^3)\Delta t}_{\substack{convective\ overturn \\ +\ wind\ stirring}} \geq \underbrace{\left(g'_k z_{sml} + C_T(w_*^3 + C_W u_*^3)^{2/3}\right)\Delta z_{k-1}}_{lifting+acceleration} \qquad (48)$$

If Equation (48) premise is met, the available energy is equal to or greater than the required energy, and the two adjacent layers (identified k and k-1) will undergo mixing. As mixing occurs, their volumes are summed and the characteristics, averaged out, weighted by the total mass of the layer. The surface mixed-layer depth is adjusted, as so its thickness, and the available energy used is removed from the system. Then, the model loop restarts the mixing process over the next layer, until Equation (48) conditions are not fulfilled anymore, or until the whole lake is mixed.

When Equation (*48* premise is not met, mixing will not occur and the calculated available energy, which has not been already used, is stored for the next time step, and the mixing algorithm will continue to assess the shear production and the Kevin-Helmholtz instabilities.

**(3) Shear Production and Kevin-Helmholtz Billowing**

Once the convective and stirring processes are computed, the GLM model calculates the mixing energy correspondent to shear stress production over the metalimnion and the occurrence of billows due to the Kevin-Helmholtz instability.

The shear energy production is modeled with the average velocity shear over a time period, and its accumulation due to continuous wind events. As wind stress is applied over a time interval, it increases the velocity shear value, highlighting the importance of continuous wind events for the production and maintenance of shear stress over the thermocline. However,

the model imposes a cut-off time ($\delta t_{shear}$), beyond which is assumed that no more shear-induced mixing will happen due to that event.

Acting over the metalimnion, the average velocity shear value is calculated by the Equation (49), proposed by Imberger and Patterson (1981), for applications on one-dimensional models (Hipsey *et al.*, 2019).

$$u_b = \begin{cases} \frac{u_*^2 \Delta t}{z_{sml}} + u_{b_{old}}, & t \leq t_b + \delta t_{shear} \\ 0, & t \geq t_b + \delta t_{shear} \end{cases} \quad (49)$$

where $u_b$ is the average velocity shear [LT$^{-1}$]; $u_*^2$ is the shear velocity [LT$^{-1}$]; $t$ is the time [T]; z is the depth [L]; $u_{b_{old}}$ is the average velocity shear accumulated from the previous time step [LT$^{-1}$]; $\delta t_{shear}$ is the cut-off time [T]; and $t_b$ is the initial moment of the wind event [T].

As a following step, the Kevin-Helmholtz instability is accounted by the model as an energy source and sink, once it consumes energy (billows formation) and produces turbulent energy (billows destruction). Its modeling parameters are the average velocity shear value ($u_b$), the reduced gravity between the epilimnion and hypolimnion, the mixing efficiency coefficient for KH turbulent billows ($C_{KH}$), and the KH length-scale (Equations (*50*)).

$$\delta_{KH} = \frac{C_{KH} u_b^2}{g'_{EH}} \quad (50)$$

where $\delta_{KH}$ is the KH length scale [L]; $C_{KH}$ is the mixing efficiency coefficient for KH turbulent billows [dimensionless]; $u_b$ is the average velocity shear [LT$^{-1}$]; and $g'_{EH}$ is the reduced gravity acceleration between the epilimnion and the hypolimnion [LT$^{-2}$].

At last, the available kinetic energy of the surface mixed-layer is updated, in order to account for the shear-production parcels (Equation (*51*). The total available energy is, then, compared, to the required energy for lifting and accelerating the metalimnion upper water.

Once again, if the conditions are met, the two adjacent layers will mix and their properties be redistributed, setting the conditions of the new layer.

$$\underbrace{\frac{C_K(w_*^3 + C_W u_*^3)\Delta t}{convective\ overturn\ +\ wind\ stirring}} + \underbrace{0.5C_S\left[\frac{u_*^2(\widetilde{z_{sml}} + \Delta\delta_{KH})}{6} + \frac{u_b\delta_{KH}\Delta u_b}{3}\right] + \left[g'_k\delta_{KH}\left(\frac{\delta_{KH}\Delta z_{k-1}}{24 z_{sml}} - \frac{\Delta\delta_{KH}}{12}\right)\right]}_{\substack{shear\ production+ \\ KH\ production\ and\ consumption}} \geq \underbrace{\left(g'_k z_{sml} + C_T(w_*^3 + C_W u_*^3)^{2/3}\right)\Delta z_{k-1}}_{lifting+acceleration} \quad (51)$$

After the mixing processes are accounted for, the thermocline stability is assessed. If the metalimnion layer thickness is such that the KH length scale surpasses it, the instability will take place. In this case, the model creates a six-layer structure to be placed around the thermocline, smoothing the density profile and preventing computational instabilities. Figure 10 summarize the discussed processes calculated for the surface mixed-layer, as computed by the GLM code.

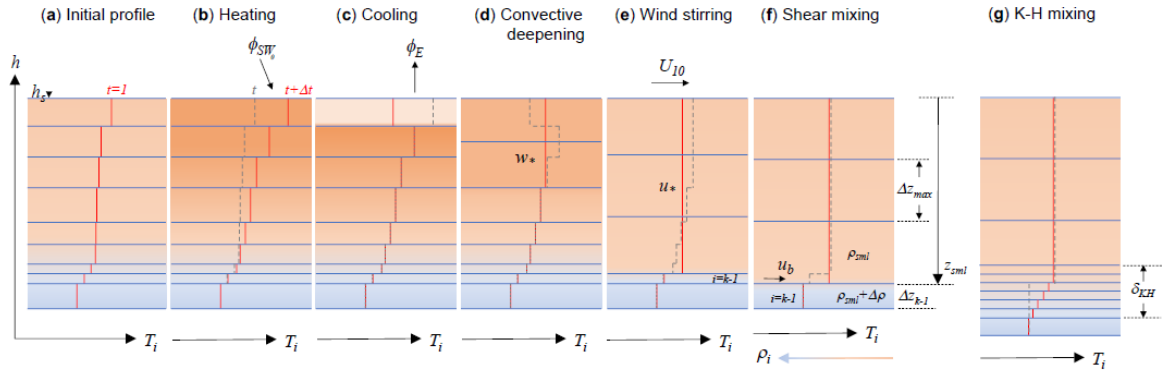


**Figure 10 - Schematic depiction of layer changes during stratification and mixing. Consecutive panels show changes from (a) the initial layer and thermal profile, to (b) heating due to solar radiation, to (c) evaporative cooling, which creates (d) convective mixing followed by (e) a wind event causing stirring and (f) shear mixing across the thermocline. If the metalimnion remains unstable to shear it may be subjected to mixing from K-H billowing, which opens up the thermocline as depicted in panel (g). Source: (Hipsey *et al.*, 2019).**

Bellow the thermocline, the prevailing mixing process modeled is the diffusive transport. The model, so called, "deep mixing" routine, proposes three alternatives for the hypolimnion mixing dynamic, to be chosen by the user: (1) no diffusivity; (2) constant diffusivity or (3) a derivation by Weinstock (1981), suitable for regions with weak or strong stratification, where

diffusivity increases with dissipation and decreases with heightened stratifications (Weinstock, 1981) (Hipsey *et al.*, 2019).

The diffusivity main parameter is the diffusivity coefficient ($E_z$). It is set to 0 for the first option; set to a constant valued equaled to the mixing efficiency coefficient for hypolimnetic turbulence ($C_{HYP}$), for the second option; or, for the third option, it is determined as a function of the stratification strength and the rate of turbulent dissipation (due to wind stirring and inflow intrusion)

In summary, the GLM model, with a one-dimensional approach, can perform the mass and energy balances of lentic environments, considering their main components and dynamics. The model routines are performed, separately, in a sub-daily (hourly) and daily time-steps. Within these routines, the surface mass and energy fluxes are compiled together, interacting and affecting one another. However, whilst the mass fluxes result in variations of the water level, energy fluxes will only affect the layers thickness, but never their heights. In its turn, deeper layers dynamics happen in response to surface heating or mixing processes, inflows or outflows discharges, and the diffusive transport in place. At the end of every time step, the model layer structure is assessed in the light of its stability and more layers are created, refining the column grid, if necessary.

Different parameters can be calibrated within the model. The maximum and minimum layer thickness ($dh$), as well as the maximum layer volume can be set by the user to ensure a good representation of the vertical profile and prevent calculation instabilities.

For the water balance, the main sources and sinks of water masses can be calibrated with the application of scaling factors ($f_{flow}$), inflow characteristics (drag coefficient ($C_{D\ inf}$), angle of slope ($\beta_{inf}$)), seepage coefficient, the runoff threshold, and, if applied, the outlet characteristics (i.e., weir discharge coefficient ($c_{D_{weir}}$), crest height and width)

For the energy balance, the main parameters are related to the heat and momentum fluxes on the surface layer (i.e., light extinction coefficient ($k_w$), sensible ($c_e$)and latent ($c_h$) heat transfer, wind drag coefficient ($c_d$)), also, the mixing efficiency coefficients ($C_K$, $C_W$, $C_S$, $C_T$, $C_{KH}$, $C_{HYP}$) and, for the bottom layer, the diffusivity coefficient ($E_z$).

Figure 11 presents a simplified version of the model main hydrodynamic code structure and Table 1 shows the main input data of the model.

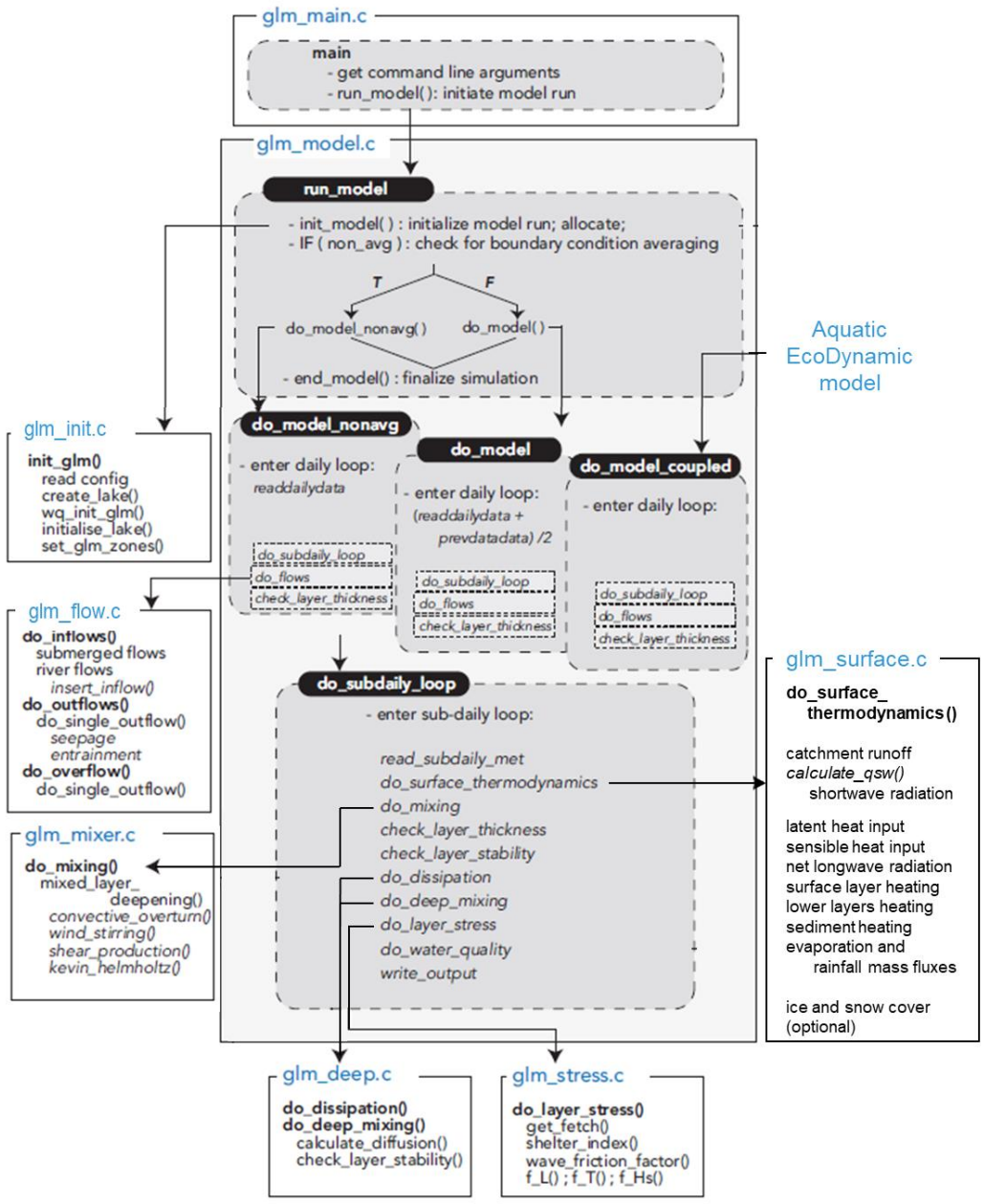


**Figure 11 - Overview of GLM code structure and program flow. Modules are depicted as a box with the main routines and functions summarized. Three entry points to the main model routines are possible: do_model uses the flow boundary condition data over the present and previous day in order to get the midday value, do_model_nonavg uses that from the present day only, and do_model coupled passes in the present-day flows from the host. Source: Adapted from (Hipsey *et al.*, 2019), to better demonstrate the surface thermodynamic routine)**

**Table 1 - The main input data and its characteristic (General Lake Model, v. 3.0.5). Source: Author.**

| Parameters | Time Interval | Components | Units | File Type |
|---|---|---|---|---|
| Inflows | Daily | Time; Flow; Temperature; Salinity | [day]; [m³/s]; [°C]; [mg/L] | inflow.csv |
| Outflows | Daily | Time; Flow | [day]; [m³/s] | outflow.csv |
| Rainfall | Hourly or daily | Rainfall depth | [m/day] | met.csv |
| Snowfall | Hourly or daily | Snowfall depth | [m/day] | met.csv |
| Shortwave Radiation | Hourly or daily | Radiation Intensity | [W/m²] | met.csv |
| Longwave Radiation | Hourly or daily | Radiation Intensity | [W/m²] | met.csv |
| Cloud Cover | Hourly or daily | Cloud cover fraction data | - | met.csv |
| Air Temperature | Hourly or daily | Average air temperature | [°C] | met.csv |
| Relative Humidity | Hourly or daily | Average relative humidity | [%] | met.csv |
| Wind Speed | Hourly or daily | Average wind speed 10 m above the water surface | [m/s] | met.csv |
| Hypsographic Curve | - | Height-Area Relationship | [m] x [m²] | .nml |
| Initial Profile | - | Depths; Temperatures; Salinity | [m]; [°C]; [mg/L] | .nml |

Other functions are available to better characterize the studied environment and frame the simulation. They may include: sediment heating (modeled as discussed in Equation (25)), bottom shear stress calculation, ice and snow dynamics, effects of wind-sheltering or still-air conditions over the surface fluxes, among others.

The GLM hydrodynamic model was, also, designed to operate with the Aquatic EcoDynamics Model (AED), simulating water quality and biological features.

Moreover, the user may customize the mass and energy balances, with some of the modeling alternatives already discussed, or activating and deactivating optional modules, providing what is important on their own simulation.

## 4.2 OTHER 1D MODELS

One-dimensional vertical models are widely used tools applied in the simulation of lakes and reservoirs, whose horizontal gradients are assumed to be homogeneous or of reduced importance. Most 1DV models are based on similar physical principles, well stablished around the scientific community, differing in terms of numerical solution and layer structure approaches, also, suitability and limitations.

The General Lake Model is one of the tools available for this type of study. However, many others may be considered. Understanding the mathematical model principles and applicability, as well as the environment to be modeled, is essential to better match the study requirements and the methodological approach. Here, some of the available 1DV models, most used in scientific studies, will be briefly discussed.

FLake is an open-source, bulk-thermodynamic model. Its main premise is the application of a self-similarity approach over the vertical thermal structure. The water column is divided into two layers: the upper layer working as a well-mixed reactor, with a vertically homogeneous temperature profile; and the bottom layer working as the thermocline, where the temperature gradient is parameterized using a polynomial self-similar representation, that is, the temperature profile characteristic shape is conserved among different lakes, irrespective of the depth of the layer. The FLake model uses a Lagrangian structure while it numerically solves the governing equations in each layer by integration over time. It also simulates ice, snow and sediment heating and can be coupled with other water quality models. An online version is also available. (Mironov, 2008) (Kirillin *et al.*, 2011) (Thiery *et al.*, 2014) (Le Moigne *et al.*, 2016) (Igb, 2021)

The MyLake is an open-source model, developed at the Norwegian Institute for Water Research (NIVA), written in Matlab programming language. It uses a Eulerian structure approach, applying the finite differences' method to solve discrete transport equations over each layer, as the user previously defines their placement and thickness. The model is focused

on a simple method, accounting only for the most significant driving forces and internal processes, to simulate, within a daily time step: the stratification and mixing events, ice and snow seasonal evolutions, sediment-water interactions, the phosphorus-phytoplankton dynamics, biogeochemical reaction and dissolved gases exchanges. (Saloranta and Andersen, 2004) (Saloranta and Andersen, 2007) (Woolway *et al.*, 2017)

Among the ecological models, the zero-dimensional PCLake has been successfully applied, as well as its one-dimensional extension the PCLake+, for assessing climate change impacts and lakes' trophic conditions. The first is an ecological process-based model focused on simulating the water quality and ecological interactions of shallow, mixed lakes, representing the whole lake as one homogeneous layer. Whereas, the PCLake+ extension is a mass-based model that adds a hypolimnetic layer to the lake, which can be configured by simple forcing functions and build-in empirical relationships or at a user specified-depth. Each layer receives their own state variables (i.e., nutrients and oxygen) and perform mass balances within itself. Yet, during mixing events, the model will resemble the original PCLake structure and diffusive processes will be accounted for between the layers. The PCLake+ is an open-source model coded as a Eulerian structure, where differential equations will be solved, at each layer, over a daily period. Moreover, with a strong focus on ecology, the one-dimensional model is an alternative for some hydrodynamically based models and their inherently bias, or a complement to them, once it can be coupled with some of these models. (Mooij *et al.*, 2007) (Janssen, Teurlincx, *et al.*, 2019)

Other 1D models worth to be cited are the DYRESM (Imberger and Patterson, 1981; Hamilton and Schladow, 1997), SIMSTRAT (Goudsmit *et al.*, 2002; Perroud and Goyette, 2010), Dynamic Lake Model with Water Quality (DLM-WQ) (Sahoo *et al.*, 2013) and AQUASIM (Reichert, 1994).

# 5 CASE STUDY

In this work, the Hedberg reservoir (São Paulo, Brazil) was selected as the case study. This chapter presents the studied site overview and the description of the used materials. Here, the materials are the data collected by the local monitoring system, for the period of 2017 to 2020. The dataset is composed by observed meteorological variables, the estimation of inflows and outflows and on-site measurements of water temperature and transparency.

In this context, this chapter aims to partially address the second specific objective of this study, in regard to the compilation, analysis and organization of the observed data.

## 5.1 STUDIED SITE

Located in the state of São Paulo - Brazil, the Hedberg reservoir (23°25'39"S and 47°35'39"W) was built in 1811 to provide water for Brazil's first steelmaker and small villages nearby. Currently, with its surrounding area defined as preserved site by the Brazilian government, named as Floresta Nacional de Ipanema, its main uses are flow regulation, water supply, scientific studies, landscape and recreation. (Icmbio, 2017) (*Figure 12*)

Downstream of the Ipanema River, the dam resulted in a 0.23 km²-surface area-reservoir, enclosing a catchment area of 234 km². Its basin is characterized by different land uses, with 68.2% of its area classified as rural (agriculture and pasture), 21.5% as forests and natural vegetation and 9.8% as urban. Yet, the growth of the urban sprawl in recent years reflects the anthropogenic influence that the basin has suffered. (Mapbiomas, 2020) (*Figure 13*)

**Figure 12 - Hedberg Reservoir. Source: Author (2019)**

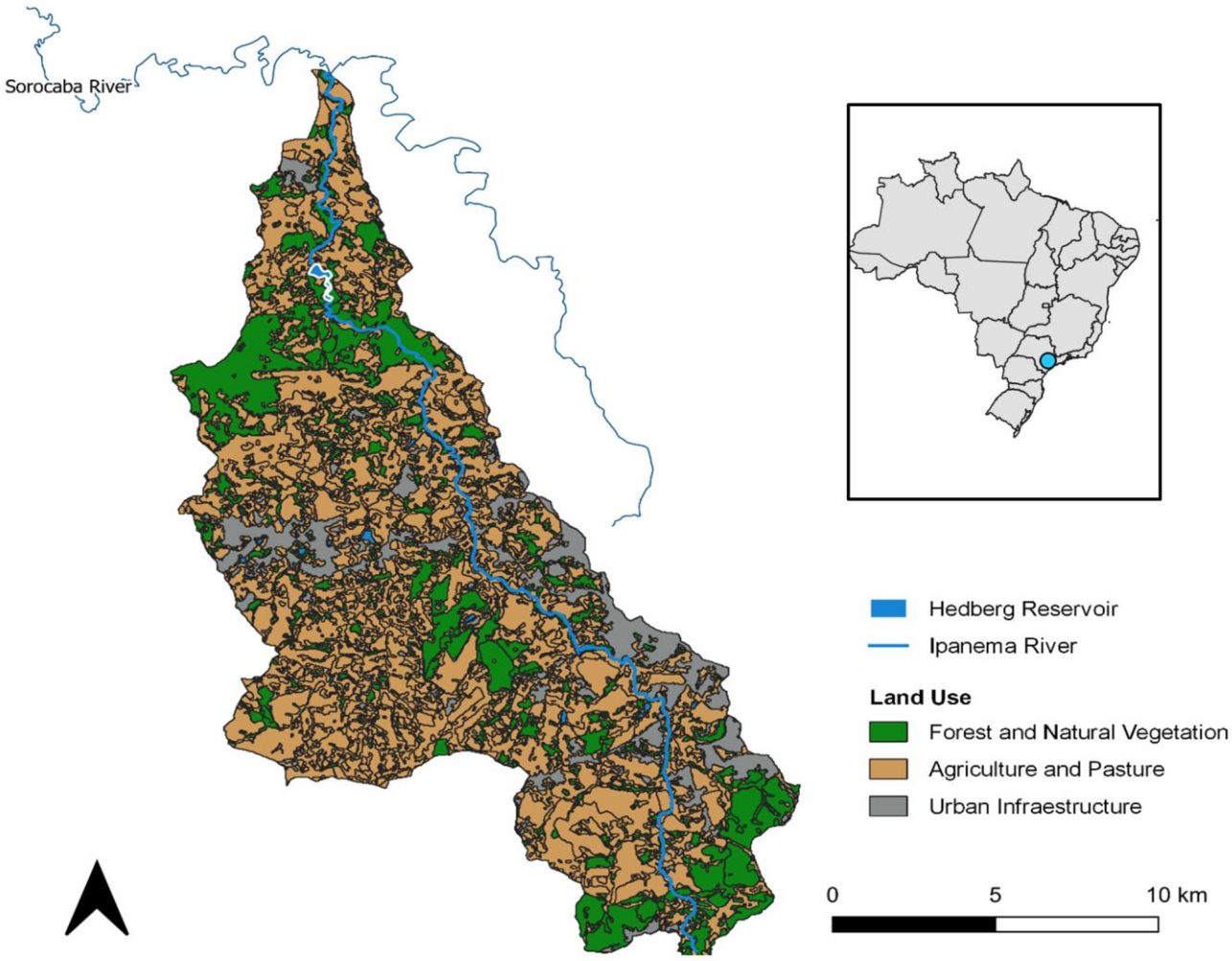


**Figure 13 - Ipanema Basin: Land Uses (Mapbiomas, 2020)**

The Hedberg reservoir has an approximately volume of 1.5 hm³, with its hypsometric curve presented in Figure 14. An average flow from 2 to 5 m³/s, determines a detention period of 2 to 10 days. Its maximum depth is 5 m and the mean depth 4.5 m. The spillway crest elevation is 548.0 m, and the basin width and length at crest elevation are 670 m and 630 m, respectively.

With several events of mixing and stratification along the year, the lake presents a polymictic behavior. Furthermore, concerning its water quality evaluations, the lake is considered eutrophic (Icmbio, 2017). However, the excess of nutrients has been pointed out as a problem, mainly the phosphorus load (Amorim, 2020).

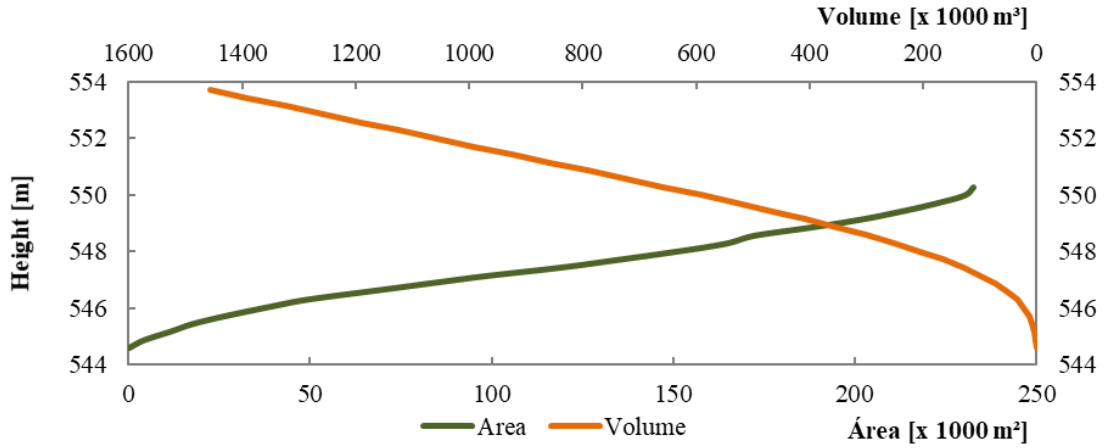


**Figure 14 - Hypsographic Curve (Hedberg Reservoir) (Fcth, 2015)**

## 5.2 MATERIALS

### 5.2.1 Meteorological Data

The Ipanema basin, situated in the tropical zone (23.42° S and 47.6° W), has a temperature range between 15 and 35°C, predominant wind direction as Southeast (SE) and annual precipitation rate of, approximately, 1500 mm. The meteorological data, regarding the reservoir, was treated in order to provide an accurate dataset, as input data, to the model.

The meteorological data was obtained from two different stations. The first one is located on the banks of the reservoir (*Figure 15*), near the spillway, collecting data on: solar radiation, air temperature, relative humidity, wind speed and direction (10 meters above the lake' surface),

atmospheric pressure and precipitation. The variables are measured at a10 minutes time step, except by the wind speed and direction that have a 1-minute interval.

This station was installed and its currently maintained by the Fundação Centro Tecnológico de Hidráulica (FCTH). Its monitoring data are available from 2016 until now (2022), however, due to maintenance problems, some gaps and inconsistences can be found in the dataset and, therefore, had to be complemented.

The second meteorological station is controlled by the Instituto Nacional de Meteorologia (INMET). Located about 1 km from the lake (Code: A7113 – Sorocaba), its monitoring data is available since 1989, in hourly time-steps. (Inmet, (2017 - 2018))

**Figure 15 - Meteorological Station on the bank of the Hedberg Reservoir. Source: Author.**

In order to compose a complete meteorological dataset, for the years 2017 to 2020, the gaps and inconsistences observed in the data collected by the local meteorological station were supplemented with information from the second one and, if needed, other sources. The period

between July and September, 2019 was not considered in this study, due to lack of monitored data for all analyzed atmospheric variables.

The solar radiation data measured on site presented several flaws, and, therefore the INMET station was chosen as its main source. Some failures on June, 2018 (days 02 until 06), were complemented with theorical values (Varejão-Silva, 2000).

Air temperature and relative humidity local measures were used between January and June, 2017. However, a problem with the monitoring equipment prevented the measures of these variables until 2020. The data was complemented with the second station, until December, 2020.

The correlation coefficients between the two stations for each variable were 0.81 (air temperature) and 0.82 (relative humidity), indicating a strong correlation according to literature. (Cohen, 2013)

Wind speed and direction measurements presented the longest monitoring period on the local station, with valid data from January, 2017 to September, 2018, and from May to December, 2020. Periods with lacking data were complemented by the INMET measurements. The correlation coefficient for windspeed is 0.52, which does not indicate a strong correlation. However, as the only available source, the INMET data was used.

Precipitation data, which in this study case is restricted to rain, was collected by the local station from January to November, 2017. From December,2017, and on, the INMET station was used. However, to fulfill the failure on February, 2018 (days 02 to 28), approximated hourly data was calculated from the daily data used on the SMAP software.

The complete meteorological dataset compiled for studied period (2017-2020) is shown in Figure 16. Data from July to September 2019 were not complemented due to inconsistencies on both monitoring station during the period.

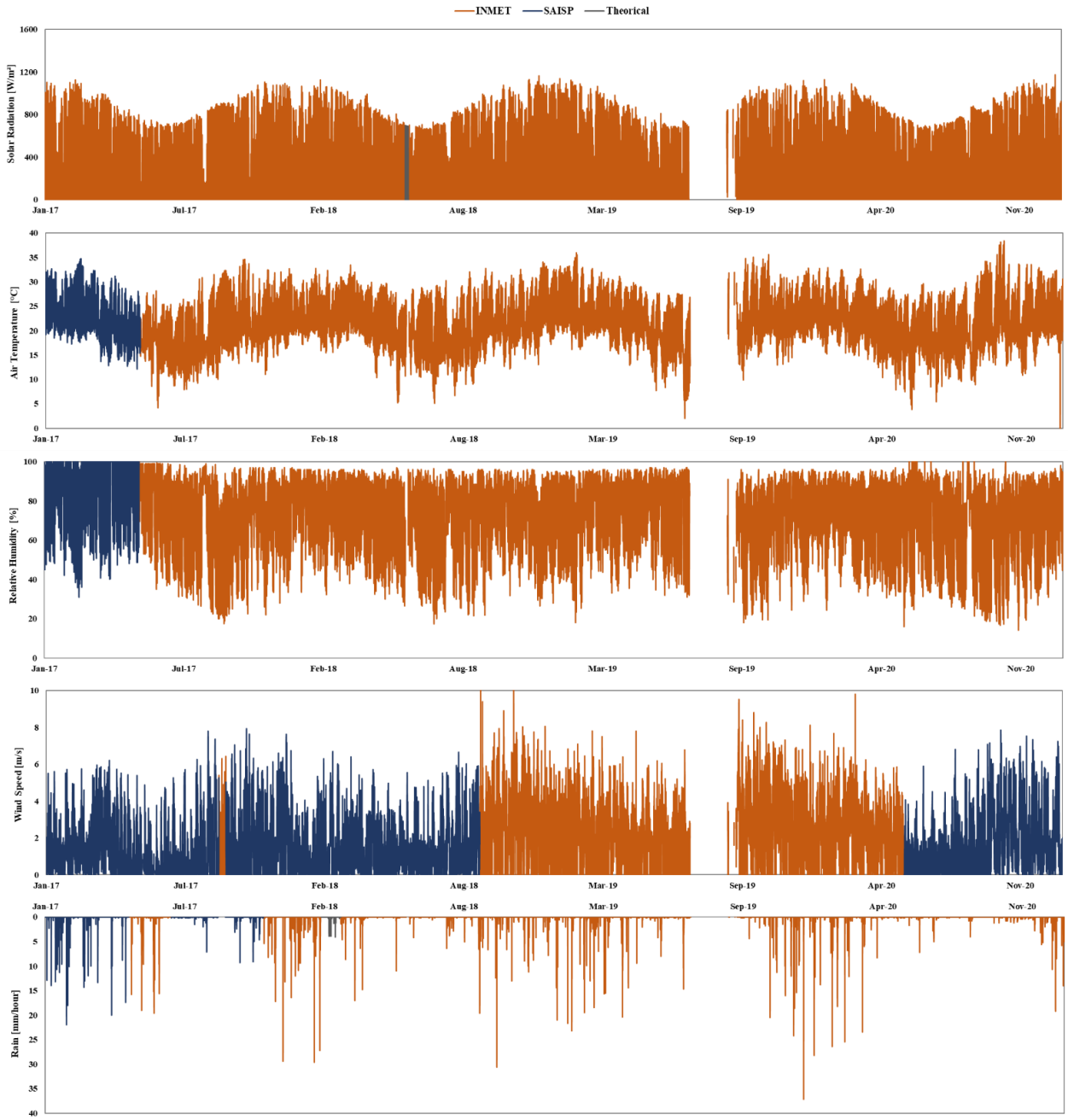


**Figure 16 - Meteorological dataset (2017 and 2020): Blue: Local Station (SAISP), Orange: INMET Station and Gray: Theorical Values. Source: Author.**

### 5.2.2 Hydrological Data

The hydrological data upstream of the Hedberg Reservoir was calculated through the application of the Soil Moisture Accounting Procedure (SMAP), a deterministic hydrological model of rain-flow transformation. Designed by Lopes, Braga Jr and Conejo (1982), the model requires potential evaporation and precipitation data to determine the base flow and the runoff over the catchment area.

The model is based on a three-reservoir system, which represents the main water fluxes to be brought about after a precipitation (rain) event: superficial (river flow and runoff), infiltration (soil) and groundwater flow (Figure 17). Accounting for the rainfall and potential evapotranspiration rates, as so for soil characteristics of the catchment area, the SMAP model generates the basin base and superficial flow, which can be calibrated in comparison to historical flow series, in a daily time step.

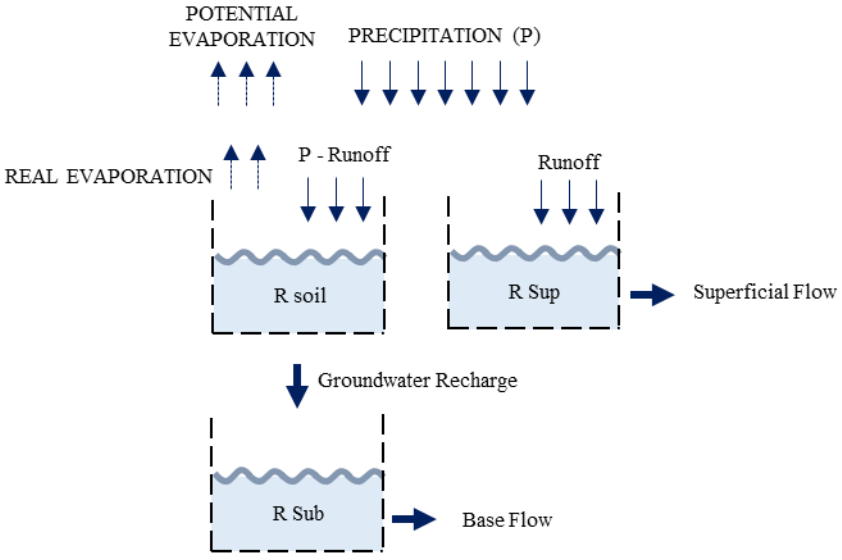


**Figure 17 - SMAP three-reservoir system (daily model). Source: Adapted from: Lopes; Braga Jr.; Conejo (1982).**

The model has eight calibration parameters. They represent the catchment soil characteristics (Sat, Crec, Capc), the basin initial conditions (Ai, tuin and ebin) and the runoff (K2t) and base flow (Kkt) recession (Lopes *et al.*, 1982). Recent studies discuss the SMAP calibration method and application in Brazilian watersheds (Cavalcante *et al.*, 2020; Maciel *et al.*, 2020) .

For this study, daily evaporation data was obtained by the INMET station and the precipitation data was composed by Thiessen polygon method with five different meteorological stations – in order to cover most of the watershed, even at great distance from the reservoir, and fill in gaps of missing data. Two of the stations were the ones previously cited on this study, the local station (maintained by FCTH) and the INMET station in Sorocaba (SP). The other three stations used were localized in the nearby cities of Votorantim (SP), Salto (SP), Araçoiaba da Serra (SP).

For the Ipanema basin, the calibration and validation of the SMAP model were performed from April, 2016 to April, 2017. The model performance was assessed through the relative error calculated for the mean and standard deviation values of the observed and simulated flow series.

With the mean relative error of near 0%, the model was considered calibrated. The adjusted parameters, the performance results and the comparison between both series are shown in Table 2, Table 3 and Figure 18, respectively.

These results provided the basin inflow for the Hedberg reservoir (*Figure 19*).

**Table 2 - SMAP model: Calibrated Parameters (Hedberg Reservoir). Source: Author.**

| Parameters | | Limits |
|---|---|---|
| sat | 100 | 100<2000 |
| k2t | 1.5 | 0,2<10 |
| crec | 13 | 0<20 |
| ai | 2 | 2<5 |
| capc | 20 | 30<50 |
| kkt | 48 | 30<180 |
| tuin | 70 | |
| ebin | 5 | |

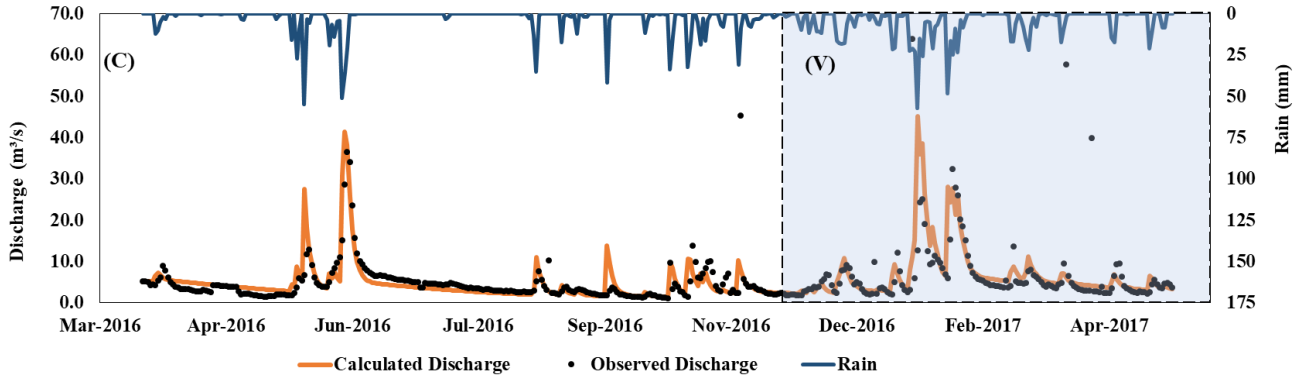


**Figure 18 - Calibration and validation of the SMAP hydrological model (2016 - 2017). Source: Author.**

**Table 3 – Results of the calibration and validation of the SMAP hydrological model. Source: Author.**

| | Calculated Discharge [m³/s] | Observed Discharge [m³/s] | Relative Error [%] | RMSE [m³/s] | MAE [m³/s] | NSE [-] |
|---|---|---|---|---|---|---|
| **Mean** | 5.57 | 5.58 | -0.10% | 5.61 | 2.16 | 0.28 |
| **Standard Deviation** | 5.75 | 6.59 | -12.76% | - | - | - |

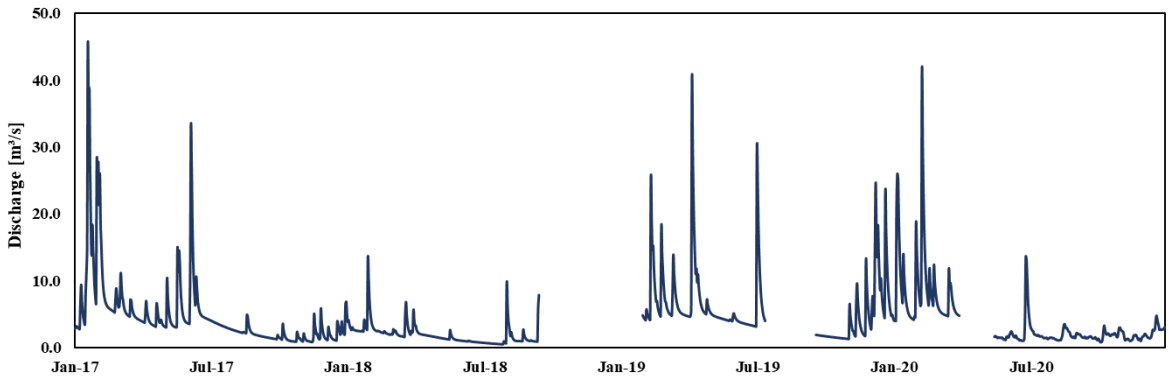


**Figure 19 –Inflow data at the Hedberg Reservoir computed by SMAP Model (2017-2020). Source: Author.**

### 5.2.3 Monitoring Data

The monitoring system implemented on the studied site is composed by the local meteorological station, a water level sensor and two floats placed on the lake, each with a set of thermistors attached to a rope and a plummet.

Installed on the bank of the reservoir, the water level sensor provides the surface height, based for the outflow estimation, within a 10-minutes time step. Regarding the period of interest, the monitoring data was gathered from January, 2017, to September, 2018 (Figure 20). Recent maintenance (May, 2020) has restarted the local monitoring.

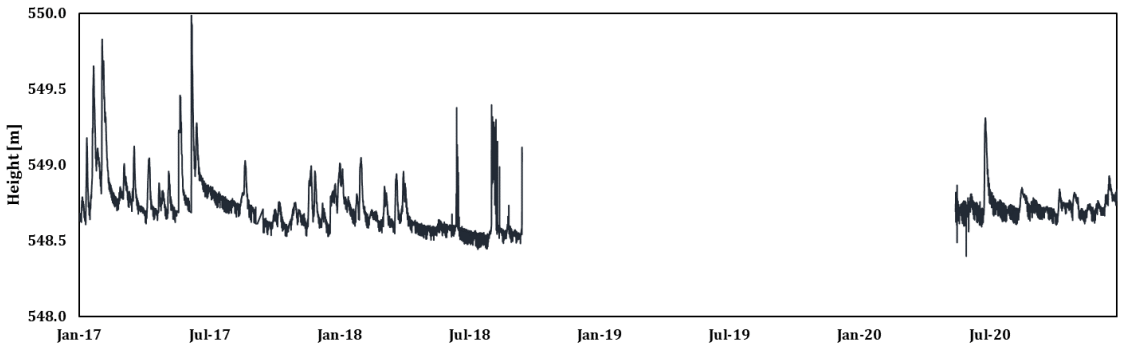


**Figure 20 – Water level monitored data (2017 – 2018) – Hedberg Reservoir. Source: Author.**

The observed outflow data was obtained through the discharged curve of the spillway (Figure 21). The curve was built considering the geometry of the hydraulic structure and the height of the water surface.

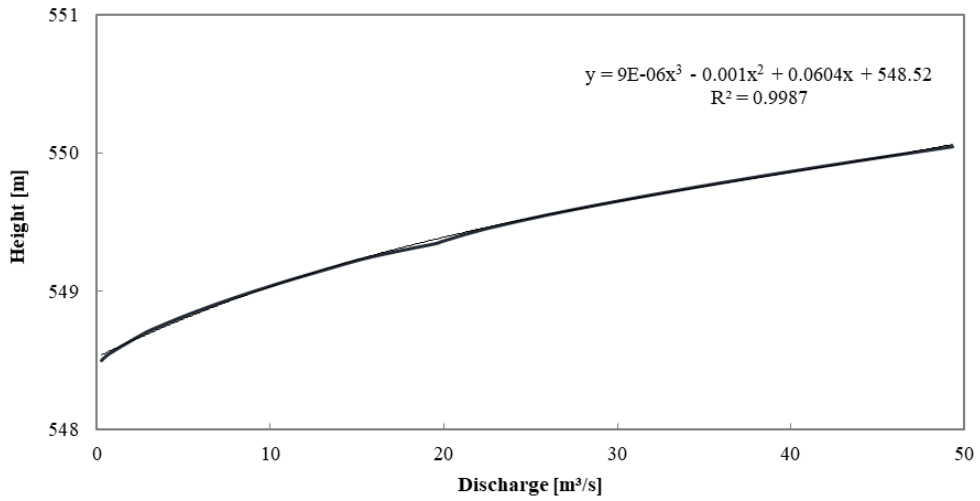


**Figure 21 – Discharge Curve – Hedberg Reservoir Spillway. Source: FCTH (2015).**

On the lake, two floats, with a set of thermistors on each one, monitors water temperature data for two distinct vertical profiles. Each float has a plummet and a rope attached to it, where the probes are displayed. (*Figure 22 and Figure 23*)

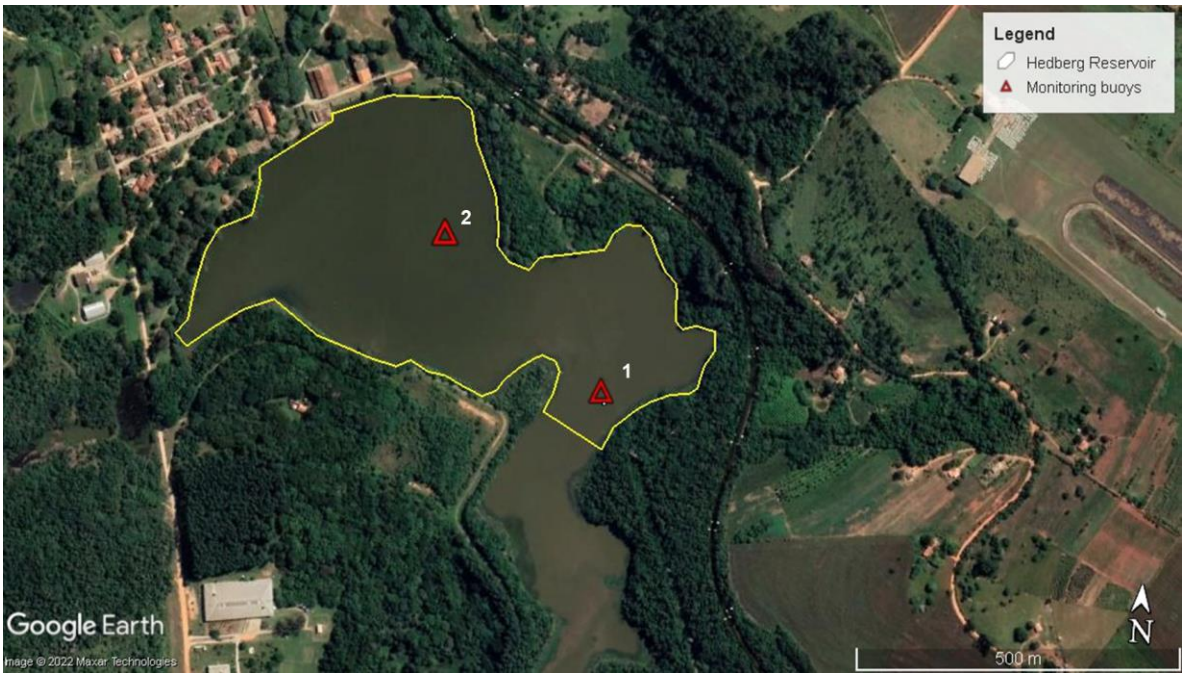


**Figure 22 - Monitoring floats displayed on the Hedberg Reservoir Source: Google Earth. (Access: June, 2022)**

The first float is positioned at the entrance of the Ipanema River on the reservoir. It has one thermistor attached to it, in order to measure the inflow temperature. Its data ranges from January, 2016, until now (2022), with some gaps during this period.

The second float is located at the center of the lake, where the depth is maximum (around 4.5 m along the year). With four probes placed at different depths along the vertical profile (from the surface: 0.5 m, 1.5 m, 2.5 m and 3.5 m), the float establishes itself as a representative point of the reservoir, allowing for the analysis of the occurrence of hydrodynamic processes. Its dataset, also, range from January, 2016, until now (2020), with some periods lacking data.

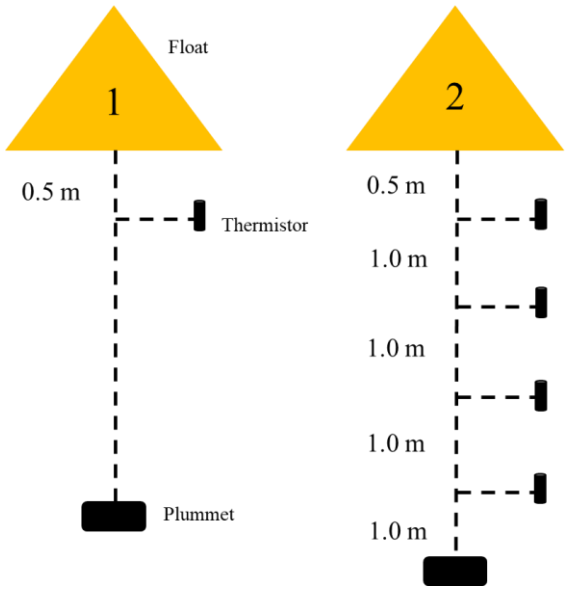


**Figure 23 – Scheme of the two monitoring floats and their equipment. Source: Author.**

On both floats, the thermistors used are the HOBO Water Temp Pro v2 Onset Logger (*Figure 24*), programmed to monitor data within a 2-minutes time-step, and an accuracy of ± 0.2°C.


**Figure 24 - Thermistor used on floats 1 and 2. HOBO Water Temp Pro v2 Onset Logger. Source: Onset Computer. (Access: June, 2020)**

The water temperature monitored on the first float represents the inflow temperature of Rio Ipanema. During the years 2017 to 2020, periods without monitoring data were complemented by the daily mean air temperature measured on site (Correlation coefficient of 0.65). (*Figure 25*) (Read *et al.*, 2014)

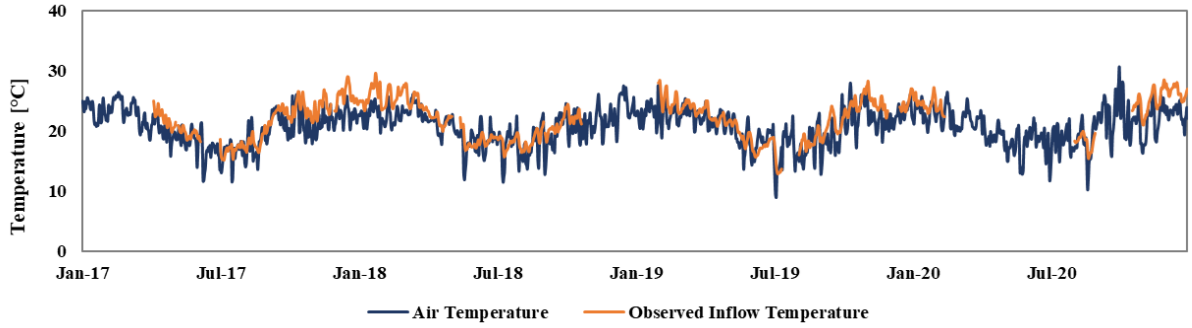


**Figure 25 - Air temperature and Observed Inflow Temperature (2017 to 2020) - Hedberg Reservoir. Source: Author.**

The dataset of the second float, for 2017 to 2018, has monitoring data from April, 2017, until October, 2018, lacking information on June (2017) and some days of May (2018). The third sensor (2.5 m), however, lacks data from July until September (2017), and the bottom sensor (3.5 m) from September (2017) until January (2018). (*Figure 26*)

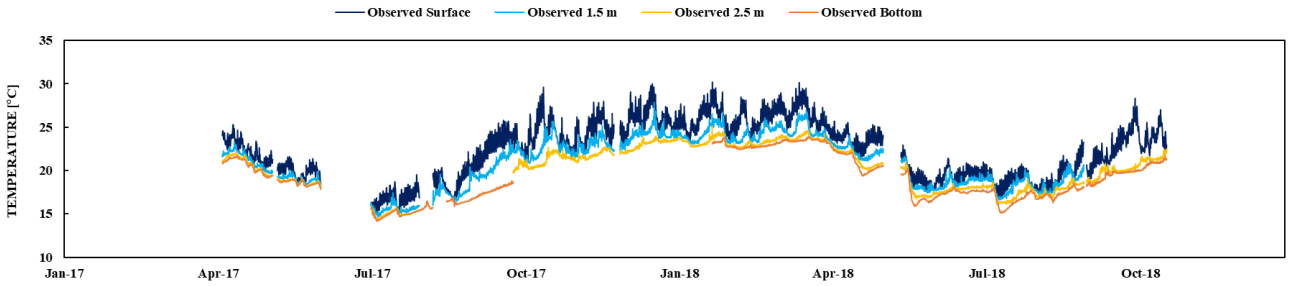


**Figure 26 - Temperature monitored on the second float at four different depths (0.5 m - surface, 1.5 m, 2.5 m and 3.5 m - bottom) – 2017 and 2018. Source: Author.**

Due to the SARS-Cov-2 Coronavirus pandemic, the maintenance of the monitoring data equipment had to be paralyzed along the year 2020, therefore, few data could be collected during this period.

Hence, for 2019 to 2020, monitoring data was gathered from February, 2019, until February, 2020, with incomplete data on July (2019), December (2019) and some February (2020). The monitoring was restarted in August, 2020 and data from October to December, 2020 was obtained. (*Figure 27)*

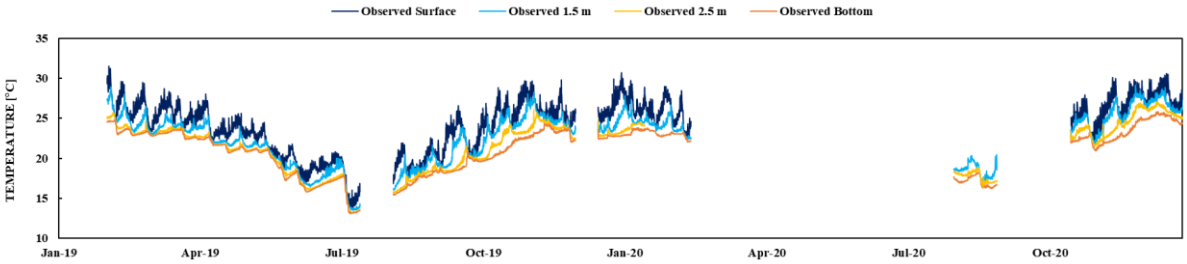


**Figure 27 - Temperature monitored on the second float at four different depths (0.5 m - surface, 1.5 m, 2.5 m and 3.5 m - bottom) – 2019 and 2020. Source: Author.**

The maintenance of this monitoring system requires local monthly visits to evaluate the equipment and gather the monitored data. These visits are held by a team of researchers that develop studies on the site.

The process includes a boat ride to reach the floats, cleaning of the equipment (that usually collect algae near the surface thermistor, the rope and bottom of the float), the download of the data monitored from the sensors, the measure of the Secchi depth on site and sampling of water for water quality analysis. (*Figure 28* and *Figure 29*)

**Figure 28 - Maintenance of the monitoring equipment (2019). Source: Author.**

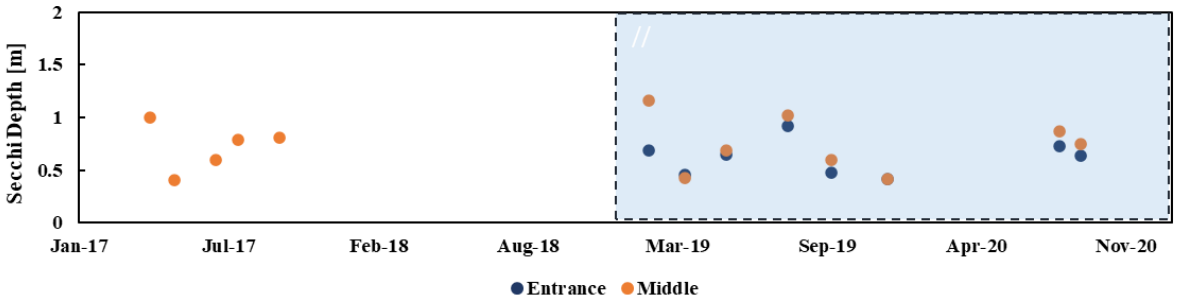


**Figure 29 - Secchi depth measurements (2017 - 2020). The years 2019 and 2020 are highlighted in blue. Source: Author.**

The periods with available data from the monitoring system, for the years 2017 to 2020, are shown in Table 4.

**Table 4 - Monitored data (2017 – 2020) - Hedberg Reservoir. Source: Author.**

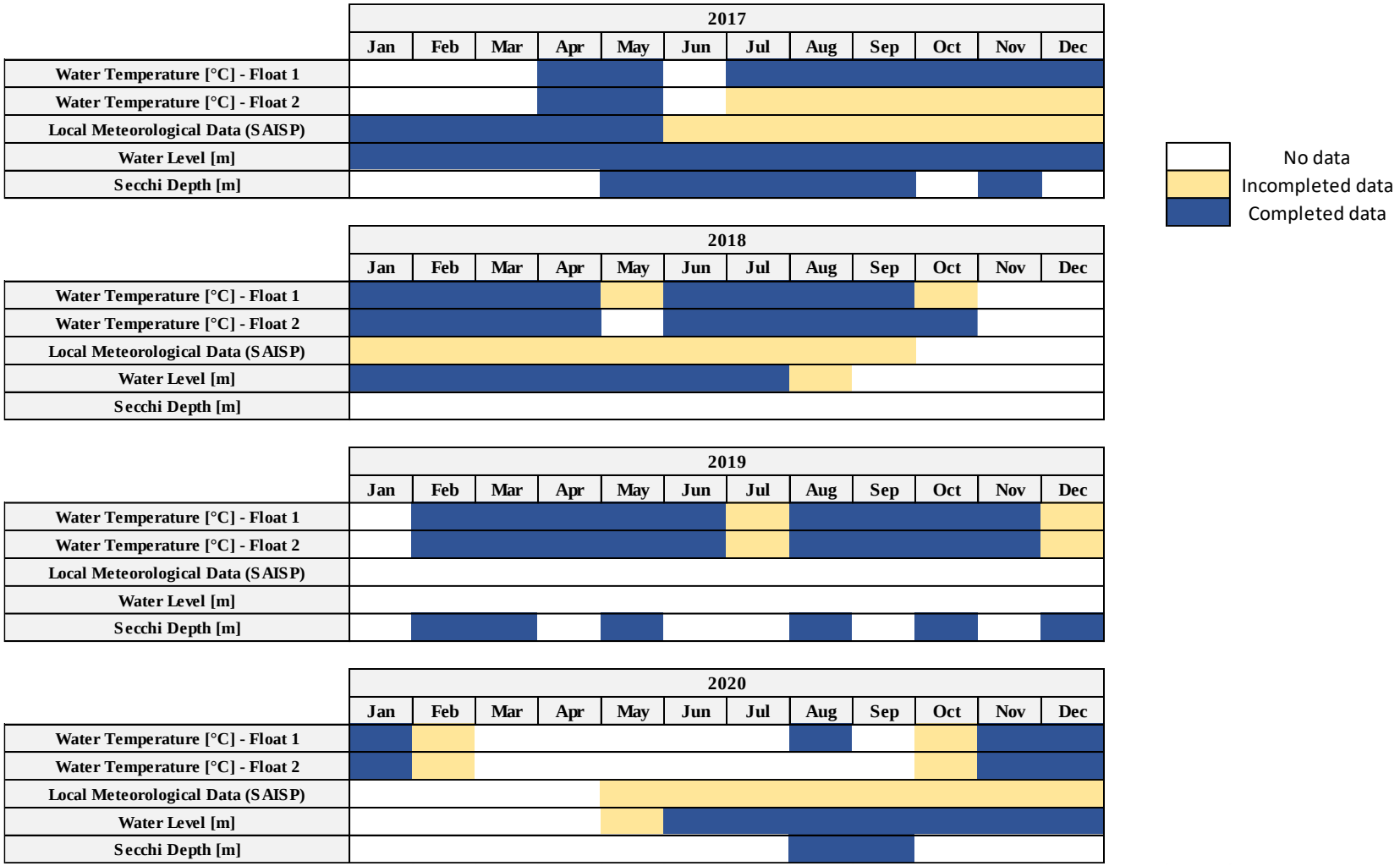

# 6 DATA PREPARATION

This chapter focuses on the data preparation required to simulate two climate change scenarios, an optimistic and a pessimistic one. The climate change scenarios were developed by global climate models, based on prediction of greenhouse gas emissions. In order to use climate change scenarios as input in the GLM, the data had to be transformed to better fit the model's requirements. The inflow characteristics were estimated, based on the predicted rain and air temperature, and the atmospheric variables were discretized into hourly values.

In this context, this chapter aims to partially address the second specific objective of this study, in regard to the compilation, analysis and organization of the projected data.

## 6.1 CLIMATE CHANGE SCENARIOS

In the Fifth Assessment Report (AR5), published in the 2014's Intergovernmental Panel on Climate Change (IPCC) report, four climate change scenarios were defined, regarding projections on anthropogenic influence on the global climate pattern. The scenarios were developed using Integrated Assessment Models (IAMs), as input to several climate change model simulations, and assessing the consequences projected on climate systems (Ipcc, 2014).

The Representative Concentration Pathways (RCPs), as they were named, represent four different pathways concerning greenhouse gas emissions, air pollutant and land use. They vary from a restricted mitigation scenario (RCP 2.6), two intermediate scenarios (RCP 4.5 and 6.0) to a pessimistic one (RCP 8.5) (Ipcc, 2014). (*Figure 30*)

According to the IPCC, "baseline" scenarios, which do not propose any additional mitigation measure, usually result in pathways between the RCP 6.0 and RCP 8.5 (Ipcc, 2014).

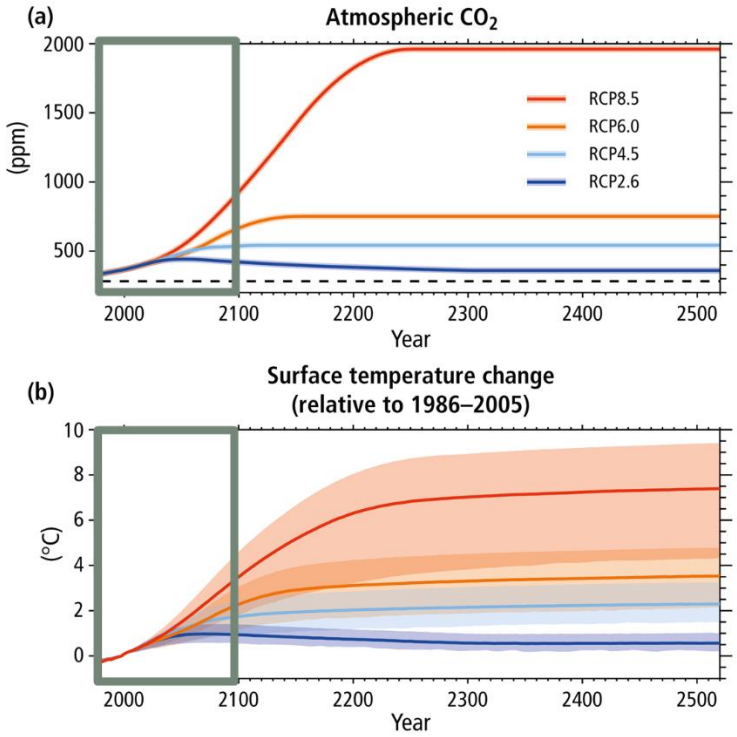


**Figure 30 - Climate change projections: (a) Atmospheric CO2; (b) Surface temperature change (2000 to 2100 accentuated).Source: (Ipcc, 2014).**

The PROJETA is a Brazilian government research platform by the Instituto Nacional de Pesquisas Espaciais (INPE) that works as a data repository for the Centro de Ciência do Sistema Terrestre (CCST/INPE). The platform is responsible for assessing the climate change projections for South America and providing access to its data.

For this study, two climate change scenarios were obtained from the PROJETA platform and applied to the hydrodynamic model: RCP 4.5, representing the optimistic scenario, and the RCP 8.5, indicating the pessimistic one. (Table 5)

For the South America, Central America and Caribe, the scenarios RCP 4.5 and RCP 8.5 were generated with the regional climate model Eta (Mesinger *et al.*, 2012), with a 20 km spatial resolution. The downscaling was forced by two global climate models HadGEM2-ES (Collins *et al.*, 2011) and MIROC5 (Watanabe *et al.*, 2011)).

**Table 5 - RCPs scenarios defined: CO2 equivalent emissions and global mean temperature change projected by 2100. Source: Author.**

| Climate Change Scenarios | $CO_2$ eq. Emissions (ppm) | Global Mean Temperature Change by 2100 (°C) |
|---|---|---|
| **RCP 4.5** | 650 | 1.8 |
| **RCP 8.5** | 1000 | 3.6 |

The projected meteorological data is provided in daily measures for the variables: solar radiation (short and longwave), evaporation, precipitation (rain), relative humidity, air temperature, wind speed and direction, for the period ranging from 2006 to 2099.

However, the data is projected accounting for months with 30 days, with the exception of February. Therefore, the months with 31 days received averaged values from the days $30^{th}$ and $01^{st}$.

In this study, both climate change scenarios were simulated between the years 2021 and 2099. To help the analysis, the simulated period was divided into three sets, near future (2021 – 2040) (*Figure 31*), middle-term future (2041 – 2070) (*Figure 32*) and distant future (2071 – 2099) (*Figure 33*).

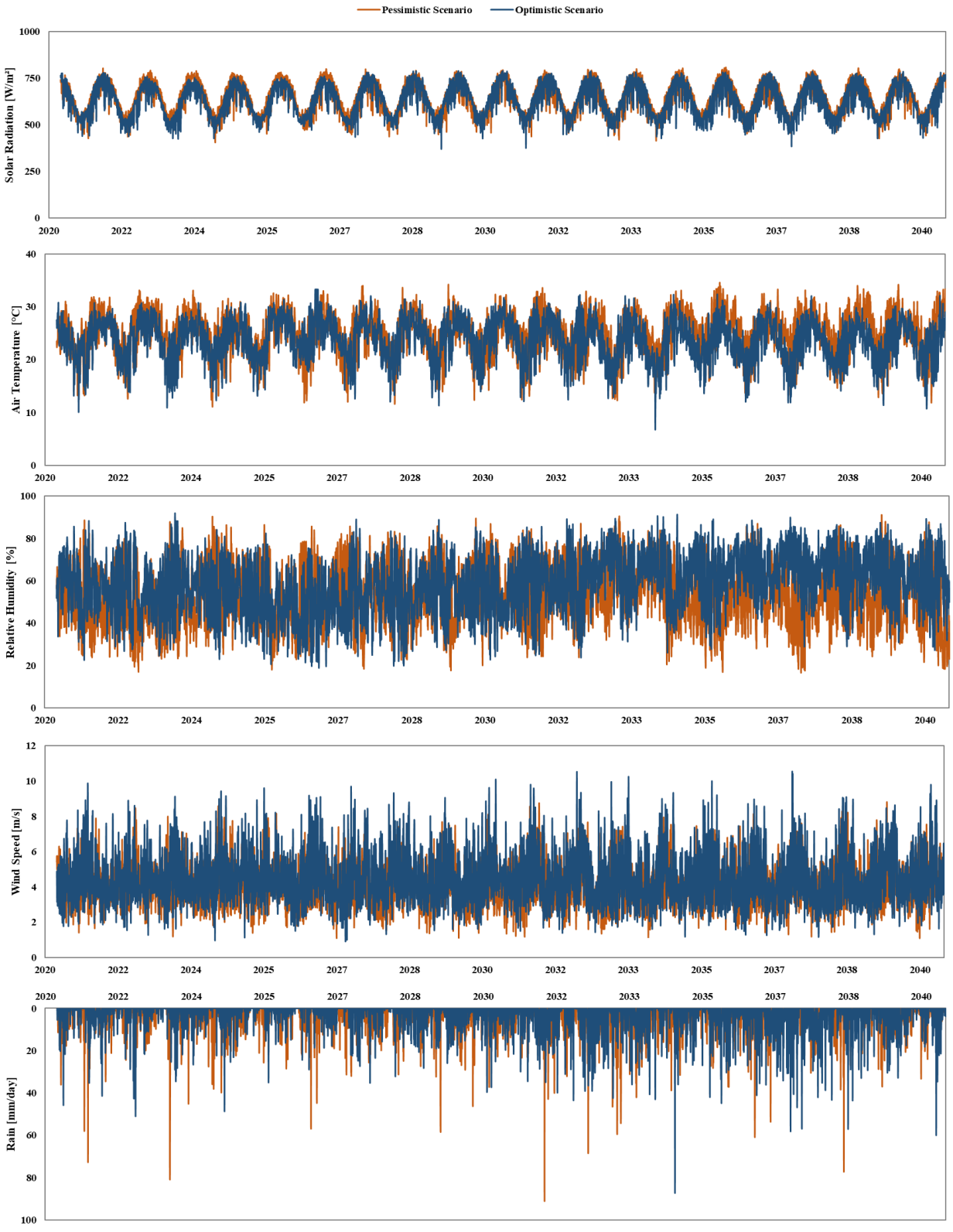


**Figure 31 - Optimistic and Pessimistic Scenario: Near future (2021 – 2040). Source: Author.**

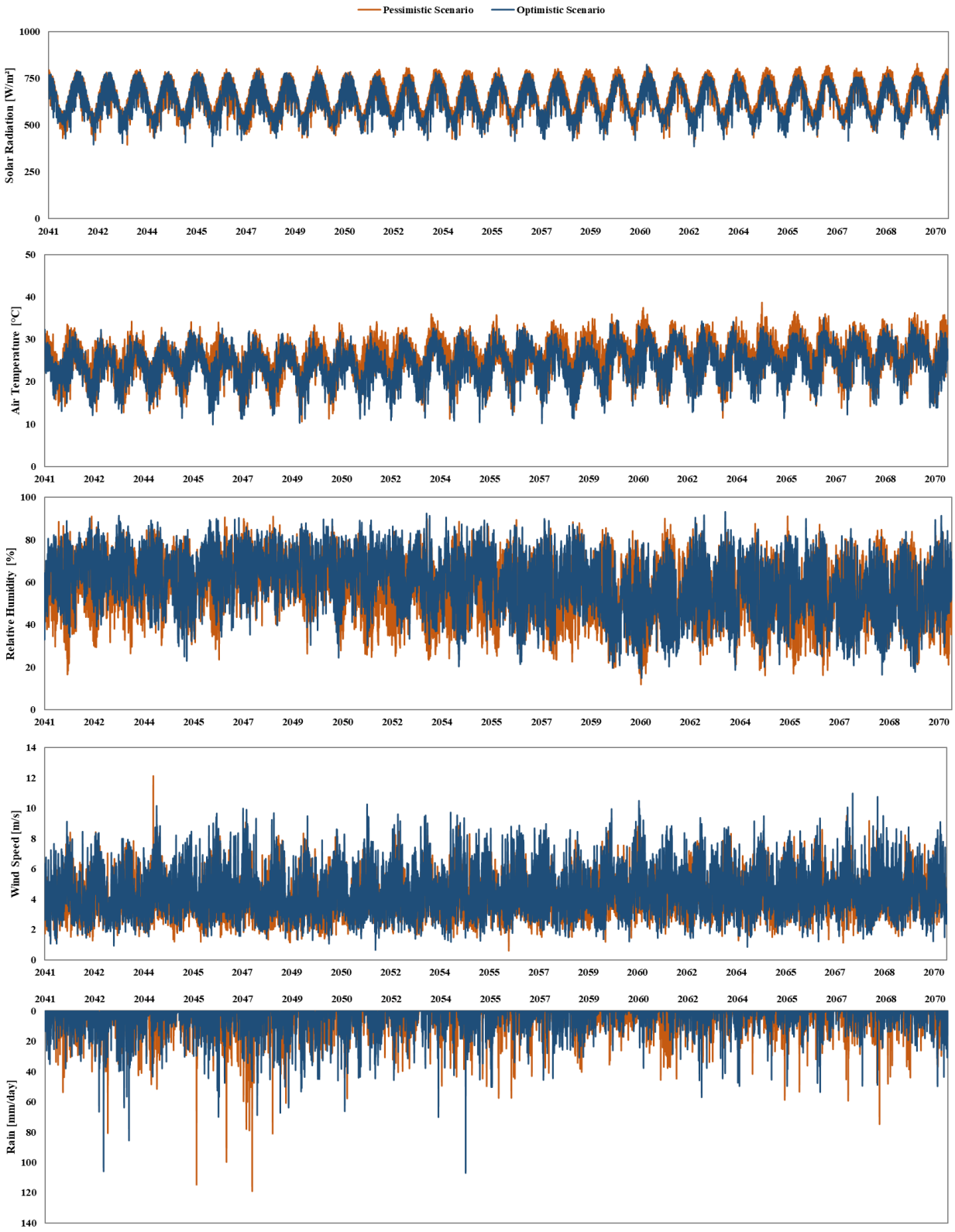


**Figure 32 - Optimistic and Pessimistic Scenario: Middle-term future (2041 – 2070). Source: Author.**

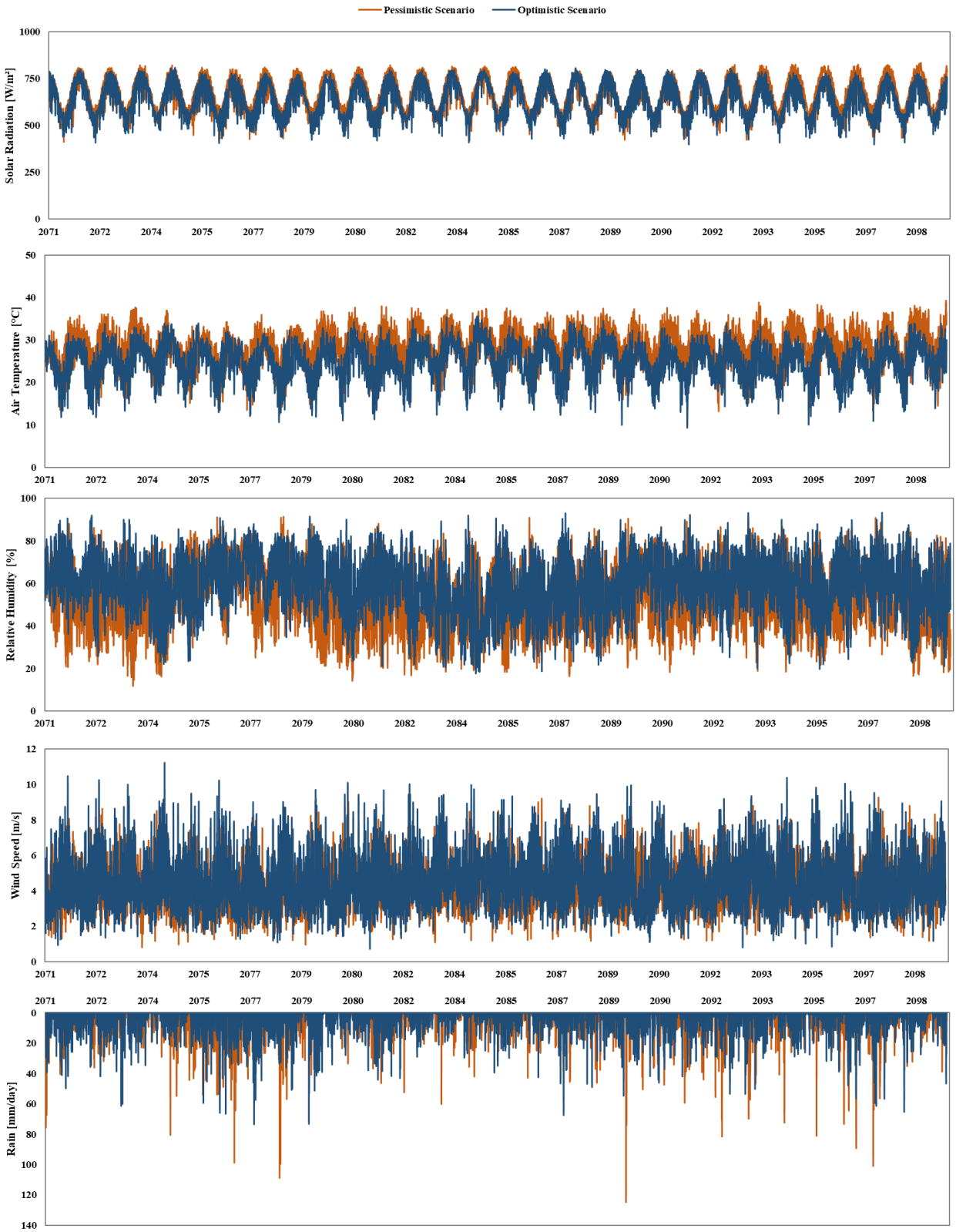


**Figure 33 - Optimistic and Pessimistic Scenario: Distant Future (2071 – 2099). Source: Author.**

## 6.2 INFLOW DATA PREPARATION

The inflow data required by the GLM is composed by the variables: flow, temperature and salinity. The data is provided on average daily values.

The climate change flow values were obtained with the rain-flow model SMAP (Lopes *et al.*, 1982), which had been calibrated and validated for the studied site. The SMAP input data was the projected evaporation and rain information.

In this study, neither the projected precipitation (rain) nor evaporation data were corrected regarding their bias in relation to the observed data.

Figure 34 and Figure 35 display the projected data for the optimistic and pessimistic scenarios, respectively.

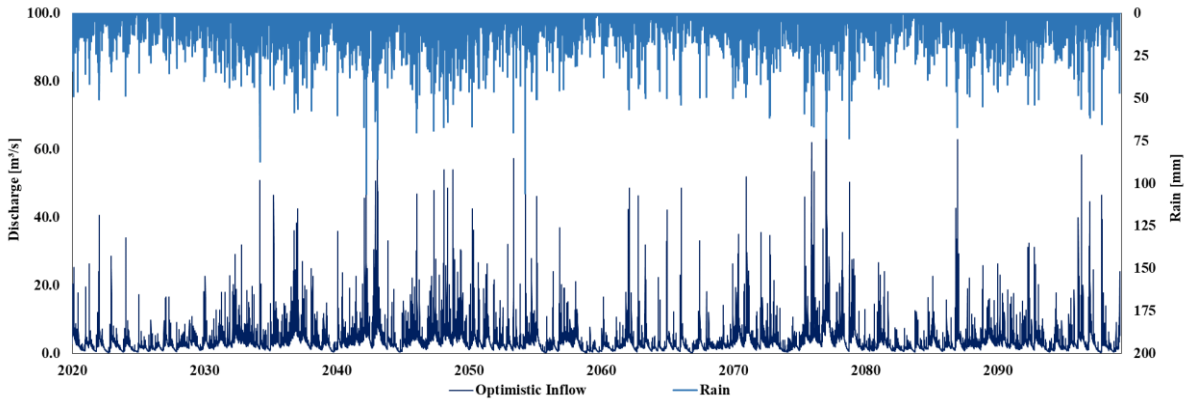


**Figure 34 - Optimistic scenario: Inflow. Source: Author.**

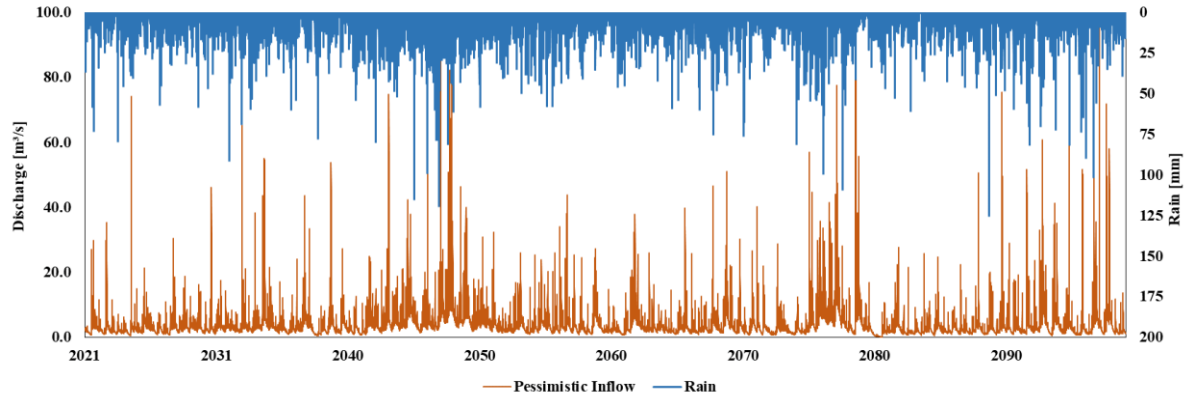


**Figure 35 - Pessimistic scenario: Inflow. Source: Author.**

Comparing both scenarios, it can be noted how, in the pessimistic one, the frequency of extreme events (for wet and dry periods) is higher than in the optimistic one, which presents a less intense and more distributed set of extreme events. These conditions are expected and indicate a good representation of the rain-flow model.

As a next step, the inflow temperatures were estimated with the model air2water (Toffolon *et al.*, 2014), based on the projected air temperature. Using the observed water and air temperature data from the years 2017, 2018 and 2019, the model was calibrated through an automated process (RMSE: 0.93 °C) (Figure 47). The year 2020 was used for the model validation (RMSE: 1.10 °C).

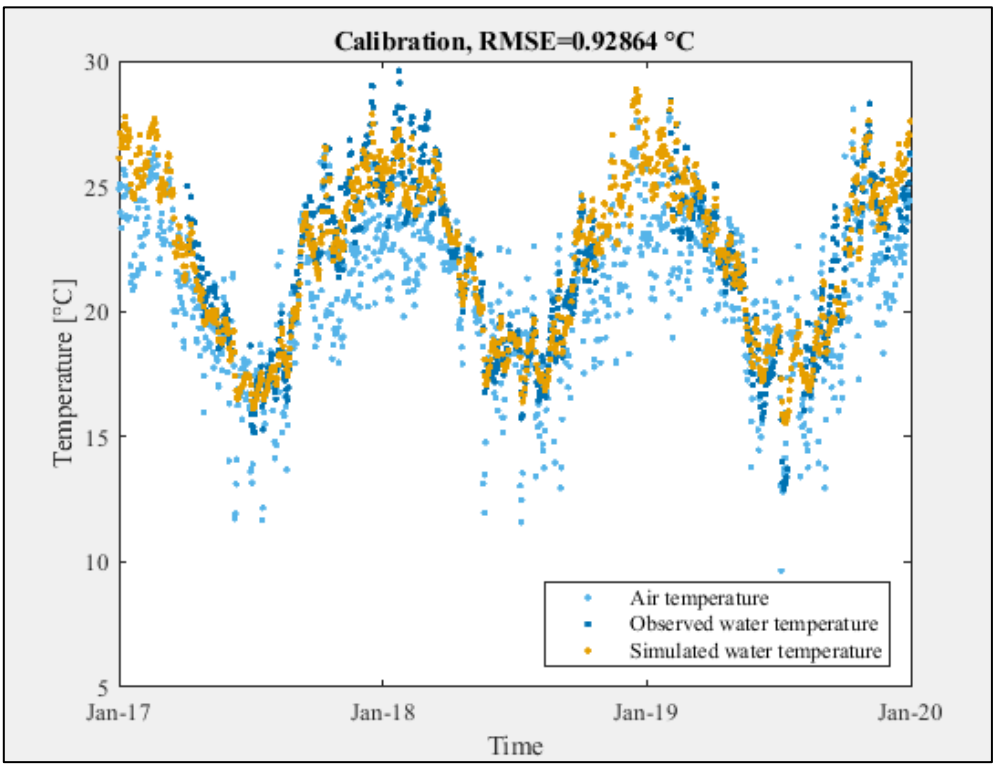


**Figure 36 - Calibration of the air2water model for the Hedberg reservoir. Source: Author.**

Figure 37 presents the comparison between the air temperature projected for the pessimistic scenario (2021) and the water temperature calculated by the air2water model. The latter displays smaller temperature variations, what indicates the higher specific heat capacity of the water in opposition to the air, as expected.

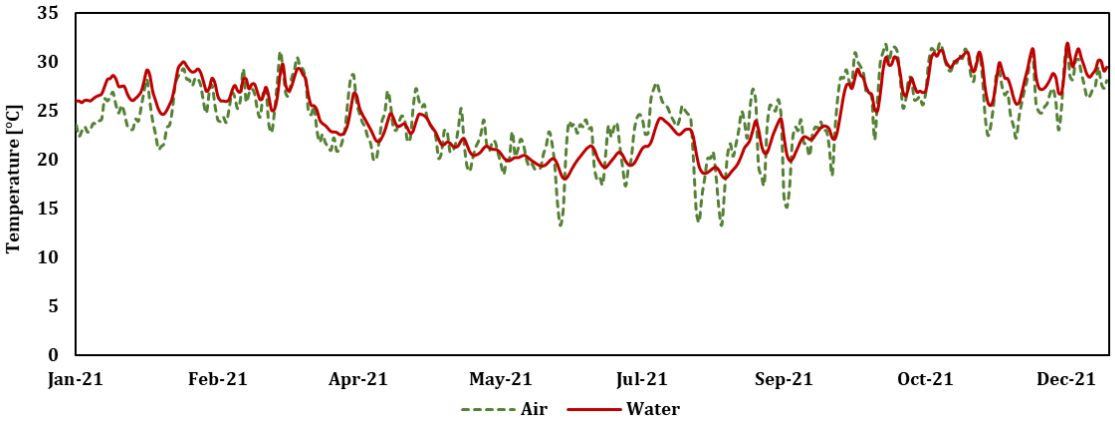


**Figure 37 - Comparison between the predicted air temperature and the calculated water temperature. Source: Author.**

Figure 38 shows the comparison between both climate change scenarios, for the inflow temperature values. The pessimistic scenario, in consonance with its air temperature information, indicates the occurrence of higher temperatures than the optimistic one. This difference is better noted for the distant future set (2070 – 2099). For the near future (2021 – 2040), the temperature data presents similar values in both scenarios.

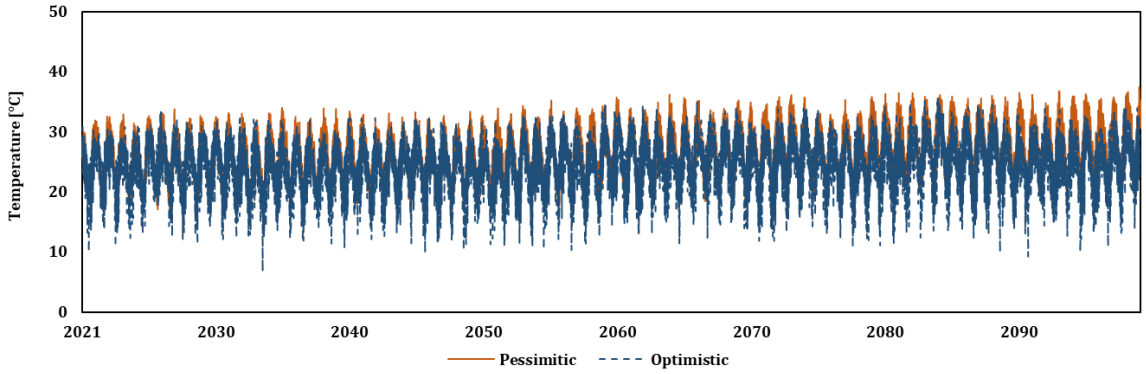


**Figure 38 - Optimistic and pessimistic scenario: Inflow temperature. Source: Author.**

## 6.3 ATMOSPHERIC DATA PREPARATION

In this study, the monitored atmospheric data was compiled and applied to the model in a sub daily time step. Therefore, in order to ensure a better fit between the observed data used for the calibration and validation processes and the climate change scenarios to be simulated, the projected daily data was processed and discretized into average hourly values.

The atmospheric variables discussed are: shortwave solar radiation, air temperature, relative humidity, wind speed and rain.

### 6.3.1 SHORTWAVE RADIATION

The transformation of daily shortwave radiation data into hourly values was based on the formulations presented by Varejão-Silva (2000), using the local latitude, the Julian date and the calculated photoperiod of each day. The data transformation was done in the Matlab environment and the results are shown in Figure 39 (Varejão-Silva, 2000).

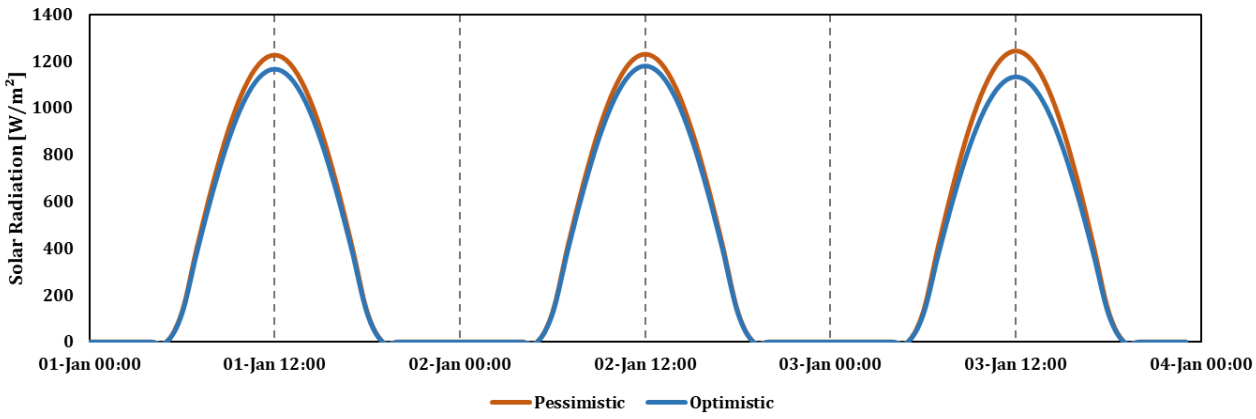


**Figure 39 - Hourly values calculated for the optimistic and pessimistic scenarios (shortwave radiation) (2059). Source: Author.**

### 6.3.2 AIR TEMPERATURE

The discretization of daily air temperature data into hourly values was based on Equations (52) and (53), which take into account the length of the day and night and the maximum and minimum temperature projected for the day. (Parton and Logan, 1981)

$$T_i = (T_x - T_N)\sin\left(\frac{\pi m}{Y + 2a}\right) + T_N \quad (52)$$

$$T_i = T_N + (T_s - T_N)e^{-(bn/Z)} \quad (53)$$

where Y is the day length scale [T]; Z is the day length scale [T]; m is the number of hours after the minimum temperature occurs until sunset [T]; n is the number of hours after sunset until the time of the minimum temperature [T]; a is the lag coefficient for the maximum temperature [-]; b is the nighttime temperature coefficient [-]; Ti is temperature at ith hour [degree]; Tx and $T_N$ are the maximum and minimum temperatures, respectively [degree] and Ts is the temperature at sunset [degree].

For the Hedberg reservoir, the coefficients adopted were a = 0.5 and b = 1.82.

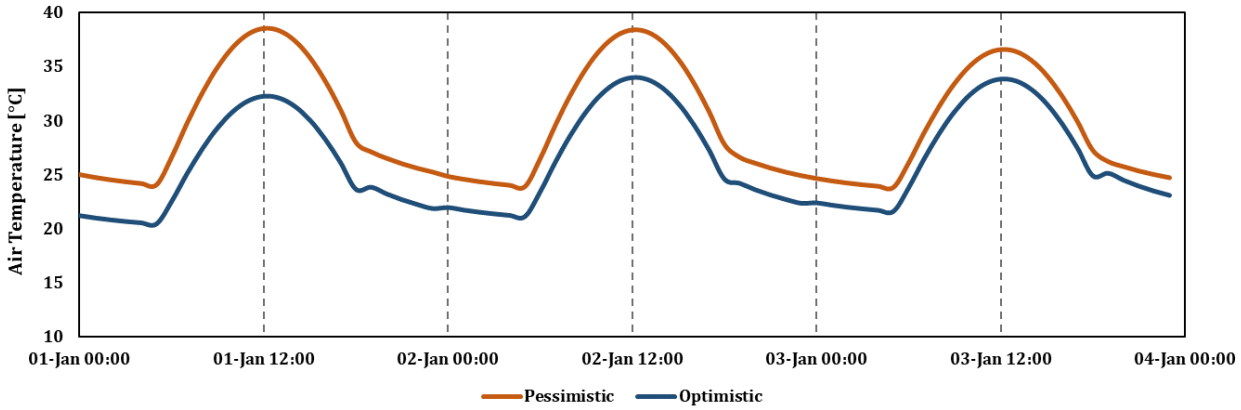


**Figure 40 - Hourly values calculated for the optimistic and pessimistic scenarios (air temperature) (2059). Source: Author.**

Figure 40 presents the hourly values obtained by the method, for January 2059, on both scenarios. The method determined the maximum temperature to occur around 12h00 (noon) and the minimum to occur in the early hours of the day, before sunrise.

### 6.3.3 RELATIVE HUMIDITY

The relative humidity data was transformed into hourly values using the Equation (54), based on Waichler and Wigmosta (2003), accounting for the saturation vapor pressure at the dew point and for the calculated air temperature. (Waichler and Wigmosta, 2003)

$$\mathrm{RU} = \frac{Vs(T_{dew})}{Vs(T)} \tag{54}$$

where Vs ($T_{dew}$) is saturation vapor pressure [$MT^{-2}L^{-1}$] at the dew temperature [degree] and Vs (T) is the saturation vapor pressure [$MT^{-2}L^{-1}$] at temperature T [degree].

Figure 41 displays the hourly values obtained by the applied method, for January 2059. Both scenarios present similar results for the variable during the analyzed period.

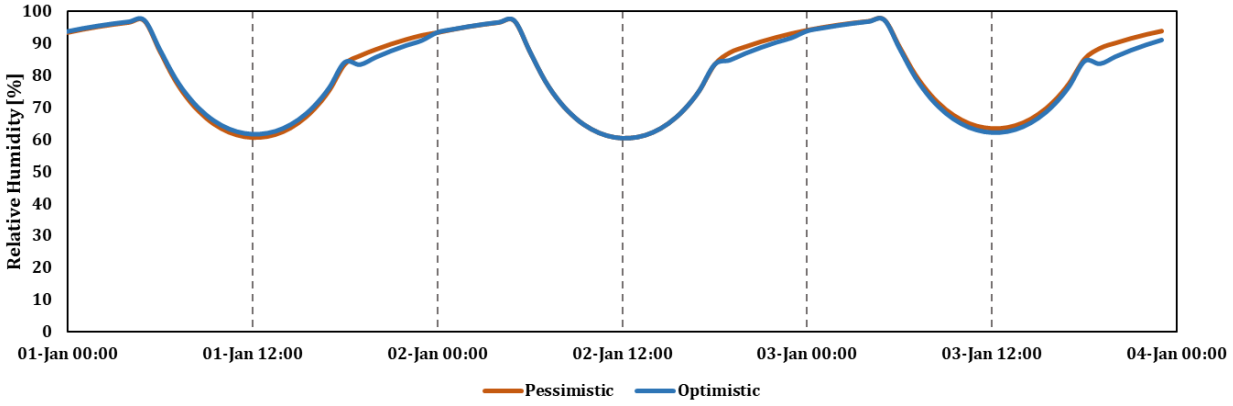


**Figure 41 - Hourly values calculated for the optimistic and pessimistic scenarios (relative humidity) (2059). Source: Author.**

### 6.3.4 WIND SPEED

Local wind speed measurements were analyzed using the Discrete Fourier Transformation, over a two-year period (2017 and 2018). The spectral analysis helped to determine the main frequencies and amplitudes observed on the studied site, which was applied to generate a synthetic series of data. Using the semi-amplitudes and applying a random phase value, the synthetic series was built around the mean daily value. (Equation (55))

$$\text{ws (t)} = \overline{ws} + \sum_{i=0}^{i} a_i \cos(2\pi t f + \delta) \quad (55)$$

where ws is the wind speed [$LT^{-1}$] at t hour [T]; $\overline{ws}$ is the daily mean wind speed [$LT^{-1}$]; $a_i$ is the semi-amplitude of the ith component of the Fourier Series [L]; $\delta$ is the phase associated to the ith component and f is the frequency of the ith component [$T^{-1}$].

The applied method results in values that fluctuate around the projected daily mean. Thus, the method ensures that during a period of time, the mean value of the series is similar to the projected one.

The process was applied for the optimistic and pessimistic scenarios, using the same phase value. The data transformation was performed in the Matlab environment and the results are shown in Figure 42

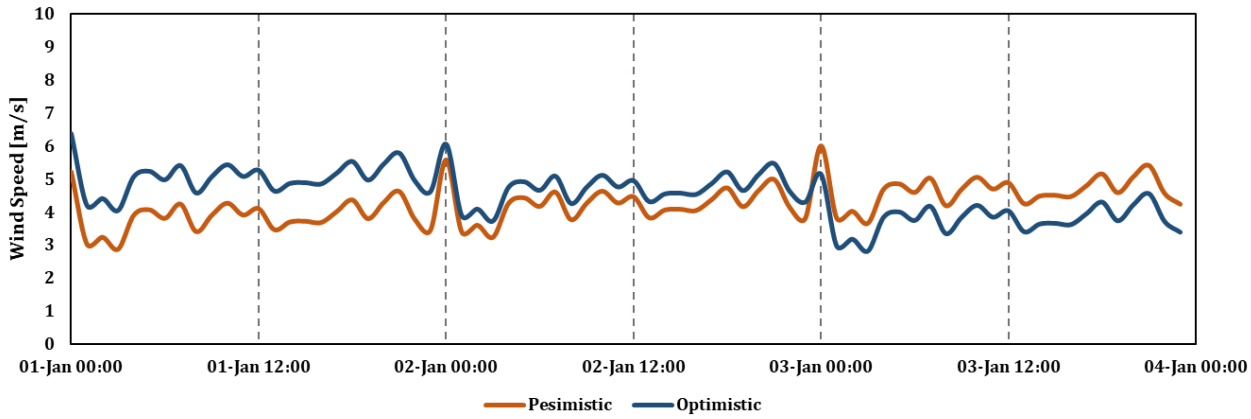


**Figure 42 - Hourly values calculated for the optimistic and pessimistic scenarios (wind speed) (2059). Source: Author.**

### 6.3.5 RAIN

Since the GLM model accounts for the water balance in a daily time step, the projected rain did not have to be discretized in a sub daily time step. Its values were set to be provided to the model at 12:00 (noon), each day.

## 6.4 COMPARISON OF CLIMATE CHANGE SCENARIOS AND THE OBSERVED DATA

Atmospheric variables predicted by the climate change scenarios (2021 to 2099) were compared to the observed data (2017 to 2020), as annual average values. The comparison aimed to identify trends on the predicted data, in order to support the results assessment (*Figure 43*).

Since the beginning of the climate change scenarios (2021), it can be noted that the atmospheric variables present higher values than the observed years, indicating that the future projections are magnified in relation to the observations. The air temperature is 10% higher for the optimistic scenario (O) (20% in the pessimistic (P)), the relative humidity is 5% higher for both scenarios, and the wind speed is increased 250% for the optimistic one (260% for the pessimistic).

Bias correction can be performed in order to reduce the impact of the projected data on the simulation results. The projected bias can impact the intensity and distribution of the variables throughout the simulated period. Studies indicate that climate models, if not corrected, can predict alterations to the existing pattens, affecting precipitation seasonality (Sumka, 2017) and increasing or reducing events intensity (Gutowski *et al.*, 2003).

However, this analysis was not carried out on this study, since the bias information was only used to support the climate change trends evaluation.

These trends indicate increases on the air temperature, over the century, as the distant future presents temperatures up to 25 °C (25% higher for the optimistic scenario) and 29 °C (44% for the pessimistic one).

The relative humidity displays similar values for both scenarios and the observations, without a noteworthy trend. Although, small variations between dry and wet years (for example, 2059 (dry) and 2075 (wet)) can be identified.

The wind speed variable exhibits higher values than the observed scenarios throughout the years. The pessimistic scenario tends to have smaller values than the optimistic one.

For the precipitation variable, no singular trend is observed, for either scenario. This variable presents intense variations over the years, indicating the occurrence of extreme conditions, of dry and wet periods.

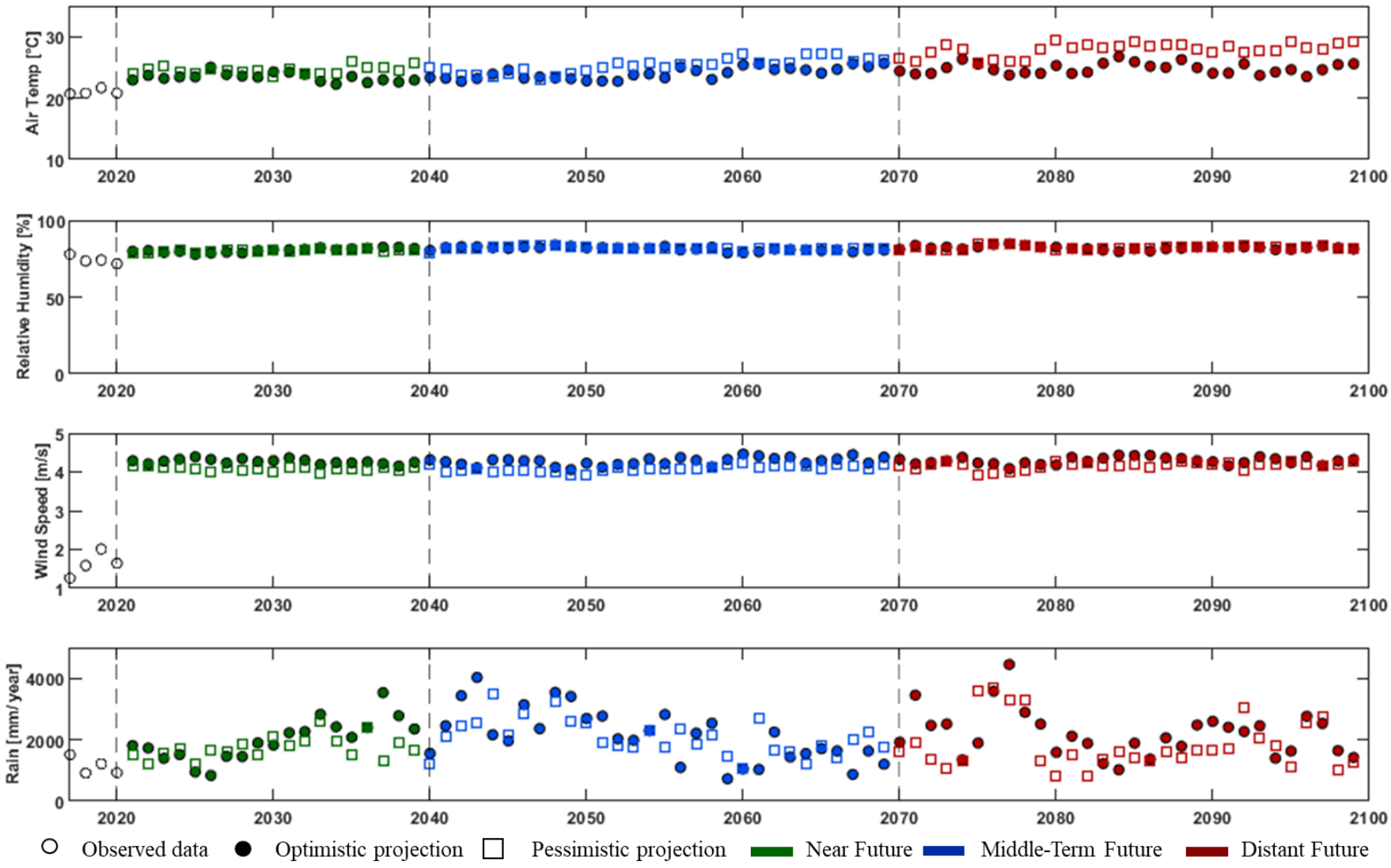


**Figure 43 - Comparison between optimistic and pessimistic scenarios and the observed data. Source: Author.**

# 7 METHODOLOGICAL APPROACH

The methodological approach, applied in this study, proposes the literature review of lake's hydrodynamic processes and mathematical modeling; the investigation of the GLM model; the data compilation, preparation and analysis of the studied site; and the simulation and evaluation of two climate change scenarios.

This chapter discusses the model setup for the calibration and validation processes, the performance indexes used for the model evaluation, the model setup for the climate change simulations and the approach used to assess its results.

## 7.1 THE MODEL SET UP

This study applied the General Lake Model (Version 3.0.5) to simulate the hydrodynamic behavior of the Hedberg Reservoir, through a one-dimensional approach. The GLM code was compiled in the R environment (R Core Team, 2020) and the following packages were used: GLM3r (Hipsey *et al.*, 2019) and glmtools (Read *et al.*, 2014).

In the Hedberg Reservoir, the second buoy (Figure 22), located at the center of the lake, was chosen as the representative vertical profile of the lake, due to the longer period of available monitoring data and its placement, which it is expected to reduce the lake's edges influence.

On the GLM, the user's main interface is the glm3.nml file, where the model structure is organized into sections (i.e., setup, morphometry, time, meteorology, etc) and the user is able to indicate input and output files paths, adjust parameters values and select between the optional modes of the model.

In this study the GLM optional modes selected were: light_mode = 0 (define the light extinction coefficient as the light calculation approach); rad_mode = 1(sub-daily insolation data provided); cloud_mode = 1 (define Idso and Jackson (1969) as the atmospheric emissivity calculation option used); albedo_mode = 1 (define Hamilton and Schladow (1997) as the albedo calculation option used); deep_mixing = 1 (define the hypolimnetic mixing approach as constant diffusivity).

The simulation time framework was from January 2017 to December 2020, with hourly time-steps. The initial depth of the lake was set at 4.1 m, as observed from the monitoring data (for January, 1st, 2017 at 00h00). Whereas the overall lake and inflow salinity was set at 0.0005 mg/L, in order to reduce its influence over the studied domain, once its impacts are not considered relevant in a freshwater environment.

Table 6 presents the input data used during the simulation.

**Table 6 - Input data used for the simulation of Hedberg Reservoir (2017 - 2020). Source: Author.**

| Parameters | Frequency | Components | Units | File Type | Requirement | Dataset |
|---|---|---|---|---|---|---|
| Inflows | Daily | Time; Flow; Temperature; Salinity | [m³/s]; [°C]; [mg/L] | inflow.csv | 1 Inflow - Ipanema River | *Figure 19* |
| Rainfall | Hourly | Rainfall depth | [m/day] | met.csv | - | *Figure 16* |
| Shortwave Radiation | Hourly | Radiation intensity | [W/m²] | met.csv | rad_mode = 1 | *Figure 16* |
| Cloud Cover | Hourly | Cloud cover fraction data | - | met.csv | rad_mode = 1 | - |
| Air Temperature | Hourly | Average air temperature | [°C] | met.csv | - | *Figure 16* |
| Relative Humidity | Hourly | Average relative humidity [0 - 100] | [%] | met.csv | - | *Figure 16* |
| Wind Speed | Hourly | Average wind speed 10 m above the water surface | [m/s] | met.csv | - | *Figure 16* |
| Hypsographic Curve | - | Height-Area Relationship | [m] x [m²] | .nml | Npoints = 33 | *Figure 14* |
| Initial Profile | - | Depths; Temperatures; Salinity | [m]; [°C]; [mg/L] | .nml | Depth [0.5, 1.5, 2.5 and 3.5]<br>Temp [24, 21.5, 21, 20.8]<br>Salinity [0.005, 0.005, 0.005, 0.005] | - |

Since the longwave radiation data was not available, the model (rad_mode = 1) estimates it according to the local cloud cover, which was set to 0 throughout the simulation framework.

Outflow values were, also, not directly provided to the model, but rather, the local spillway was modeled through a surface withdraw structure, placed at the height 548 m. The sediment' mean temperature (19.2 °C) and peak day of the year (30 – Julian) were obtained by the bottom sensor in the second buoy (*Figure 23*). The sediment amplitude was considered 0 °C in this study.

Finally, the layers minimum volume, as well as the maximum number of layers, were set at: 0.01 and 900, respectively. These parameters hold the simulation more coherently and steady.

Parameters not specifically mentioned in this study were set to default values of the model.

## 7.2 CALIBRATION AND VALIDATION

Observed data from 2017 and 2018 was used to calibrate the model, whilst the validation was performed during the years 2019 and 2020. Due to the available observed data, the water balance was calibrated between January and December, 2017 and validated from January to September, 2018. The energy balance, however, was calibrated with data from April, 2017 to September, 2018 and validated from February, 2019 to December, 2020, with some periods lacking data. Both balances were assessed during wet and dry seasons.

For the water balance, two proxies were evaluated: the outflow discharge over the modeled spillway and water level of the lake. The weir performance was calibrated against the outflow values observed for the local discharge curve and the water level with the observed data. Both proxies were analyzed by daily mean values.

The calibration parameters adopted were: $c_{D\,weir}$, $W_{weir}$ (Equations (*39* and (*40*), $f_{ro}$, $R_L$ (Equation (*34*), accounting for the processes of overflow and runoff.

In order to assess the performance of the lake, the indexes MAE (Equation (9)), NMAE (Equation (11)), RMSE (Equation (10)), NSE (Equation (12)), and *r* (Equation (13)) were evaluated. The first 30 days of the simulation were not considered, to assure the exclusion of the model's warming period.

For the energy balance calibration and validation processes, the water temperature was selected as the proxy (at depths: 0.5, 1.5, 2.5 and 3.5 m). The observed data at these depths are presented in Figure 26 and Figure 27. The calibration was assessed in hourly mean values.

The calibration parameters adopted were: $K_W$ (Equation (*41*), $lw_{factor}$, $c_e$ (Equation (23)), $c_d$ (Equation (8) and (*43*)), $C_k$ (Equation (*42*), (*43*) and (*44*)), $C_w$ (Equations (*43* and (*46*), $C_S$(Equation (*51*)), $C_{HYP}$, $K_{soil}$ (Equation (25)), accounting for the processes of surface heating (shortwave radiation, longwave radiation and evaporation), wind stirring, diffusive transport on the hypolimnion and sediment heating.

At this stage, the performance indexes evaluated were, also, the MAE, NMAE, RMSE, NSE, and *r*. Since the hydraulic simulation started at January, 2017, during the temperature calibration process, the model was restarted at April, 2017 (near the start of the temperature monitored period) in order to ensure the best adjustments to the initial observed data. The model was restarted at January, 2018, February, 2019 and October, 2020, with the same purpose.

Table 7 indicates some performance indexes values (RMSE and NSE) found in the literature.

**Table 7 - Performance indexes values found in the literature for studies with the General Lake Model. Source: Author.**

| Lake | Depth | RMSE [°C] | NSE | Reference |
|---|---|---|---|---|
| 32 Lakes around the world | Full Profile | 0.72 - 2.14 | 0.77 - 0.97 | Bruce et al. (2018) |
| | Epilimnion | 0.53 - 4.32 | 0.52 - 0.98 | |
| | Hypolimnion | 0.34 - 3.64 | -3.05 - 0.9 | |
| 434 Lakes (USA) | Full Profile | 2.78 | | Read et al. (2014) |
| | Epilimnion | 1.74 | | |
| | Hypolimnion | 3.33 | | |
| Lake Mendota (USA) | Full Profile | 1.78 - 2.26 | 0.87 - 0.92 | Ladwig et al. (2021); Farrell et al (2020) |
| | Epilimnion | 1.3 - 1.77 | 0.97 | |
| | Hypolimnion | 1.55 - 2.43 | 0.2 | |
| Lake Sunapee (USA) | Epilimnion | 1.06 | | Farrell et al (2020) |
| | Hypolimnion | 1.44 | | |
| Nam Co (China) | Epilimnion | 0.854 | | Huang et al. (2017) |
| | Hypolimnion | 0.426 | | |
| Paranoá Lake (Brazil) | Full Profile | 1.47 | -0.41 | Barbosa (2015) |
| | Epilimnion | 1.9 | -0.3 | |
| | Hypolimnion | < 2.0 | -0.81 - 0.14 | |
| Pampulha Lake (Brazil) | Full Profile | 0.7 | | Silva et al. (2015) |

| | | | |
|---|---|---|---|
| Passaúna Reservoir (Brazil) | Full Profile | 0.81 - 2.28 | Sales (2020) |
| Serra Azul Reservoir (Brazil) | Full Profile | 1.3 - 2.08 | Soares (2018) |
| Descoberto Reservoir (Brazil) | Full Profile | 1.01 - 1.05 | Pinto (2018) |
| | Epilimnion | 1.2 | |
| | Hypolimnion | <1.01 | |

The calibration process was performed manually, applying an interactive trial and error process with the adjustment of the model parameters, through visual evaluation, and performance indexes assessment.

The GLM manual calibration has been shown effective in recent studies (Soares, 2018; Farrell *et al.*, 2020; Sales, 2020a). However, the use of automatic calibration routines has also been applied and points to interesting and promising results. The Markov Chain Monte Carlo (Silva *et al.*, 2015; Huang *et al.*, 2017), the Particle Swarm Optimization (Pinto, 2018) and the GLMGui (Bueche *et al.*, 2020) are some of the employed routines.

Initially, in this study, the application of an automatic calibration routine was attempted, using the Particle Swarm Optimization method. But the method was abandoned in order to better develop the modelist sensibility towards the model, because, although presenting good results, the automatic process was dissipating part of the control away from the student, undermining the learning experience of a beginner modelist. Nonetheless, it is an interesting process to be explored further on.

## 7.3 MODEL SET UP: CLIMATE CHANGE SCENARIOS

For the climate change scenarios simulations, an hourly time-step was applied, in accordance calibration and validation processes. The model was run from 2021 to 2099 (79 years). The input dataset used is shown in Table 8. The hypsographic curve was the same from the previous simulations, once erosion and sediment deposition in the lake basin are not been considered. The initial depth of the lake was set at 4.56 m, the observed value at the beginning of 2021.

**Table 8 - Input data used for the simulation of climate change scenarios on the Hedberg Reservoir (2021 - 2099). Source: Author.**

| Parameters | Frequency | Components | Units | Data Source | Requirement |
|---|---|---|---|---|---|
| Inflows | Daily | Time; Flow; Temperature; Salinity | [m³/s]; [°C]; [mg/L] | SMAP model and Air2Water model | 1 Inflow - Ipanema River |
| Rainfall | Hourly | Rainfall depth | [m/day] | PROJETA data [adapted] | - |
| Shortwave Radiation | Hourly | Radiation intensity | [W/m²] | PROJETA data [adapted] | rad_mode = 1 |
| Cloud Cover | Hourly | Cloud cover fraction data | - | PROJETA data [adapted] | rad_mode = 1 |
| Air Temperature | Hourly | Average air temperature | [°C] | PROJETA data [adapted] | - |
| Relative Humidity | Hourly | Average relative humidity [0 - 100] | [%] | PROJETA data [adapted] | - |
| Wind Speed | Hourly | Average wind speed 10 m above the water surface | [m/s] | PROJETA data [adapted] | - |
| Initial Profile | - | Depths; Temperatures; Salinity | [m]; [°C]; [mg/L] | Observed data [year 2021] | Depth [0.5, 1.5, 2.5 and 3.5] Temp [26.52, 26.47, 25.16, 24.51] Salinity [0.005, 0.005, 0.005, 0.005] |

## 7.4 CLIMATE CHANGE ASSESSMENT

The climate change scenarios assessment was performed through the analysis of four hydrodynamic indicators: water level, epilimnion temperature, hypolimnion temperature and the Schmidt Number. The indicators were selected in regard to their importance over the representation of the hydrodynamic processes, their use in scientific researches about climate change impacts and the ease to calculate them for the extensive dataset (79 years).

The Lake Analyzer tool (Read *et al.*, 2011) was used for the indicators calculation. The Lake Analyzer (v. 3.4.0) is an analysis script, developed by GLEON, used to help models' assessment

and estimate different lake metrics. The script was developed in a Matlab environment and is available online, being well fitted for the GLM analysis.

For this study, in order to better assess the data over 79 years, the hourly results were averaged into year-long values. The limitations implied by this approach are the misrepresentation of seasonal variations and underestimation of extreme events. However, the indicators' tendency and the estimation of their impact over the lake's thermal regime, the objective of this study, are well represented.

# 8 RESULTS AND DISCUSSION

This chapter focuses on presenting the simulation results and discussion, addressing the hydrological and thermal patterns observed in the Hedberg reservoir and their representation by the GLM model, in the light of the model's performance, limitations and biases. Finally, the assessment of the climate change scenarios impact over the Hedberg thermal behavior is also discussed. For that, four indicators are used: epilimnion and hypolimnion temperature, the Schmidt Number and the thermocline depth.

Therefore, this chapter aims to address the third, fourth and fifth specific objectives of this study.

## 8.1 HYDRODYNAMIC MODEL PERFORMANCE

### 8.1.1 Observed thermal patterns

The Hedberg reservoir is a tropical, shallow lake (mean depth 4.5 m), located at the end of a 234-km² watershed (*Figure 13*), with the local spillway as the main outflow structure.

Presenting a polymictic pattern, the lake's thermal behavior can be assessed by the daily variations observed along the vertical temperature profile. During the day, the incident solar radiation provides enough energy for the water column of the lake to establish the stratification, mainly in the first few meters; however, during the night, due to convective processes (water cooling), short mixing events lasting up to 2 or 3 hours can be observed early in the morning, before the incoming solar radiation restarts the stratification (Figure 44).

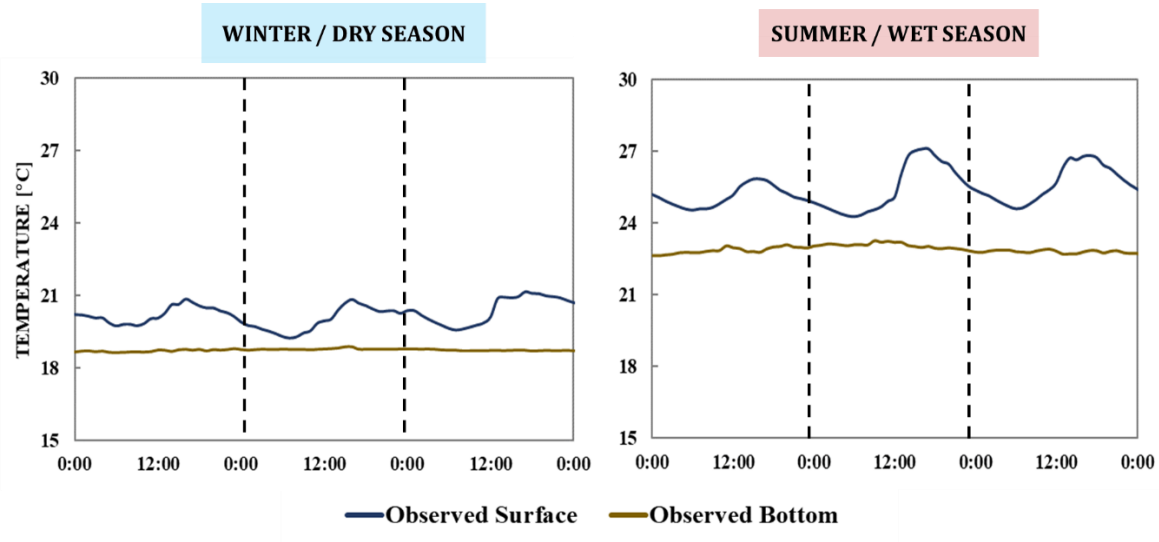


**Figure 44 - Observed daily thermal patterns on the Hedberg reservoir, during winter (left) and summer (right). Source: Author.**

Mixing events during the day can also be generated by the wind stirring onto the surface of the lake, but those are less frequently observed.

Throughout the year, the seasonal variations influence the Hedberg thermal patterns (Figure 45). The winter is the local dry season, therefore, lower flow discharges, colder inflow and surface water temperatures, along with the reduction of the solar radiation intensity, bring about the occurrence of long overturning events, which can be maintained for a few days. In the summer, on the other hand, elevated radiation intensities, along with warmer inflow and surface water temperatures, promote stronger stratification profiles and only short mixing events take place.

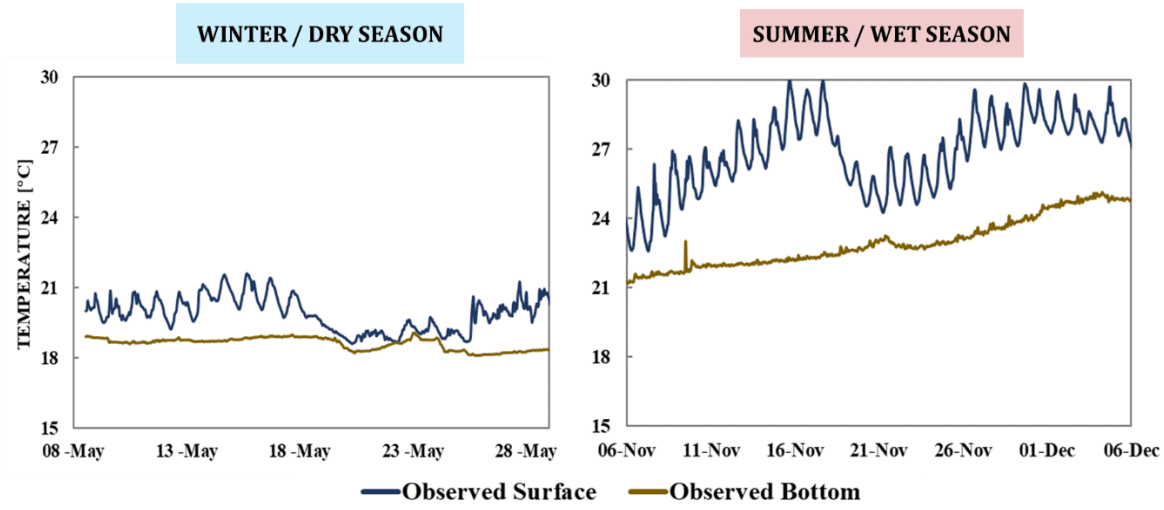


**Figure 45 - Observed seasonal thermal patterns on the Hedberg reservoir, during winter (left) and summer (right). Source: Author.**

For the Hedberg reservoir, the period from April to September (monthly mean rain: 25 mm), which is during winter, was considered as the dry season, and the one from September to March (monthly mean rain: 115 mm), over the summer, as the wet season.

In this study, the model was calibrated and validated for the years 2017 to 2020, including dry and wet periods.

### 8.1.2 Water Balance

The lake's water balance was evaluated by two important proxies: the outflow discharge and the surface water level. The first takes place at the local spillway, whose placement allows the reservoir to work as a run-of-the-river dam. The latter indicates the variations within the volume of the system.

Observed data indicates that, throughout a regular year, the Hedberg outflow discharge varies between 1 and 20 $m^3/s$, as the water level ranges from 548.5 m to 549.5 m, with the wet season presenting higher values, mainly during flood events.

In 2017, two extraordinary flood events were observed. During the wet season, at the beginning of February, intense rain raised the water level up to 549.6 m and generated discharges of 31 $m^3/s$. However, the event that took place in early June, in response to an unusual rain event during the

dry season, generated discharges of 35 m³/s and elevated the surface level up to 549.8 m. The event was the most extreme flood observed over the monitoring period available.

Regarding the unusual characteristics of both events, mainly the one during the dry season, the calibration focus was to achieve the best representation of the lake's response outside of these periods.

Table 9 presents the parameters and values calibrated for the water balance.

**Table 9 - Calibration and validation parameters (water balance). Source: Author.**

| Parameter | | Initial Values | Calibration | Units | Associated Process |
|---|---|---|---|---|---|
| Weir drag coefficient | $c_{D\ weir}$ | 0 | 180.585 | - | Overflow |
| Width of the weir crest | $W_{weir}$ | 0 | 160 | m | Overflow |
| Runoff factor | $f_{ro}$ | 0 | 1 | - | Runoff |
| Rainfall threshold | $R_L$ | - | 0.04 | m | Runoff |

The outflow discharge calibration was performed in order to evaluate the response of the structure simulated by the GLM. Figure 46 displays the modeled and observed data over the years 2017 (calibration) and 2018 (validation).

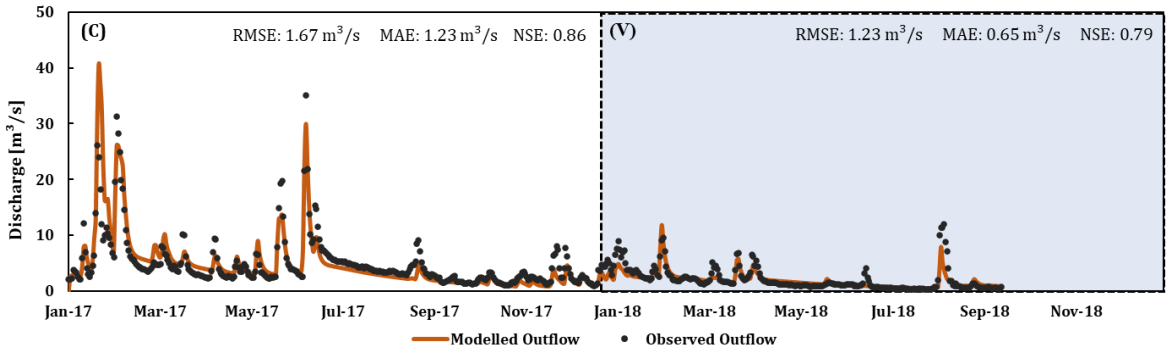


**Figure 46 - Calibration: Outflow discharges (2017). Source: Author.**

The modeled structure response is considered adequate, with the simulated outflow fitting the observed data, even during the extreme events. The main performance indexes calculated reinforce the good fit of the model, with the RMSE value of 1.67 m³/s and the NSE of 0.86 (N=344). Yet, the simulation results are slightly underestimated when compared to the observed data, throughout the year.

After the outflow calibration, the water level response was analyzed (Figure 47). Its performance index values presented good results, with RMSE of 0.16 m and MAE of 0.12 m (N=344). However, the NSE index was estimated at 0.25, indicating an inefficient representation of the level dynamic, which can be observed for the first semester of the year 2017 and explained by the unusual events simulation.

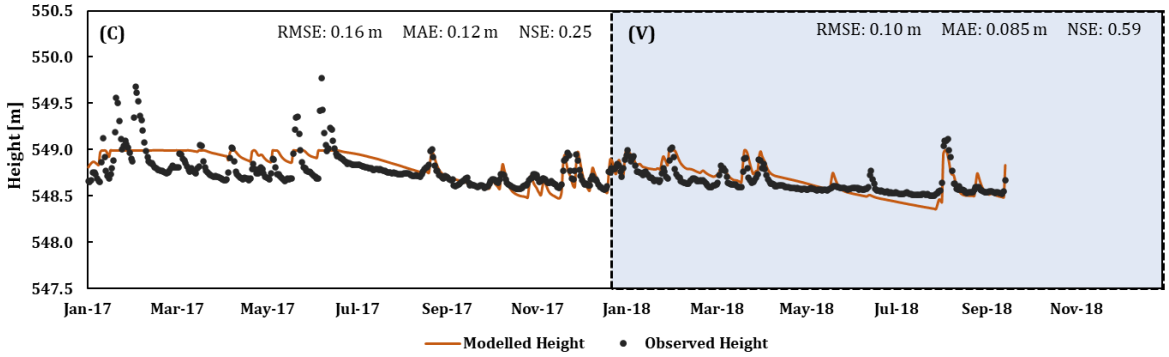


**Figure 47 - Calibration: Water level (2017). Source: Author.**

The water level assessment indicates an appropriate fit during most of the year, but fails to represent the extreme flood events, even with the reliable simulation of the weir structure (Figure 46). As the surface water reaches the height of 549 m, the water level stops rising and all of the excess water is retrieved from the system. This condition may be due to the large width adopted for the weir or the elevated drag coefficient.

During the validation (2018), both proxies were evaluated and presented suitable results, improving their performance index values. The outflow dynamic (Figure 46) had a RMSE of 1.23 m³/s and MAE of 0.65 m³/s, as the water level (Figure 47), without the occurrence of extreme events, presented RMSE of 0.1 m, MAE of 0.085 m and NSE of 0.59 (N = 258).

In conclusion, the GLM model seems to reliably represent the water balance dynamics over the Hedberg reservoir. The local outflow discharges were well characterized by the model's weir, during wet and dry periods. As for the water level, the results indicated a good fit with the observed data, with limitations during extreme flood events, which are underestimated by the model. Table 10 resumes the performance index values for the calibration and validation periods.

**Table 10- Calibration and validation: Performance index values (2017 - 2018) - Water Balance. Source: Author.**

| Variable | Calibration (2017) | | | | Validation (2018) | | | | Whole Period (2017 - 2018) | | | |
|---|---|---|---|---|---|---|---|---|---|---|---|---|
| | N | RMSE | MAE | NSE | N | RMSE | MAE | NSE | N | RMSE | MAE | NSE |
| Overflow [m³/s] | 334 | 1.67 | 1.23 | 0.86 | 258 | 1.23 | 0.65 | 0.79 | 592 | **1.45** | **0.94** | **0.83** |
| Water Level [m] | 334 | 0.16 | 0.12 | 0.25 | 258 | 0.10 | 0.09 | 0.59 | 592 | **0.14** | **0.11** | **0.36** |

### 8.1.3 Energy Balance

Once the water balance of the model provided an adequate representation of the Hedberg hydraulic dynamic, the study focused on the energy balance calibration. The chosen proxy was the water temperature, at four different depths: 0.5 m, 1.5 m, 2.5 m and 3.5 m.

Measured data at these four depths, observed during the 2017-2020 period (Figure 26 and Figure 27), showed that the temperature of the lake varies between 14°C and 30°C. The most pronounced variations have a daily frequency and take place within the first meters of the water column, being better represented by the 0.5 m and 1.5 m depths; whereas, near the bottom (3.5 m), these daily variations have a reduced influence over the temperature, what is indicated by a smoother thermal contour.

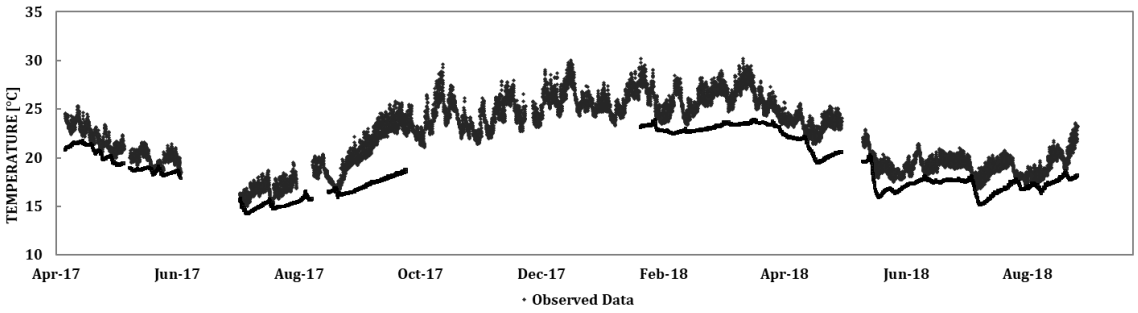


**Figure 48 - Observed data: Water temperature 0.5 and 3.5 m (2017 - 2018). Source: Author.**

The characterization of the upper and bottom layer temperature profiles determines the density structure of the system. Mixing events are observed by the convergence of the distinct temperature contours of each depth, indicating that both depths have similar temperatures at that time and, therefore, belong to the same homogeneous density layer (salt and other dissolved components are disregarded by this study, since the lake is considered a freshwater environment). If the surface (0.5 m) and bottom (3.5 m) temperatures are the same, the lake has presented an overturning event.

In the Hedberg reservoir (Figure 48), major mixing events occur throughout the year, during wet (summer) and dry (winter) seasons, but are most predominant on the latter, due to the reduced water temperature over the lake. Therefore, seasonal patterns are well defined along the observed period, with lower surface and bottom temperatures from June to August, and the rise of temperatures after September, when the stratification events are more distinctively noticeable.

During 2017 and 2018, wet and dry season monitored data were used for the two-year-long calibration. However, the bottom data was available only for three months over the wet season, and eight months of the dry one.

The Hedberg model calibration parameters and their values are presented in Table 11.

**Table 11 - Calibration and validation parameters (energy balance). Source: Author.**

| Parameter | | Initial Values | Calibration | Units | Associated Process |
|---|---|---|---|---|---|
| Light extinction coefficient | $K_W$ | - | 1.185 | $m^{-1}$ | Shortwave radiation |
| Longwave radiation factor | lw_factor | 1 | 1.1 | - | Longwave radiation |
| Bulk aerodynamic coefficient for latent heat transfer | $c_e$ | 0.0013 | 0.0008 | - | Evaporation |
| Drag coefficient | $c_d$ | 0.0013 | 0.0006 | - | Wind stirring |
| Mixing efficiency due to convective overturn | $C_K$ | 0.2 | 0.4 | - | Mixing |
| Mixing efficiency due to wind stirring | $C_w$ | 0.23 | 0.03 | - | Mixing |
| Mixing efficiency due to shear production | $C_s$ | 0.3 | 0.2 | - | Mixing |
| Mixing efficiency coefficient for hypolimnetic turbulence | $C_{HYP}$ | 0.5 | 0.1 | - | Hypolimnion diffusivity |
| Soil-sediment thermal conductivity | $K_{soil}$ | 0.25 – 2.9 | 0.5 | kg m $s^{-3}$ $°C^{-1}$ | Sediment heating |

Besides the parameters displayed on Table 11, the optimal setting of the minimum and maximum layer thickness parameters ($h_{min}$ and $h_{max}$, respectively) were essential to the calibration process. For the Hedberg reservoir, the minimum layer thickness was set to 0.01 m and the maximum to 0.7 m.

It was noted that reducing the maximum layer thickness improved the calibration of the bottom layer, helping the representation of a smoother temperature profile. This reduction attenuated the influence of the upper layer onto the bottom ones, once it pushed the model to calculate the energy balance separately for each layer, resulting in a better representation of stratification events.

However, the same reduction impacted negatively on the representation of the surface layers. The mixing process taking place in the first two meters of the lake was underestimated with the reduction of $h_{max}$. Therefore, an optimal point was sought.

Another important factor was setting the start of the simulation period close to the beginning of the observed temperature data, in order to ensure that the initial conditions were properly set and that the least amount of error was being accumulated.

With those considerations, Figure 49 presents the GLM thermal calibration. The modeled surface and bottom data were compared to the observed temperatures at the 0.5 m and 3.5 m depths, for the 2017-2018 dataset.

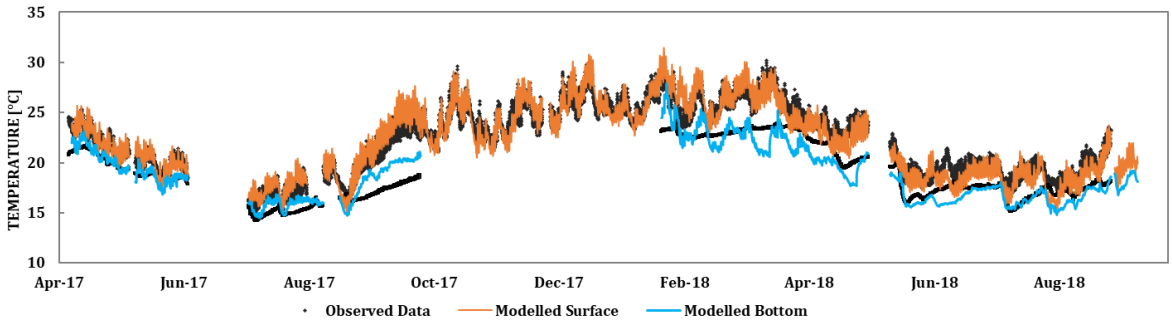


**Figure 49 - Calibration: Water temperature at 0.5 and 3.5m, for the observed and modelled data (2017 - 2018). Source: Author.**

The visual evaluation of the simulated thermal dynamic indicates a good agreement between the observed and modeled data. The seasonal pattern is well represented by the year-long variations, at both depths, with decreasing temperatures from April to July, and increasing values after August. The daily variations are also represented by the upper and bottom layers, with the model displaying larger fluctuations than the monitored data for the latter.

Due to difficulties in calibrating the bottom layer, which is influenced by the dynamic of the upper layers, diffusive processes and the sediment heat exchanges, the 3.5 m-depth simulated temperature presented larger variations than the observed data, incurring a fluctuating temperature profile. This condition resulted in a higher occurrence of mixing events by the GLM simulations, mainly during the wet season, in comparison with the observed data.

A quantitative evaluation, for the full vertical profile (N = 41056), was calculated through the performance indexes: RMSE (1.20°C), MAE (0.93°C), NMAE (0.05) and NSE (0.82). The indexes indicated a great fit between the simulation and monitoring data and are coherent with the literature (*Table 7*).

Figure 50 and Figure 51 display the calibration for each of the four depths and their respective performance indexes. All indexes' values were considered indicators of the model's good fit as the thermal pattern presented is adherent to the observed data.

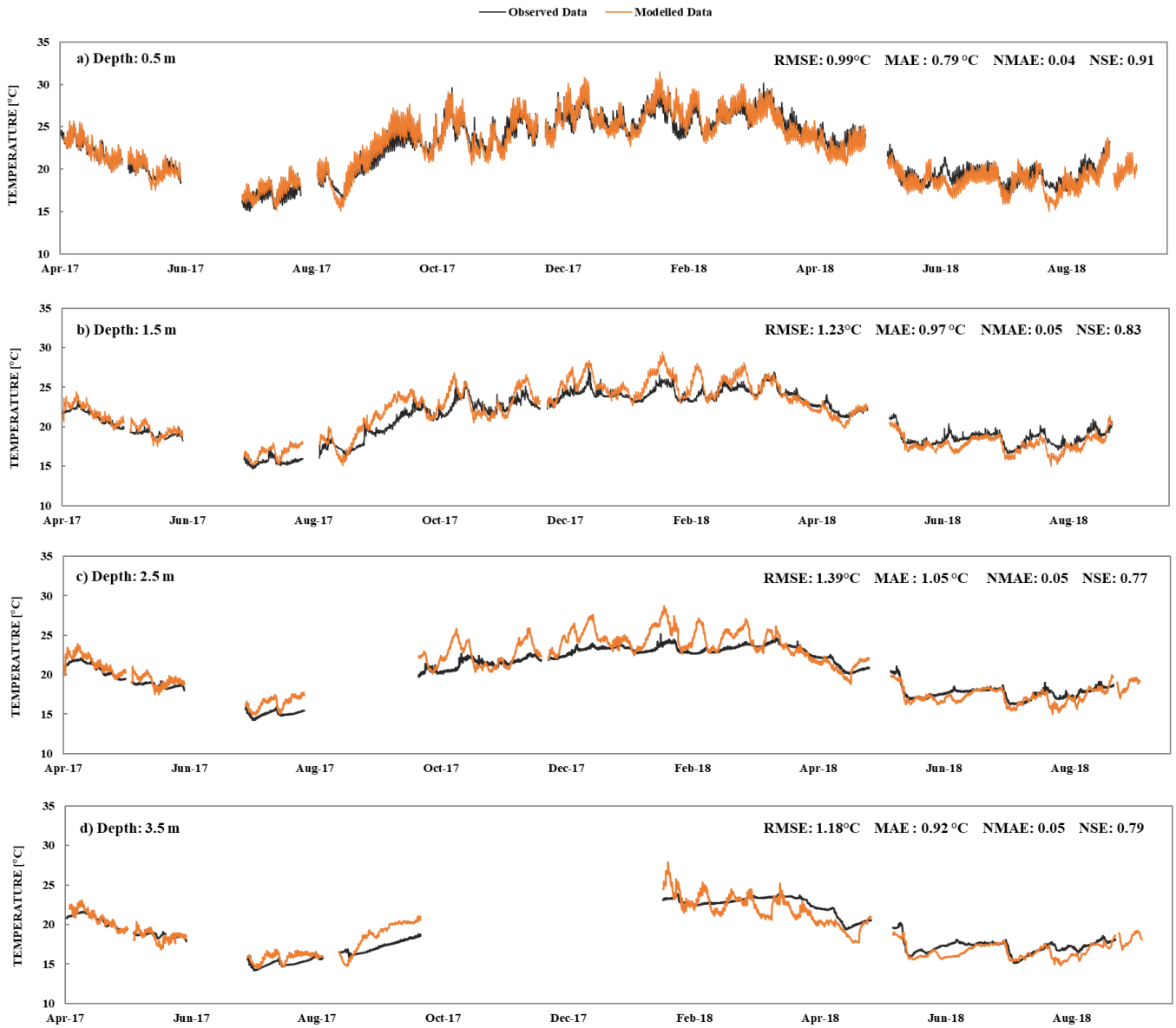


**Figure 50 - Calibration: Water temperature (a) 0.5 m, (b) 1.5 m, (c) 2.5 m and (d) 3.5 m (2017 and 2018). Source: Author.**

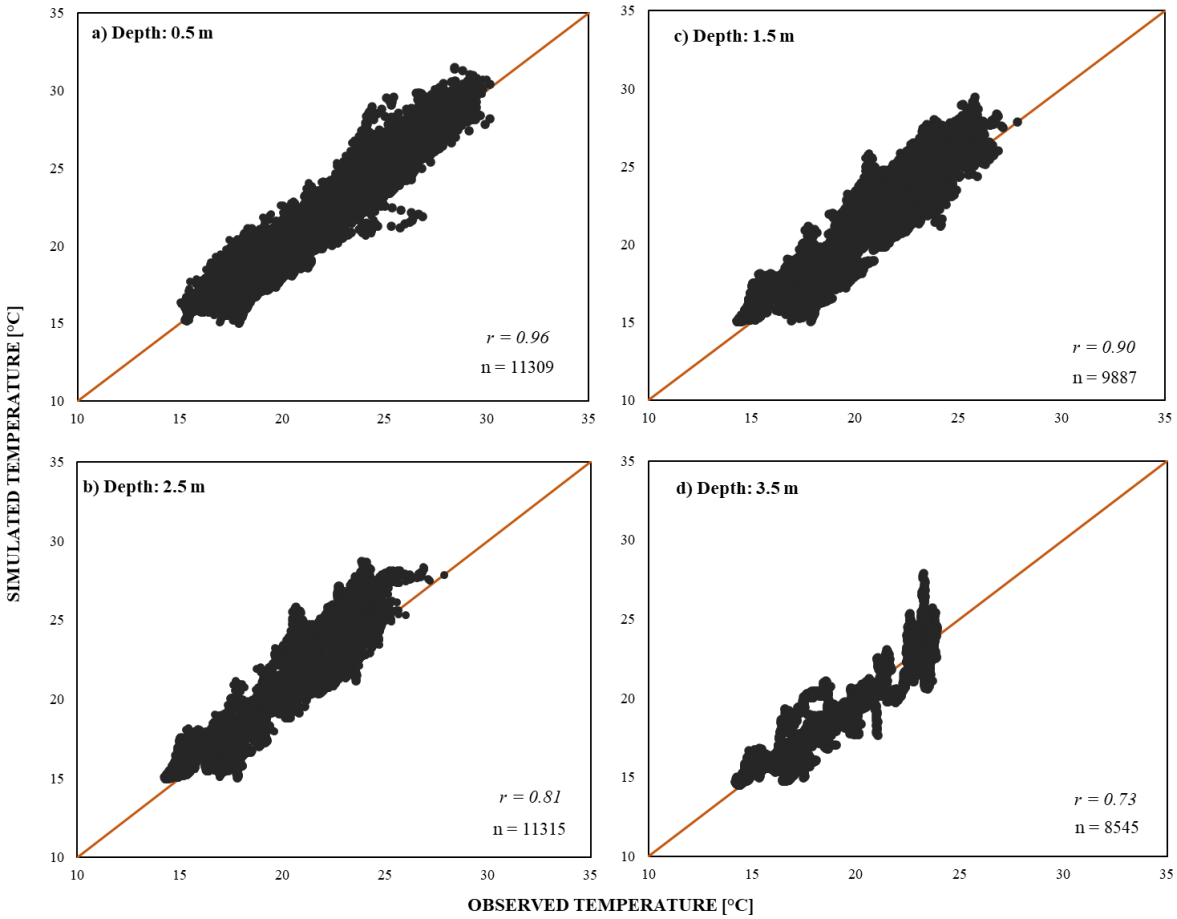


**Figure 51 - Calibration: Water temperature correlation (a) 0.5 m, (b) 1.5 m, (c) 2.5 m and (d) 3.5 m (2017 - 2018). Source: Author.**

The surface and bottom layers exhibited the best performance indexes, with the first associated with a RMSE of 0.99 °C, NSE of 0.91 and r of 0.96 (N = 11309), and the latter with a RMSE of 1.18°C, NSE of 0.79 and r of 0.73 (N = 8545). Yet, the 3.5 m-depth temperature profile was predominantly calibrated with dry period data and, thus, its evaluation over the wet period must be better assessed in the validation.

Overall, the model's performance presented similar results to other reviewed studies developed with the GLM model (Table 7). For the surface layer (epilimnion), literature RMSE values range from 0.7 up to 4 °C and NSE from -0.3 to 0.98. As for the bottom layers (hypolimnion), studies indicated RMSE between 0.3 and 3.6 °C and NSE varying from -3.05 to 0.9.

In Brazilian studies, most RMSE values ranged between 1 and 2 °C, for both the upper and bottom layer, as well as for the full profile. Barbosa (2015) also calculated the NSE for the Paranoá lake and found values ranging from -0.8 up to 0.14.

Therefore, in the light of these results, the calibration was considered adequate, with its results reliably representing the thermal pattern of the Hedberg Reservoir.

The model validation was assessed during the 2019 - 2020 simulation. Figure 52 and Figure 53 present the observed data and the calibrated model response for the 0.5 m and 3.5 m depth.

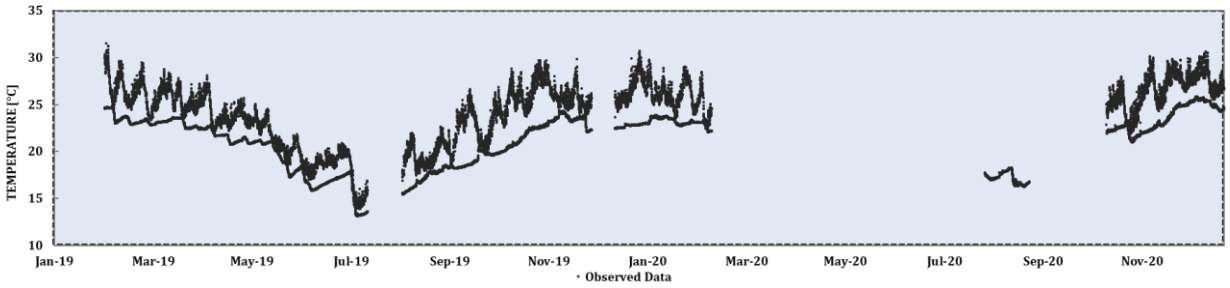


**Figure 52 - Observed data: Water temperature 0.5 and 3.5 m (2019 - 2020). Source: Author.**

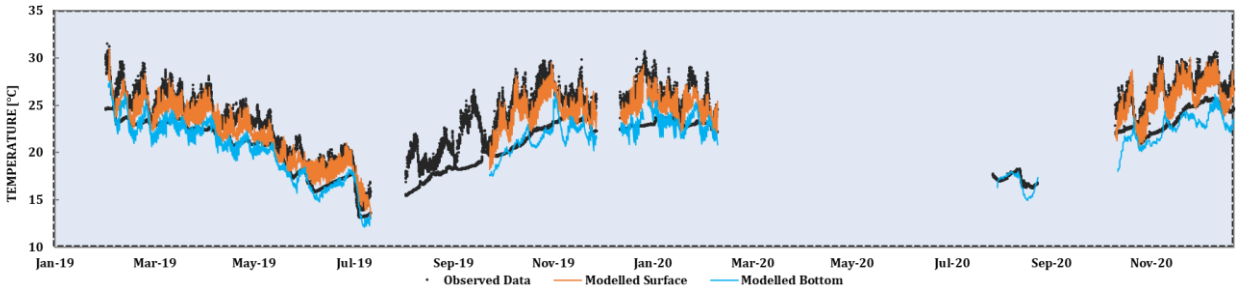


**Figure 53 - Validation: Water temperature at 0.5 and 3.5m, for the observed and modelled data (2019 - 2020). Source: Author.**

Through a visual analysis, the good adherence of the model during the simulated period can be noticed. Once again, the surface layer was well represented, with the seasonal and daily variations properly simulated. The bottom layer, in consonance with the calibration analysis, presented larger thermal fluctuations, resulting in more frequent mixing events, mainly during the wet season.

However, the simulation of October and November, from both years, 2019 and 2020, showed that the model was able to reliably represent great stratification events, with long-lasting characteristics (up to a month), observed during the wet season.

For the full profile analysis (average value over depth), the calculated performance indexes indicated a good fit of the model in relation to the observed data, as well as in the calibration. Its values were also in agreement with the literature (Table 7). The full profile (N = 31032) performance values were: 1.05 °C (RMSE), 0.84 °C (MAE), 0.04 (NMAE) and 0.84 (NSE).

Figure 54 and Figure 55 display the validation analysis at the four depths.

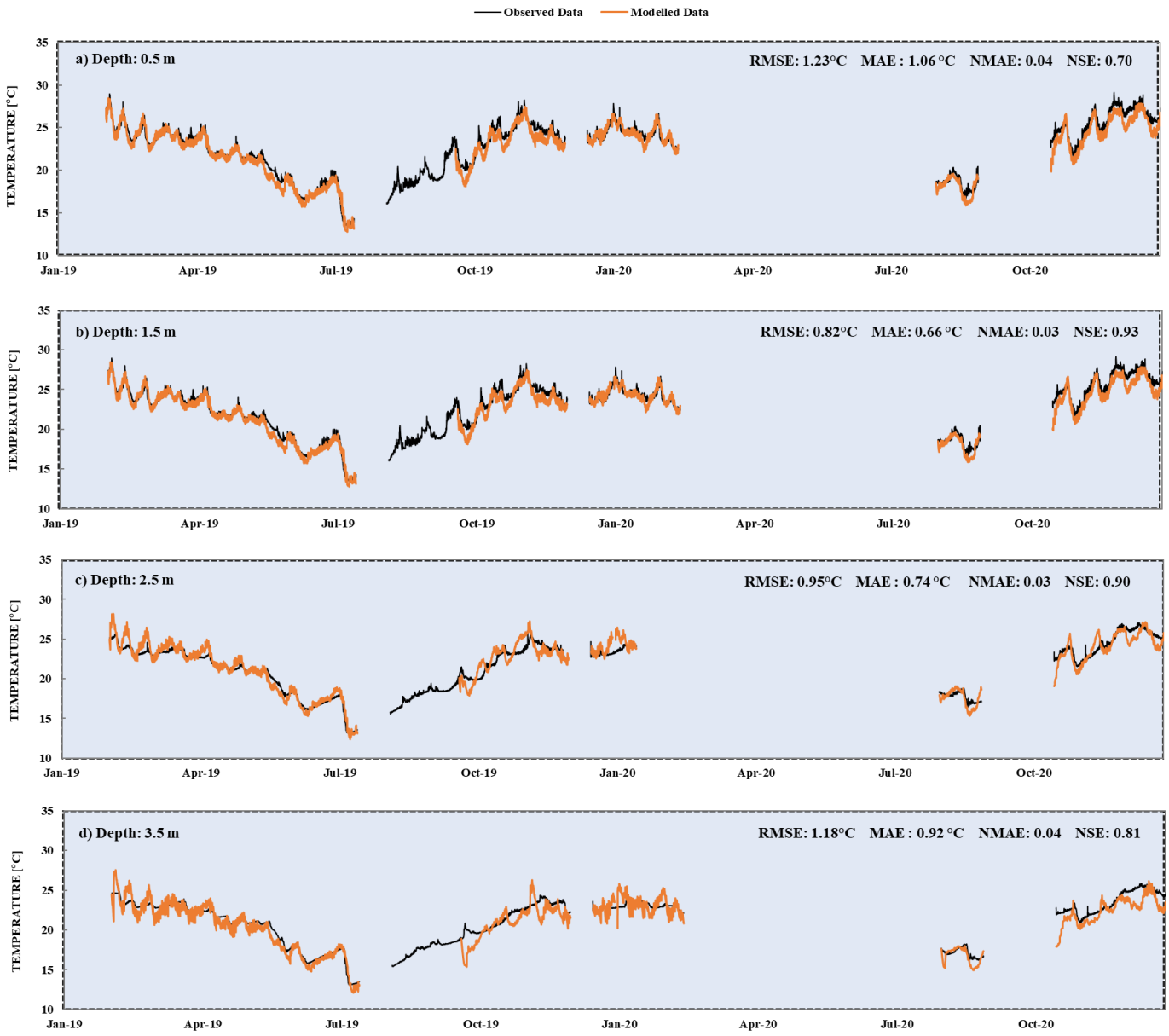


**Figure 54 - Validation: Water temperature (a) 0.5 m, (b) 1.5 m, (c) 2.5 m and (d) 3.5 m (2019 - 2020). Source: Author.**

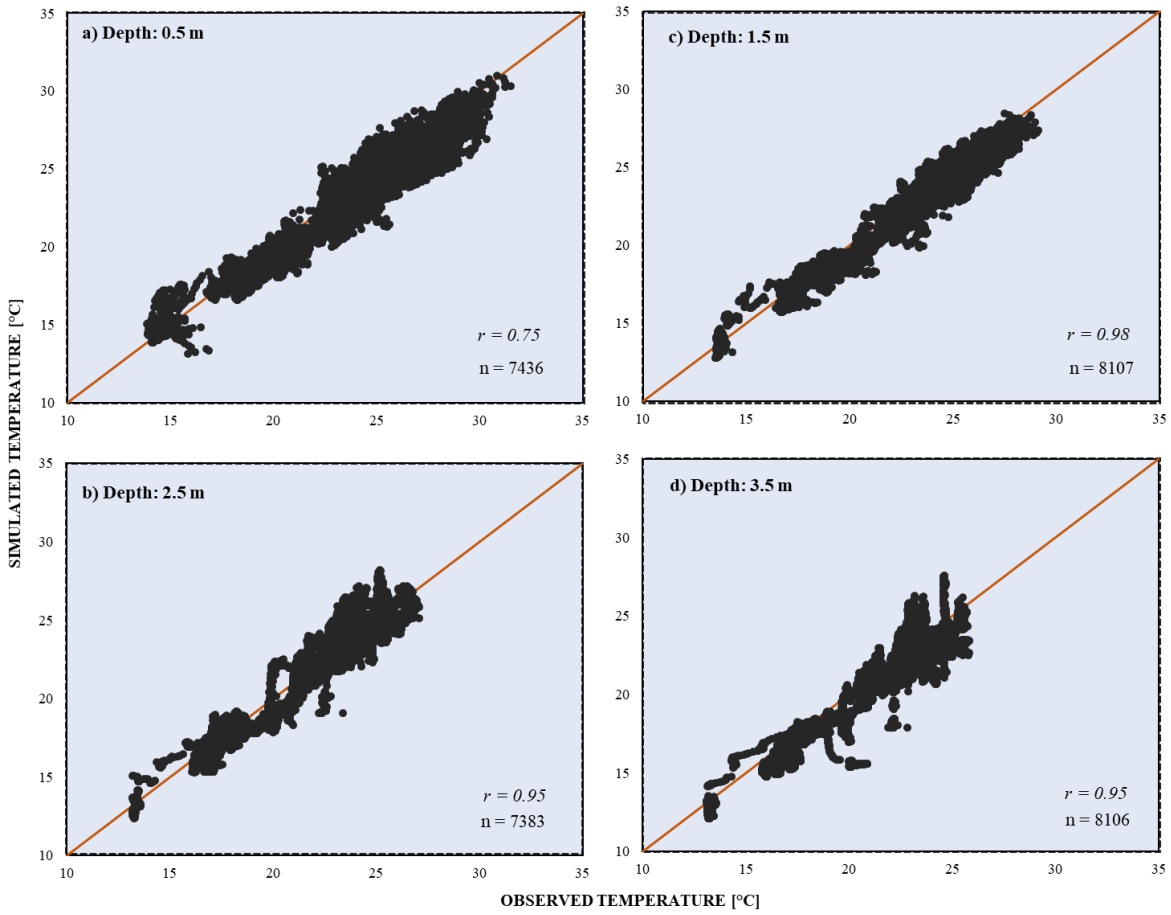


**Figure 55 - Validation: Water temperature correlation (a) 0.5 m, (b) 1.5 m, (c) 2.5 m and (d) 3.5 m (2019 - 2020). Source: Author.**

As discussed, the model presented an adherent thermal pattern with the observed data throughout both years, although temperature fluctuation at 2.5 and 3.5 m are still simulated more frequently than the observed data, overestimating the occurrence of mixing events.

The surface layer did not perform as well for the validation period as for the calibration, with an RMSE of 1.23°C and a NSE of 0.71, yet its values still indicate a great fit between the model and the observed data, in accordance with the literature (Table 7).

On the other hand, the two middle layers (1.5 and 2.5 m) exhibited better performance indexes during the validation, with the 1.5 m depth associated with a RMSE of 0.82 °C, NSE of 0.93 and r of 1.02 (N = 8107), and the 2.5 m depth with a RMSE of 0.95°C, NSE of 0.90 and r of 0.95 (N = 7383).

The elevated values of the linear correlation coefficient (r), close to 1, indicate the great agreement between observed and simulated data, suggesting the high accuracy of the model during the simulation.

At last, the bottom layer disclosed a similar adjustment to the observed data on both simulations, with an RMSE of 1.18°C and NMAE of 0.04 (Calibration) and 0.05 (Validation), indicating that the wet period is as well represented as the dry one, for this depth.

Table 12 and Table 13 summarize the performance indexes RMSE, MAE, NMAE and NSE values calculated for the simulation period (calibration, validation and the overall period). The values are presented by proxy and depth.

**Table 12 – Calibration and validation: Performance indexes values (2017 - 2020) – Energy Balance. Source: Author.**

| Variable | Calibration (2017 - 2018) | | | | | Validation (2019 - 2020) | | | | |
|---|---|---|---|---|---|---|---|---|---|---|
| | **N** | **RMSE** | **MAE** | **NMAE** | **NSE** | **N** | **RMSE** | **MAE** | **NMAE** | **NSE** |
| Water Temperature [°C] | | | | | | | | | | |
| Full Profile | 41056 | 1.20 | 0.93 | 0.05 | 0.82 | 31032 | 1.05 | 0.84 | 0.04 | 0.84 |
| 0.5 m | 11309 | 0.99 | 0.79 | 0.04 | 0.91 | 7436 | 1.23 | 1.06 | 0.04 | 0.70 |
| 1.5 m | 9887 | 1.23 | 0.97 | 0.05 | 0.83 | 8107 | 0.82 | 0.66 | 0.03 | 0.93 |
| 2.5 m | 11315 | 1.39 | 1.05 | 0.05 | 0.77 | 7383 | 0.95 | 0.74 | 0.03 | 0.90 |
| 3.5 m | 8545 | 1.18 | 0.92 | 0.05 | 0.79 | 8106 | 1.18 | 0.92 | 0.04 | 0.81 |

**Table 13 – Performance indexes values (2017 - 2020) – Energy Balance. Source: Author.**

| Variable | Whole Period (2017 - 2020) | | | | |
|---|---|---|---|---|---|
| | **N** | **RMSE** | **MAE** | **NMAE** | **NSE** |
| Water Temperature [°C] | | | | | |
| Full Profile | 72088 | **1.13** | **0.89** | **0.05** | **0.83** |
| 0.5 m | 18745 | 1.11 | 0.93 | 0.04 | 0.81 |
| 1.5 m | 17994 | 1.03 | 0.82 | 0.04 | 0.88 |
| 2.5 m | 18698 | 1.17 | 0.90 | 0.04 | 0.84 |
| 3.5 m | 16651 | 1.18 | 0.92 | 0.05 | 0.80 |

Figure 56 displays the hydraulic and thermal behavior of the Hedberg reservoir simulated over the year of 2017. The mixing and stratification processes, discussed in this item, can be more clearly distinguished in them.

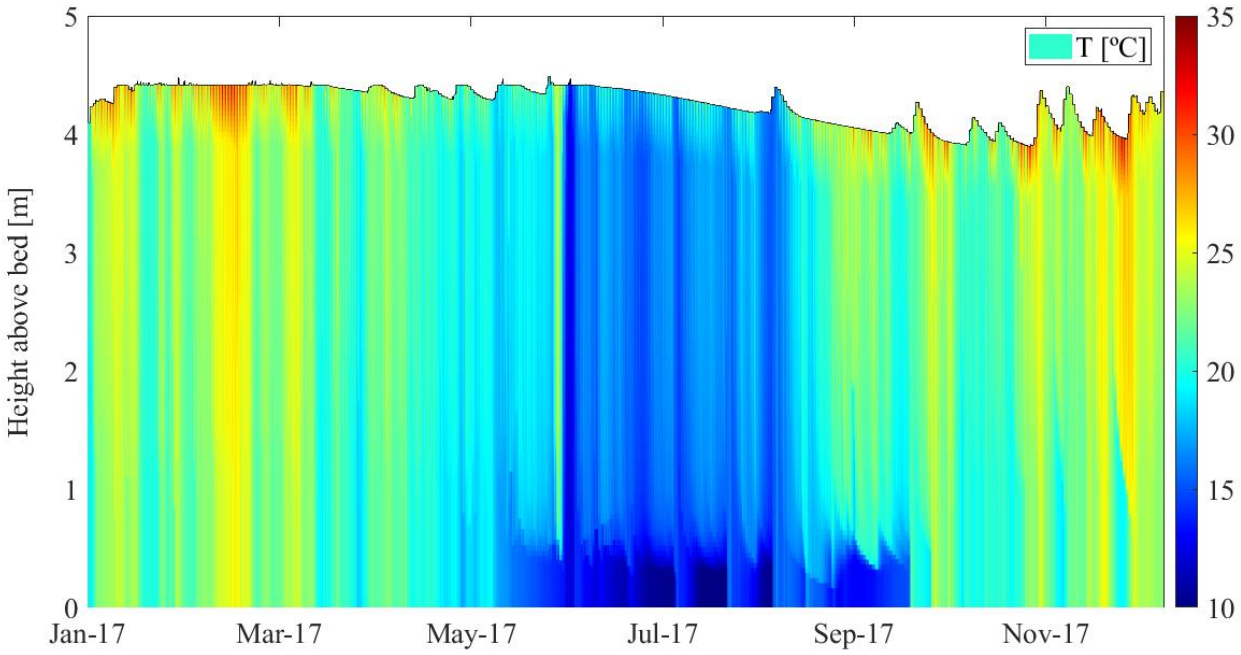


**Figure 56 - Simulated hydraulic and thermal behavior on the Hedberg reservoir (2017). Source: Author.**

## 8.2 CLIMATE CHANGE SCENARIOS

After the calibration and validation of the GLM model, two different climate change scenarios were simulated, an optimistic one and a pessimistic one. The optimistic scenario represents the RCP 4.5, proposed by the IPCC in its Fifth Assessment Report, and predicts the increase of 1.8°C of the global mean temperature by the end of 2100, whilst the pessimistic one represents the RCP 8.5, which predicts an increase of 3.6 °C. Those scenarios were chosen to evaluate the model capabilities and representativeness.

As discussed in 6.4, the climate change scenarios are going to be analyzed for three sets of data: near future (2021 – 2040), middle-term future (2041 – 2070) and distant future (2071 – 2099).

### 8.2.1 Water Balance

The water level is the selected indicator to assess the impact of climate change scenarios over the Hedberg water balance. The main atmospheric variable influencing the indicator is the rain, which presents intense variations when compared to the observed data, with drier and wetter periods.

As discussed in the calibration, the model responds to the input of rain and inflow by varying the level of the lake. However, when above 549 m, the model retrieves all the excess water from the system, imposing an upper limit to the water level representation.

Figure 57 and Figure 58 present the water level variations, in daily average values, for the proposed scenarios.

In the optimistic scenario, the water level varies, alternating between drier and wetter conditions. For the near future, these variations are frequent and balanced. As the simulation reaches the middle-term future and distant future conditions, the alternation between them is less frequent, with longer periods of lower (for example, near 2056 and 2074) or higher (for example, 2049 and 2077) levels characteristics.

The model predicts reductions of up to 0.5 m from the maximum simulated level, with longer periods of reduced levels for the middle-term and distant future.

In the pessimistic scenario, the same tendencies are found, however, with more intense characteristics. Longer periods of low (around 2080, for example) and high (around 2047) levels can be noted, and, in its drier conditions, the descent of the water surface goes up to 1 m from the maximum simulated surface.

These predicted tendencies indicate impacts not only over the amount of water available in the reservoir, but also possible impacts over the thermal regime and water quality characteristics in a shallow lake.

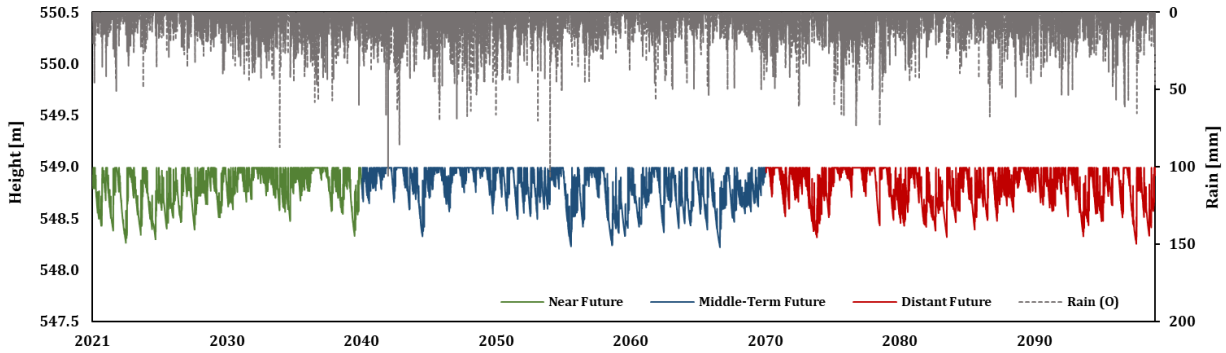


**Figure 57 - Water balance parameters on the Hedberg reservoir for the optimistic (O) simulation. Source: Author.**

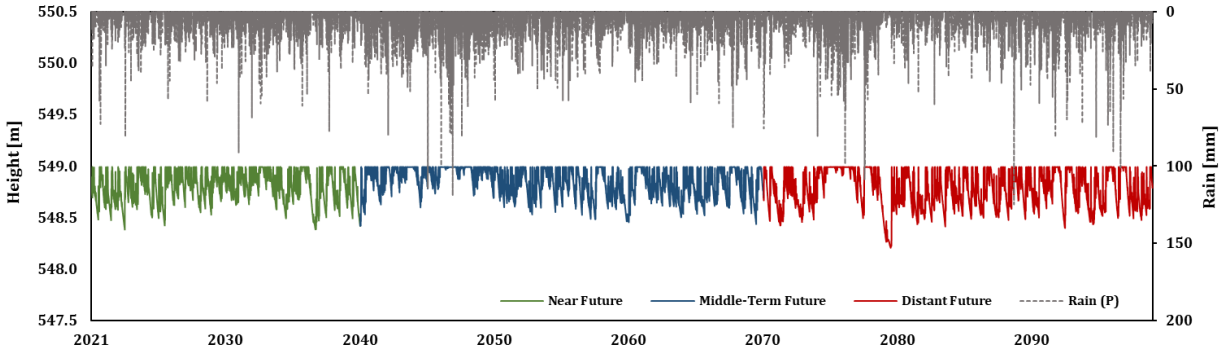


**Figure 58 - Water balance parameters on the Hedberg reservoir for the pessimistic (P) simulation. Source: Author.**

### 8.2.2 Energy Balance

For the energy balance assessment, the applied indicators were: the epilimnion temperature, the hypolimnion temperature, the Schmidt Number and the thermocline depth. They were used to evaluate the impacts of climate change scenarios over the thermal regime of the Hedberg reservoir, a polymictic tropical lake.

Polymictic lakes undergo many mixing events during the year. In these environments, daily variations can have a more relevant role than seasonal ones, in establishing the thermal structure of the lake. Therefore, their stratification events usually last for a few days until external conditions are able to overcome the stability of the density gradient, mixing the water column.

Using annual average values, the epilimnion and hypolimnion temperatures are presented in Figure 59, for the optimistic (circle marker) and pessimistic (squared marker) scenarios. The annual average values of the calibrated period (2017 – 2020) are also plotted for comparison.

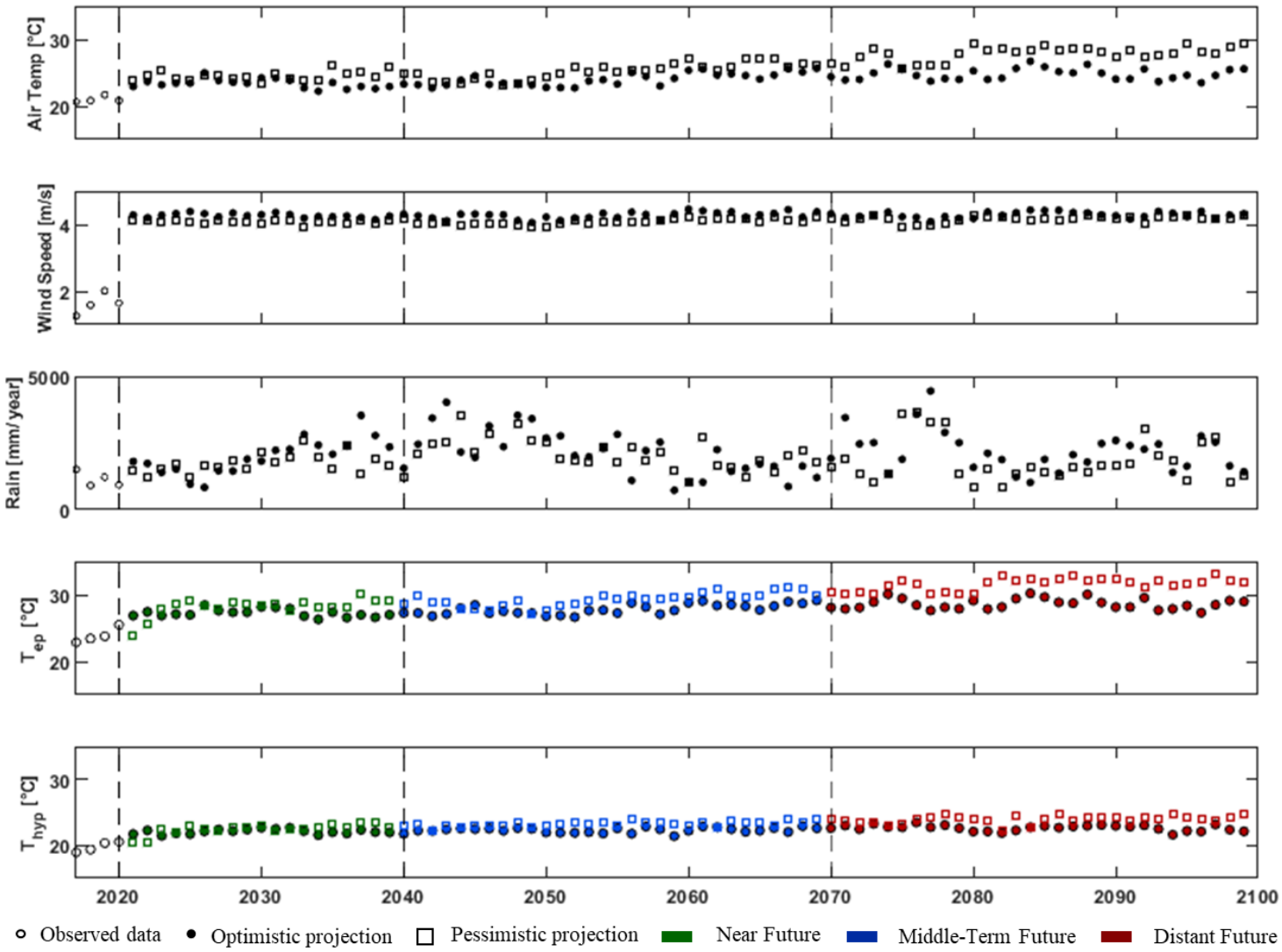


**Figure 59 – Epilimnion and hypolimnion temperatures of the Hedberg reservoir for the optimistic and pessimistic scenarios. Source: Author.**

Figure 59 indicates a trend of increasing temperatures for the upper layer of the reservoir, with lower rising rates in the near future conditions and increasingly higher rates as the simulation progresses.

Moreover, the difference between both climate change scenarios is more pronounced in the distant future conditions, when the pessimistic scenario suggests a temperature increase up to 8 °C from the average value of the observed years, in contrast to only 4 °C for the optimistic scenario.

For the hypolimnion temperature, a lower rising rate than the one related to the surface layer is predicted, with the temperatures rising up to 2 °C in the optimistic scenario and 4 °C in the pessimistic one. The difference between scenarios is also smaller than the one for the epilimnion, with both showing similar tendencies for the near future and middle-term future conditions, until 2050.

The surface layer trends strongly relate to the increase of the air temperature over the simulated period, indicating the influence of the atmospheric variable on the indicator, as expected. Nevertheless, the lower rates predicted for the hypolimnetic temperatures suggests a weaker influence on this parameter, once the bottom layer is affected not only by the atmospheric variables, but also by internal processes of energy propagation and dissipation occurring along the water column and on the soil-water interface.

Another important factor to be considered is the possible underestimation of colder inflows during the climate change scenarios, once the methodological approach applied in this study estimates the temperature of the inflow based solely on the projected air temperature. The impact of other atmospheric variables, their spatial variations and the influence of the catchment area were not considered.

In this context, currents generated by cooler entrainments will be underestimated, as well as their impacts. The occurrence of these currents on the Hedberg reservoir can be observed on the monitored data and its main impacts are related to the cooling of the bottom layer, which helps on the maintenance of long-lasting stratification events, and to the supply of oxygen and nutrients to the hypolimnion.

Therefore, in the light of the identified bias of the projected data, as well as the limitations of the model (which showed higher temperature variations at the bottom layer than in the observed data),

even lower rates may be expected for the increase of the hypolimnion temperature over the simulation period.

These results allude to the occurrence of stronger stratification events in the Hedberg reservoir. The temperature gradient (the difference between the surface and bottom layer temperatures) tends to increase, as temperatures rise at a greater rate on the upper layer than on the bottom one. As a result, the thermal structure establishes a strong density gradient, increasing the buoyancy force within the system.

These conditions can lead to the occurrence of more stable and lasting stratification events. Stronger density gradients are harder to overcome by daily atmospheric variations, which, in the long term, can suggest changes in the mixing regime of a polymictic lake.

In order to better assess the changes on the stratification events over time, the Schmidt Number and the thermocline depth were calculated and evaluated for both scenarios (average annual values) (Figure 60). The calculated values from the calibration period were also presented for comparison purposes.

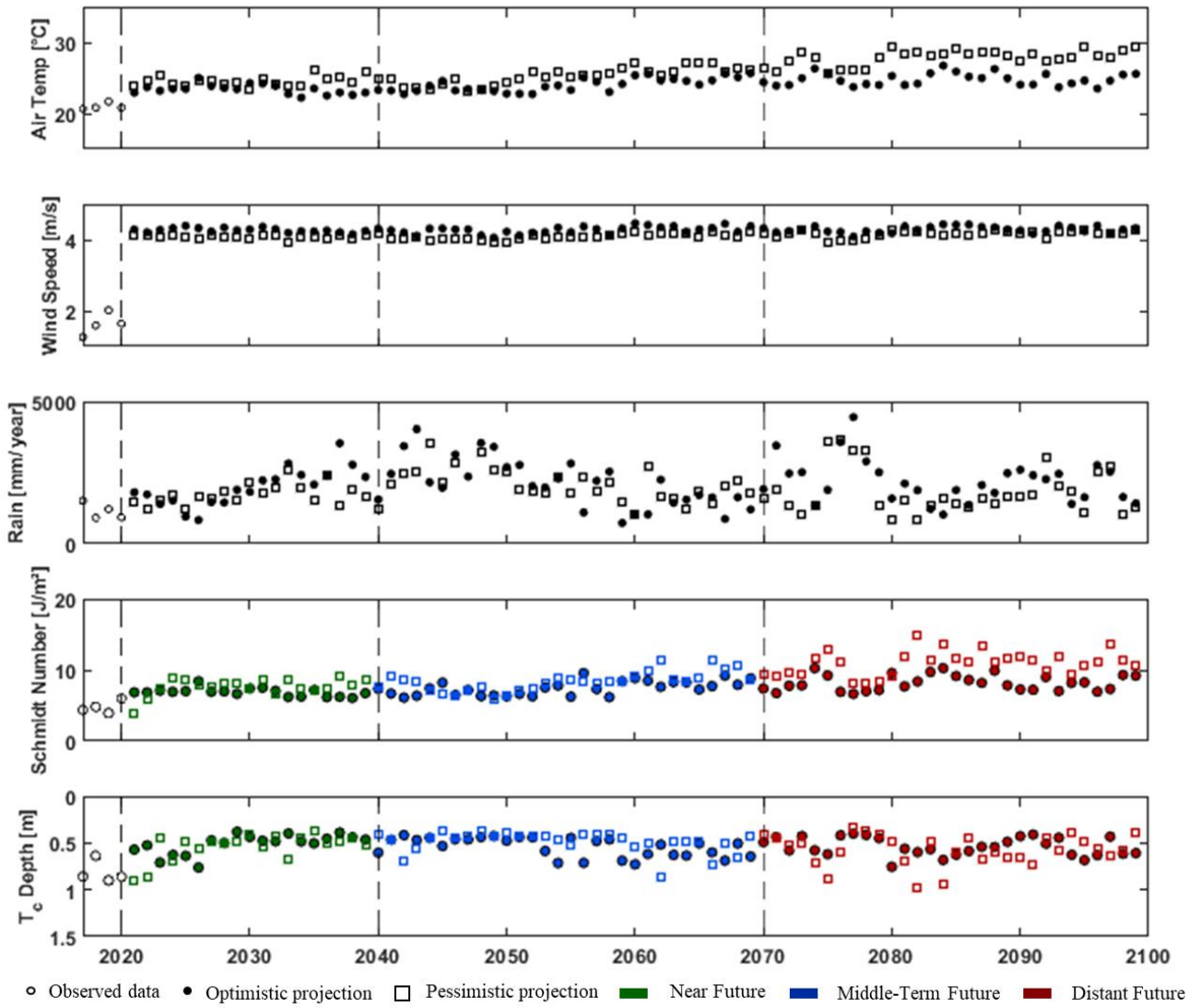


**Figure 60 – Schmidt number and thermocline depth for the Hedberg reservoir, for the optimistic and pessimistic scenarios. Source: Author.**

Throughout the simulated period, both indicators presented an offset in relation to the calibrated data values, in response to the identified bias in the input data. During the near future up to about half of the middle-term future simulation (2055), the Schmidt Number and the thermocline depth indicate an orderly behavior, with small variations and similar tendencies for both climate scenarios.

The Schmidt Number showed averaged values around 7 J/m² (2021), as the calibrated averaged value is 5 J/m². The thermocline depth, on its turn, presented shallower depths for the climate change scenarios, with an average of 0.5 m for the optimistic and pessimistic simulations against 0.8 m from the calibrated years.

Both indicators, however, indicated low changing rates over time, with the Schmidt Number increasing and the thermocline deepening.

From 2055 onward, mainly for the distant future conditions, these trends are better defined. The Schmidt Number indicated an increase in the system energy, with the optimistic scenario presenting Schmidt values up to 10 J/m² and the pessimistic one up to 15 J/m². More frequent and greater variations were also observed as more and more extreme events took place.

For the thermocline depth indicator, results indicated great variations between shallow and deep thermoclines, mainly during the pessimistic simulation. The thermocline deepening occurred in both scenarios, with values varying from 0.5 m to 1 m above the surface.

Shallow thermocline depths suggest the predominance of daily conditions over the thermal structure of the lake, related to a polymictic pattern. The deepening of the thermocline, on the other hand, can indicate the strengthening of stratification conditions, since the seasonal characteristics become more relevant.

These results are coherent with the previous analysis and indicate the strengthening of the water column stability over time, generated by the increase of the density gradient between the upper and bottom layer.

However, to complete the analysis, the lake water balance must be accounted for. The Schmidt Number and the thermocline depth allow the integrated analysis by considering not only the

thermal gradient of the vertical dimension, but also the water level dynamic, with the use of the lake's depth as a parameter.

Figure 57, Figure 58 and Figure 60 indicate that, for the combined occurrence of elevated air temperatures and low rainfall volumes, as the water level of the lake decreased, the stability values increased and the thermocline deepened (for example, around 2073 and 2085), suggesting the occurrence of stronger and lasting stratification events. Whereas, for atmospheric conditions of elevated temperatures and high precipitation rates, the Schmidt Number presented smaller values and the thermocline rose (for example, around 2076 and 2095), indicating lower stability conditions and the predominance of mixed conditions during the year.

Overall, similar trends were observed on both simulated scenarios, for all climate change indicators. The observed trends include:

- Elevation of the lake's temperature, on the upper and bottom layers, with the latter increasing at a lower rate than the first one (epilimnion and hypolimnion temperatures);
- Increase of the density gradient over time;
- Elevation of the lake's overall heat content, resulting on the strengthening of the stratified water column stability (Schmidt Number); and
- More frequent occurrence of deeper thermoclines conditions, suggesting the predominance of long-lasting stratification events, influenced by seasonal variations (thermocline depth).

The optimistic scenario, as expected, presented lower changing rates in relation to the pessimistic one, resulting in smaller variations, for all indicators, between years with different atmospheric conditions. The most extreme values were observed during the pessimistic simulation, in response to the more intense and more frequent extreme atmospheric conditions.

At last, Figure 61 and Figure 62 display the water temperature along the vertical dimension for the optimistic and pessimistic scenarios, over the 79-year period. The discussed conditions can be evaluated on both figures.

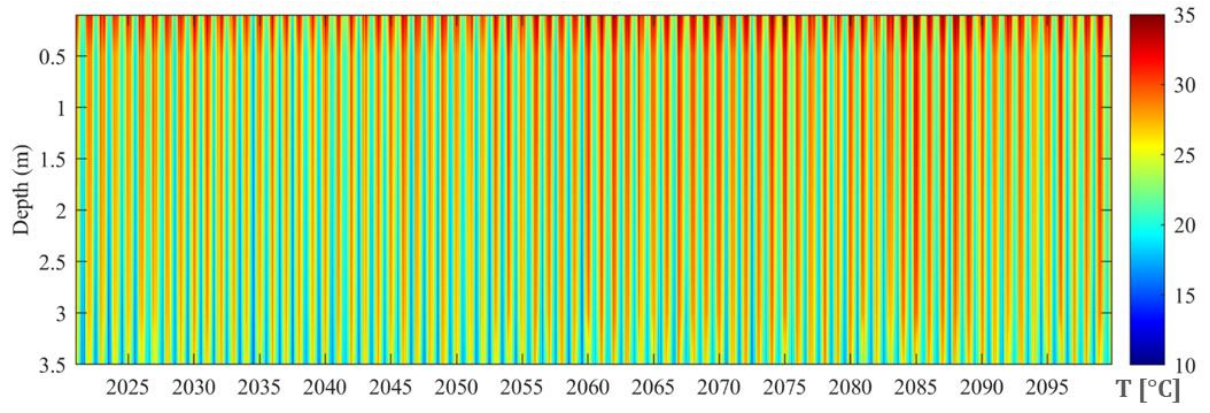


**Figure 61 - Thermal profile for the optimistic scenario (2021 - 2099). Source: Author.**

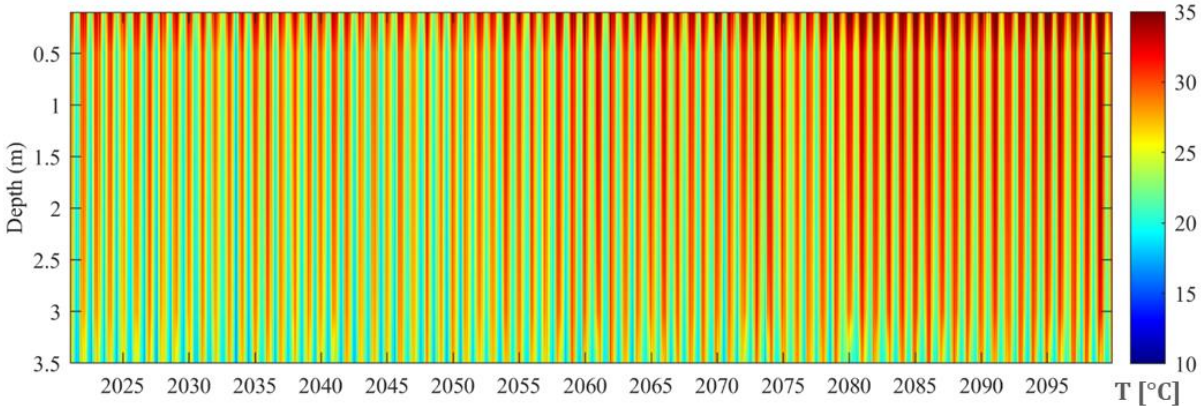


**Figure 62 - Thermal profile for the pessimistic scenario (2021 - 2099). Source: Author.**

Finally, the discussed trends can affect the thermal regime of a polymictic lake, altering its internal dynamics. The simulation results, however, do not indicate changes on the existing regime towards a dimictic one, but rather the intensification of the stratification and mixing processes occurring at the Hedberg reservoir.

These changes, on their own, can have significant impacts over the lake's ecosystem, affecting the distribution of chemicals and biota. Therefore, studying these environments and the impacts of climate change over them is relevant for the decision-making process and local management.

The lower processing effort and less data input required by a one-dimensional model make them a first-choice tool to simulate long period scenarios. In this work, both simulations were performed

in under 5 hours and only required the predicted climate dataset, in hourly values, to generate the optimistic and pessimistic climate change scenarios.

# 9 CONCLUSIONS

In this study, the GLM one-dimensional hydrodynamic model was applied on the Hedberg reservoir to assess the thermal behavior of a small lake under two projected trends of climate change scenarios.

The model was calibrated considering mass and heat balances and validated with atmospheric, hydrological and limnological field data collected along four years of monitoring. The water balance is satisfactorily represented by the modeled spillway and the water level variations, with limitations for the simulation of extreme flood events. For the heat balance, daily and seasonal responses indicated a good agreement with the observed data.

The model performance, limitations and biases in representing the Hedberg reservoir thermal regime were analyzed. During the simulated period, the upper layers temperatures showed the most reliable results, responding to the provided meteorological data and exhibiting similar patterns as the monitoring data. The bottom layer presented greater temperature amplitudes and fluctuations than the observed data, resulting in the overestimation of mixing events by the model, mainly during the wet season.

Most simulated mixing events had a short duration, taking place at the early hours of the day, in response to the surface heat losses during the night, and being dissipated by the morning solar radiation. The described phenomenon is already observed by the monitoring sensors but in lower frequencies than the simulated data. This condition suggests that the calibrated model is biased towards the promotion of mixing events.

However, lasting stratification events, which can be observed during the regional wet season (summer), are also satisfactorily represented by the model. These events are generated by elevated energy conditions (intense radiation, elevated air temperatures and warm inflows) that are maintained during a long period of time, inhibiting short mixing events, once the energy losses of the system are not significant in relation to its energy budget.

Furthermore, the evaluation of the simulation issues can be discussed in the light of the model limitations, for example: the use of a single parameter to represent season-dependent heat fluxes –

the light extinction coefficient (kw) and the soil-sediment thermal conductivity (ksoil) are two parameters highlighted in this study, as they may vary in time to better represent the characteristics of seasonal fluxes –; the use of inflow data at a daily time step, masking the influence of the inflow temperature over a shallow lake dynamic; and the difficulties in calibrating the bottom layer (discussed in other GLM studies).

Beyond the GLM limitations, the 1DV model approach also carries its own limitations, once it disregards important horizontal processes, which may influence the water column, even for a small lake.

Nevertheless, the Hedberg reservoir thermal pattern is considered satisfactorily represented by the GLM model, as its daily and seasonal responses characterize a polymictic lake. Herewith, two climate change projected scenarios were evaluated over a 79-year period.

These scenarios, an optimistic and a pessimistic one, were assessed by five hydrodynamic indicators: water level, epilimnion and hypolimnion temperature, the Schmidt Number and the thermocline depth.

The results indicate the strengthening of the density gradient, as the epilimnion temperatures rise at a greater rate than the hypolimnion, increasing, with it, the stratification stability. By the end of the century, the simulations indicate Schmidt Numbers two to three times higher than the values calculated in the observed period as the thermocline deepens, indicating the occurrence of stronger and lasting stratification events, as more extreme climate conditions occur.

Between both scenarios, the pessimistic one projects the higher occurrence of extreme events, presenting greater variation of the water level, mainly during combined conditions of low rainfall rates and elevated air temperature conditions, which results in greater impacts over the thermal structure of the reservoir.

In conclusion, the model was able to provide an insight of the impact trends of climate change scenarios onto the lentic environment of a small-polymictic-tropical lake, the Hedberg reservoir. The simulated results suggest possible alterations of the thermal regime at place with the intensification of the stratification and mixing processes occurring at the lake towards the predominance of stratified conditions. These conditions can affect chemical and biological characteristics of these environments.

Recommendations for further studies on the Hedberg reservoir focus on improving the GLM bottom layer calibration, to better represent the hypolimnion conditions; addressing the projected climate bias; applying other climate change indicators in order to evaluate the best one for the assessment of a small-polymictic- tropical lake; applying a 2D and 3D model to compare the results; and performing water quality simulation and analyzes. Further studies on lentic environments with similar and distinct characteristics are also recommended.

# 10 ARTICLES AND PUBLICATIONS

National Symposia:

**XXIV SBRH – Simpósio Brasileiro de Recursos Hídricos –November, 2021. Belo Horizonte, Brazil.**

1. Assessing the thermal behavior representation of a small-polimitic-tropical lake with an one-dimensional model. (Barbara P. S. Duarte; Lais F. Amorim; Ariel A. B. Magalhães; Fábio F. Nogueira; Fábio P. Silva; Maria C. S. Pereira; José C. M. Bernardino & José R. S. Martins)
2. Assessment of the effects of hydrological drought periods on seven brazilian reservoirs. (J. Andreza Rigotti; Laura M. V. Soares; Carolina C. Barbosa; Alice R. Pereira; Barbara P. S. Duarte; Gabriela G. N. Sales; Gilliard Nunes; Tiago V. Schuingel; Michael Mannich; Sergio Koide; Tobias B. Bleninger & José R. S. Martins)
3. Export coefficients variability analysis on nonpoint pollution modeling. (Ariel A. B. Magalhães; José R. S. Martins; Barbara P. S. Duarte; Lais F. Amorim; Maria C. S. Pereira; Fábio F. Nogueira & Fábio P. Silva)
4. Utilização de equipamentos de monitoramento de baixo custo para aplicação em corpos hídricos. (Maria Cristina Santana Pereira; Barbara Pozzan Santos Duarte; Fábio Ferreira Nogueira; Fábio Paiva da Silva; Lucas Gobatti; Brenda Chaves Coelho Leite & José Rodolfo Scarati Martins)

International Congresses:

**IEMSS - International Environmental Modelling Software Society. September, 2020. Brussels, Belgium.**

1. Assessing the impacts of climate change scenarios over a tropical lake through a 1DV model. (Barbara Pozzan dos Santos Duarte, Laís Ferrer Amorim, José Rodolfo Scarati Martins)

**vEGU 2021. - European Geoscience Union. Session: 'Lakes and inland seas in a changing environment'. April, 2021. Virtual Conference.**

1. Comparison of 1D and 3D hydrodynamic models on the assessment of climate change scenarios impact over a small tropical lake. (Barbara Pozzan dos Santos Duarte, Laís Ferrer Amorim, José Rodolfo Scarati Martins, José Carlos de Melo Bernardino)
2. Development of thermal stability curve to forecast water column stratification. (Laís Ferrer Amorim, José Rodolfo Scarati Martins, Fábio Ferreira Nogueira, Fábio Paiva da Silva, Barbara Pozzan dos Santos Duarte)

**ASLO - Aquatic Sciences Meeting 2021. June, 2021. Virtual Conference.**

1. Assessing the presence of internal seiches on a small tropical lake through high-frequency monitored data. (Barbara Pozzan dos Santos Duarte, Ariel Ali Bento Magalhães, Laís Ferrer Amorim, Fábio Ferreira Nogueira, Fábio Paiva da Silva, Maria Cristina Santana Pereira, José Rodolfo Scarati Martins e José Carlos de Melo Bernardino)

**PPNW - Physical Processes on Natural Waters. July, 2022. Vancouver, Canada.**

1. Assessment of climate change impacts over the thermal behavior of a small-polymictic-tropical lake. (Barbara Pozzan dos Santos Duarte, José Rodolfo Scarati Martins, Laís Ferrer Amorim, Ariel Ali Bento Magalhães e José Carlos de Melo Bernardino)

**SDEWES – 3rd Latin America Conference on Sustainable Development of Energy, Water and Environment Systems. July, 2022. São Paulo, Brazil.**

1. Comparison between methods to predict climate changes impacts on lakes. (Barbara Pozzan dos Santos Duarte, Laís Ferrer Amorim, José Rodolfo Scarati Martins, Ariel Ali Bento Fábio Ferreira Nogueira, Fábio Paiva da Silva)

# REFERENCES

ADRIAN, R. et al. Lakes as sentinels of climate change. **Limnology and Oceanography,** v. 54, n. 6part2, p. 2283-2297, 2009-11-01 2009. ISSN 0024-3590. Accessed on: 2021-04-01T02:35:15.

AMORIM, L. F. **Hydrodynamics and Water Quality Assessment of Lakes by Thermal Behaviour and Modelling**. 2020. 147 (Doctor of Science). Hydraulic and Environmental Department, School of Engineering, University of São Paulo, São Paulo.

AUGUSTO-SILVA, P. B. et al. Stratification and mixing in large floodplain lakes along the lower Amazon River. **Journal of Great Lakes Research,** v. 45, n. 1, p. 61-72, 2019. ISSN 0380-1330.

BAPTISTELLI, S. C. **Análise crítica da utilização de modelagem matemática na avaliação da dispersão de efluentes leves no litoral da baixada santista (Estado de São Paulo)**. 2008. Universidade de São Paulo

BARBOSA, C. C. Aplicação da modelagem ecológica com foco na dinâmica do fitoplâncton para avaliação da qualidade da água do lago Paranoá-DF. 2015.

BOEHRER, B.; SCHULTZE, M. Stratification of lakes. **Reviews of Geophysics,** v. 46, n. 2, 2008-05-30 2008. ISSN 8755-1209. Accessed on: 2022-08-25T22:14:20.

BRUCE, L. C. et al. A multi-lake comparative analysis of the General Lake Model (GLM): Stress-testing across a global observatory network. **Environmental modelling & software,** v. 102, p. 274-291, 2018. ISSN 1364-8152.

BUECHE, T. et al. glmGUI v1.0: an R-based graphical user interface and toolbox for GLM (General Lake Model) simulations. **Geoscientific Model Development,** v. 13, n. 2, p. 565-580, 2020-02-13 2020. ISSN 1991-9603. Accessed on: 2020-10-07T20:55:05.

CAVALCANTE, M. R. G.; DA CUNHA LUZ BARCELLOS, P.; CATALDI, M. Flash flood in the mountainous region of Rio de Janeiro state (Brazil) in 2011: part I—calibration watershed through hydrological SMAP model. **Natural Hazards,** v. 102, n. 3, p. 1117-1134, 2020-07-01 2020. ISSN 0921-030X. Accessed on: 2022-08-31T20:00:50.

CHAPRA, S. C. **Surface water-quality modeling**. Waveland Press, 2008. ISBN 1478608307.

CHIN, D. A. **Water-quality engineering in natural systems: fate and transport processes in the water environment**. John Wiley & Sons, 2012. ISBN 1118078608.

CHUNG, E. G. et al. A linked hydrodynamic and water quality model for the Salton Sea. The Salton Sea Centennial Symposium, 2008, Springer. p.57-75.

COHEN, J. **Statistical power analysis for the behavioral sciences**. Academic press, 2013. ISBN 1483276481.

COLLINS, W. et al. Development and evaluation of an Earth-System model–HadGEM2. **Geosci. Model Dev. Discuss,** v. 4, n. 2, p. 997-1062, 2011.

DA SILVA, F. P.; MARTINS, J. R. S.; NOGUEIRA, F. F. Impacts of Sea Level Rise on Seawater Intrusion in Cubatão River, Brazil. **Environmental Modeling & Assessment,** v. 25, n. 6, p. 831-841, 2020. ISSN 1573-2967.

DENG, B. et al. Evaluation of the CLM4 Lake Model at a Large and Shallow Freshwater Lake*. **Journal of Hydrometeorology,** v. 14, n. 2, p. 636-649, 2013-04-01 2013. ISSN 1525-755X. Accessed on: 2022-10-17T14:31:08.

FARRELL, K. J. et al. Ecosystem-scale nutrient cycling responses to increasing air temperatures vary with lake trophic state. **Ecological Modelling,** v. 430, p. 109134, 2020-08-01 2020. ISSN 0304-3800. Accessed on: 2020-11-05T15:26:34.

FCTH, F. C. T. D. H. **RA01-1152-15-R1 ETAPA I - Estudo de modelagem para a zona de mistura dos efluentes líquidos no Rio Ipanema e estudos de modelagem numérica para avaliação hidrodinâmica e ecológica do reservatório da Barragem Hedberg**. BRASIL, M. D. 2015.

FENOCCHI, A. et al. Relevance of inflows on the thermodynamic structure and on the modeling of a deep subalpine lake (Lake Maggiore, Northern Italy/Southern Switzerland). **Limnologica,** v. 63, p. 42-56, 2017-03-01 2017. ISSN 0075-9511. Accessed on: 2021-04-01T09:23:35.

FERNÁNDEZ CASTRO, B. et al. Seasonality modulates wind-driven mixing pathways in a large lake. **Communications Earth & Environment,** v. 2, n. 1, 2021-12-01 2021. ISSN 2662-4435. Accessed on: 2022-08-17T15:02:23.

FISCHER, H. B. et al. **Mixing in inland and coastal waters**. San Diego, CAlifornia: Elsevier, 1979. ISBN 0080511775.

GLEON. Global Lake Ecological Observatory Network. 2020. Avaialble at: < https://gleon.org/ >. Accessed on: March 28.

GOLDMAN, C. R.; HORNE, A. J. **Limnology**. McGraw-Hill International Book Company, 1985. Available at: < https://books.google.com.br/books?id=Tt4EzQEACAAJ >.

GOUDSMIT, G.-H. et al. Application of k-ϵ turbulence models to enclosed basins: The role of internal seiches. **Journal of Geophysical Research: Oceans,** v. 107, n. C12, p. 23-1-23-13, 2002-12-01 2002. ISSN 0148-0227. Accessed on: 2021-04-03T06:47:56.

GUTOWSKI, W. J. et al. Temporal–Spatial Scales of Observed and Simulated Precipitation in Central U.S. Climate. **Journal of Climate,** v. 16, n. 22, p. 3841-3847, 2003-11-01 2003. ISSN 0894-8755. Accessed on: 2022-10-04T17:31:44.

HAMILTON, D. P.; SCHLADOW, S. G. Prediction of water quality in lakes and reservoirs. Part I—Model description. **Ecological Modelling,** v. 96, n. 1-3, p. 91-110, 1997. ISSN 0304-3800.

HARRISON, J. A. et al. Modeling phosphorus in rivers at the global scale: recent successes, remaining challenges, and near-term opportunities. **Current opinion in environmental sustainability,** v. 36, p. 68-77, 2019. ISSN 1877-3435.

HENDERSON, S. M.; DEEMER, B. R. Vertical propagation of lakewide internal waves. **Geophysical Research Letters,** v. 39, n. 6, p. n/a-n/a, 2012-03-28 2012. ISSN 0094-8276. Accessed on: 2022-08-25T23:04:42.

HIPSEY, M. R. et al. A General Lake Model (GLM 3.0) for linking with high-frequency sensor data from the Global Lake Ecological Observatory Network (GLEON). **Geoscientific Model Development,** v. 12, n. 1, p. 473-523, 2019. ISSN 1991-959X.

HUANG, A. et al. Evaluating and Improving the Performance of Three 1-D Lake Models in a Large Deep Lake of the Central Tibetan Plateau. **Journal of Geophysical Research: Atmospheres,** v. 124, n. 6, p. 3143-3167, 2019-03-27 2019. ISSN 2169-897X. Accessed on: 2022-10-17T13:55:26.

HUANG, L. et al. The Warming of Large Lakes on the Tibetan Plateau: Evidence From a Lake Model Simulation of Nam Co, China, During 1979-2012. **Journal of Geophysical Research: Atmospheres,** v. 122, n. 24, p. 13,095-13,107, 2017-12-27 2017. ISSN 2169-897X. Accessed on: 2021-03-28T03:32:58.

ICMBIO. **Revisão do Plano de Manejo da Floresta Nacional de Ipanema**. AMBIENTE, M. D. M. Iperó, São Paulo, Brasil. I**:** 306 p. 2017.

IDSO, S. B.; JACKSON, R. D. Thermal radiation from the atmosphere. **Journal of geophysical research,** v. 74, n. 23, p. 5397-5403, 1969. ISSN 0148-0227.

IGB, L.-I. O. F. E. A. I. F. FLake Model. Berlin, Germany, 2021. Avaialble at: < http://www.flake.igb-berlin.de/ >. Accessed on: April 4.

IMBERGER, J. The diurnal mixed layer. **Limnology and oceanography,** v. 30, n. 4, p. 737-770, 1985. ISSN 0024-3590.

_____. Environmental Hydraulics. In: (Ed.). **Environmental Fluid Dynamics**: Elsevier, 2013. p.273-304.

IMBERGER, J.; PATTERSON, J. C. A DYNAMIC RESERVOIR SIMULATION MODEL - DYRESM: 5. In: (Ed.). **Transport Models/Inland & Coastal Waters**: Elsevier, 1981. p.310-361.

_____. Physical limnology. **Advances in applied mechanics,** v. 27, p. 303-475, 1989. ISSN 0065-2156.

IMBODEN, D. M.; WÜEST, A. Mixing Mechanisms in Lakes. In: (Ed.). **Physics and Chemistry of Lakes**: Springer Berlin Heidelberg, 1995. p.83-138.

INMET, I. N. D. M.-. **Normais Climatológicas**. https://bdmep.inmet.gov.br/ (2017 - 2018).

IPCC. **Climate Change 2014: Synthesis Report.** IPCC. Geneva, Switzerland, p.151. 2014

JAMES, A. **An introduction to water quality modelling**. John Wiley and Sons Ltd., 1993. ISBN 0471923478.

JANSSEN, A. B. et al. How to model algal blooms in any lake on earth. **Current opinion in environmental sustainability,** v. 36, p. 1-10, 2019. ISSN 1877-3435.

_____. PCLake+: A process-based ecological model to assess the trophic state of stratified and non-stratified freshwater lakes worldwide. **Ecological modelling,** v. 396, p. 23-32, 2019. ISSN 0304-3800.

_____. Success of lake restoration depends on spatial aspects of nutrient loading and hydrology. **Science of the Total Environment,** v. 679, p. 248-259, 2019. ISSN 0048-9697.

JI, Z.-G. **Hydrodynamics and water quality: modeling rivers, lakes, and estuaries**. John Wiley & Sons, 2008. ISBN 0470241055.

KIRILLIN, G. Modeling the impact of global warming on water temperature and seasonal mixing regimes in small temperate lakes. 2010. ISSN 1797-2469.

KIRILLIN, G. et al. FLake-Global: Online lake model with worldwide coverage. **Environmental Modelling & Software,** v. 26, n. 5, p. 683-684, 2011. ISSN 1364-8152.

KIRILLIN, G.; SHATWELL, T. Generalized scaling of seasonal thermal stratification in lakes. **Earth-Science Reviews,** v. 161, p. 179-190, 2016. ISSN 0012-8252.

LADWIG, R. et al. Lake thermal structure drives interannual variability in summer anoxia dynamics in a eutrophic lake over 37 years. **Hydrology and Earth System Sciences,** v. 25, n. 2, p. 1009-1032, 2021-02-25 2021. ISSN 1607-7938. Accessed on: 2021-03-28T03:37:24.

LAMB, H. **Hydrodynamics**. Cambridge university press, 1993. ISBN 0521458684.

LE MOIGNE, P.; COLIN, J.; DECHARME, B. Impact of lake surface temperatures simulated by the FLake scheme in the CNRM-CM5 climate model. **Tellus A: Dynamic Meteorology and Oceanography,** v. 68, n. 1, p. 31274, 2016. ISSN 1600-0870.

LOPES, J. E. G.; BRAGA JR, B.; CONEJO, J. SMAP--a simplified hydrologic model. **Applied modeling in catchment hydrology/ed. by VP Singh**, 1982.

MACIEL, G. M. et al. Daily Water Flow Forecasting via Coupling Between SMAP and Deep Learning. **IEEE Access,** v. 8, p. 204660-204675, 2020-01-01 2020. ISSN 2169-3536. Accessed on: 2022-08-31T20:00:49.

MAPBIOMAS, P. **Coleção 5 da Série Anual de Mapas de Cobertura e Uso de Solo do Brasil**. https://mapbiomas.org/ 2020.

MARTINS, J. R. S. **HIDRODINÂMICA APLICADA À MODELAGEM DE QUALIDADE DAS ÁGUAS SUPERFICIAIS: Revisão de processos e métodos**. São Paulo: USP, 2017.

MCCUEN, R. H.; KNIGHT, Z.; CUTTER, A. G. Evaluation of the Nash–Sutcliffe efficiency index. **Journal of hydrologic engineering,** v. 11, n. 6, p. 597-602, 2006. ISSN 1084-0699.

MENDOZA, M. U. et al. Small maar lakes of Luzon Island, Philippines: Their limnological status and implications on the management of tropical lakes—A review. **Philippine Journal of Science,** v. 148, n. 3, p. 565-578, 2019. ISSN 0031-7683.

MENEZES, R. F. et al. Differences in food webs and trophic states of Brazilian tropical humid and semi-arid shallow lakes: implications of climate change. **Hydrobiologia,** v. 829, n. 1, p. 95-111, 2019. ISSN 1573-5117.

MESINGER, F. et al. An upgraded version of the Eta model. **Meteorology and Atmospheric Physics,** v. 116, n. 3-4, p. 63-79, 2012-05-01 2012. ISSN 0177-7971. Available at: < http://hdl.handle.net/11380/727853 >. Accessed on: 2020-11-23T23:59:03.

MIRONOV, D. V. **Parameterization of lakes in numerical weather prediction: Description of a lake model**. DWD, 2008.

MOOIJ, W. M. et al. Predicting the effect of climate change on temperate shallow lakes with the ecosystem model PCLake. In: (Ed.). **Shallow Lakes in a Changing World**: Springer, 2007. p.443-454.

NAGHIB, A.; PATTERSON, J.; LEI, C. Natural convection induced by absorption of solar radiation in the near shore region of lakes and reservoirs: Experimental results. **Experimental Thermal and Fluid Science,** v. 90, p. 101-114, 2018. ISSN 0894-1777.

O'REILLY, C. M. et al. Climate change decreases aquatic ecosystem productivity of Lake Tanganyika, Africa. **Nature,** v. 424, n. 6950, p. 766-768, 2003. ISSN 1476-4687.

_____. Rapid and highly variable warming of lake surface waters around the globe. **Geophysical Research Letters,** v. 42, n. 24, p. 10,773-10,781, 2015-12-28 2015. ISSN 0094-8276. Accessed on: 2021-04-01T01:19:54.

PARTON, W. J.; LOGAN, J. A. A model for diurnal variation in soil and air temperature. **Agricultural meteorology,** v. 23, p. 205-216, 1981. ISSN 0002-1571.

PERROUD, M.; GOYETTE, S. Impact of warmer climate on Lake Geneva water-temperature profiles. 2010. ISSN 1797-2469.

PINTO, A. A. D. S. Avaliação da influência da precipitação e temperatura do ar na dinâmica térmica do reservatório do Descoberto-DF por meio do modelo GLM. 2018.

POLLI, B. A.; BLENINGER, T. Comparison of 1D and 3D reservoir heat transport models and temperature effects on mass transport. **RBRH,** v. 24, 2019-01-01 2019. ISSN 2318-0331. Accessed on: 2022-10-17T14:07:40.

PRATS, J.; DANIS, P.-A. An epilimnion and hypolimnion temperature model based on air temperature and lake characteristics. **Knowledge & Management of Aquatic Ecosystems**, n. 420, p. 8, 2019-01-01 2019. ISSN 1961-9502. Accessed on: 2022-10-17T13:36:13.

PUJONI, D. G. F. Padrões Espaço-Temporais da comunidade planctônica do complexo lacustre do Médio Rio Doce. 2015.

R CORE TEAM. **R: A Language and Environment for Statistical Computing**. Vienna, Austria: R Foundation for Statistical Computing 2020.

READ, J. S. et al. Derivation of lake mixing and stratification indices from high-resolution lake buoy data. **Environmental Modelling & Software,** v. 26, n. 11, p. 1325-1336, 2011-11-01 2011. ISSN 1364-8152. Accessed on: 2021-03-25T09:04:51.

_____. Simulating 2368 temperate lakes reveals weak coherence in stratification phenology. **Ecological Modelling,** v. 291, p. 142-150, 2014. ISSN 0304-3800.

REICHERT, P. AQUASIM-A tool for simulation and data analysis of aquatic systems. **Water Science and Technology,** v. 30, n. 2, p. 21, 1994. ISSN 0273-1223.

ROCHA JUNIOR, C. A. N. D. et al. Water volume reduction increases eutrophication risk in tropical semi-arid reservoirs. **Acta Limnologica Brasiliensia,** v. 30, 2018. ISSN 2179-975X.

SABER, A.; JAMES, D. E.; HAYES, D. F. Effects of seasonal fluctuations of surface heat flux and wind stress on mixing and vertical diffusivity of water column in deep lakes. **Advances in water resources,** v. 119, p. 150-163, 2018. ISSN 0309-1708.

SAHOO, G. B. et al. The response of Lake Tahoe to climate change. **Climatic Change,** v. 116, n. 1, p. 71-95, 2013-01-01 2013. ISSN 0165-0009. Accessed on: 2021-04-03T03:55:54.

SALES, G. G. N. Water quality modeling in a subtropical water supply reservoir. p. 83, 2020a.

_____. Water quality modeling in a subtropical water supply reservoir. 2020b.

SALORANTA, T.; ANDERSEN, T. MyLake (v. 1.1): Technical model documentation and user's guide for version 1.1. 2004. ISSN 8257745200.

SALORANTA, T. M.; ANDERSEN, T. MyLake—A multi-year lake simulation model code suitable for uncertainty and sensitivity analysis simulations. **Ecological modelling,** v. 207, n. 1, p. 45-60, 2007. ISSN 0304-3800.

SHATWELL, T.; THIERY, W.; KIRILLIN, G. Future projections of temperature and mixing regime of European temperate lakes. **Hydrology and Earth System Sciences,** v. 23, n. 3, p. 1533-1551, 2019-03-18 2019. ISSN 1607-7938. Available at: < https://doaj.org/article/f12ba47ec4f346dd9129918814250b6f >. Accessed on: 2022-10-17T12:59:13.

SILVA, T. et al. Urban stormwater runoff impacts on the ecosystem of a tropical lake. 36th IAHR WORLD CONGRESS, The Hague, 2015.

SIMPSON, J. H. et al. Dissipation and mixing during the onset of stratification in a temperate lake, W indermere. **Limnology and Oceanography,** v. 60, n. 1, p. 29-41, 2015. ISSN 0024-3590.

SOARES, L. M. V. Modelagem hidrodinâmica e ecológica de reservatório tropical em condição de escassez hídrica. 2018.

SOARES, L. M. V. et al. **Modelagem de Reservatório Metropolitano Destinado à Produção de Água Potável: Uma ferramenta para avaliar os impactos da escassez hídrica sobre a hidrodinâmica de ambientes lênticos**: XXII SIMPÓSIO BRASILEIRO DE RECURSOS HÍDRICOS, Florianópolis 2017.

_____. A parameterization strategy for hydrodynamic modelling of a cascade of poorly monitored reservoirs in Brazil. **Environmental Modelling & Software,** v. 134, p. 104803, 2020. ISSN 1364-8152.

SUMKA, M. G. **Climate change impacts on a eutrophying lake: Cultus Lake, British Columbia, Canada**. 2017. University of British Columbia

TALLING, J. Environmental controls on the functioning of shallow tropical lakes. **Hydrobiologia,** v. 458, n. 1, p. 1-8, 2001. ISSN 1573-5117.

**THE MATHWORKS, I. MATLAB M.The language of technical computing**

**.** 2012.

THIERY, W. et al. Understanding the performance of the FLake model over two African Great Lakes. **Geoscientific Model Development,** v. 7, n. 1, p. 317-337, 2014. ISSN 1991-959X.

THOMPSON, R.; IMBERGER, J. Response of a numerical model of a stratified lake to wind stress. Proc. 2nd Int. Symp. Stratified Flow, Trondheim, Norway, 1980. p.562-570.

TOFFOLON, M. et al. Prediction of surface temperature in lakes with different morphology using air temperature. **Limnology and Oceanography,** v. 59, n. 6, p. 2185-2202, 2014-11-01 2014. ISSN 0024-3590. Available at: < https://www.dora.lib4ri.ch/eawag/islandora/object/eawag%3A7793/datastream/PDF/view >. Accessed on: 2022-07-01T13:59:16.

TUNDISI, J. G.; TUNDISI, T. M. **Limnologia**. Oficina de textos, 2008. ISBN 8579751012.

UWA, U. O. W. A. General Lake Model (GLM). Australia, 2021. Avaialble at: < https://aquatic.science.uwa.edu.au/research/models/ GLM / >. Accessed on: 2021.

VAREJÃO-SILVA, M. A. **Meteorologia e climatologia**. INMET Brasília, 2000.

WAICHLER, S. R.; WIGMOSTA, M. S. Development of Hourly Meteorological Values From Daily Data and Significance to Hydrological Modeling at H. J. Andrews Experimental Forest. **Journal of Hydrometeorology,** v. 4, n. 2, p. 251-263, 2003-04-01 2003. ISSN 1525-755X. Accessed on: 2022-07-01T13:43:35.

WATANABE, S. et al. MIROC-ESM 2010: Model description and basic results of CMIP5-20c3m experiments. **Geoscientific Model Development,** v. 4, n. 4, p. 845, 2011. ISSN 1991-962X.

WEINSTOCK, J. Vertical turbulence diffusivity for weak or strong stable stratification. **Journal of Geophysical Research: Oceans,** v. 86, n. C10, p. 9925-9928, 1981. ISSN 0148-0227.

WHITE, F. M. **Mecânica dos Fluidos**. Porto Alegre: AMGH, 2011.

WOOLWAY, R. I. et al. Atmospheric stilling leads to prolonged thermal stratification in a large shallow polymictic lake. **Climatic Change,** v. 141, n. 4, p. 759-773, 2017. ISSN 0165-0009.

WOOLWAY, R. I.; MERCHANT, C. J. Worldwide alteration of lake mixing regimes in response to climate change. **Nature Geoscience,** v. 12, n. 4, p. 271-276, 2019. ISSN 1752-0908.

WÜEST, A.; LORKE, A. Small-scale hydrodynamics in lakes. **Annual Review of fluid mechanics,** v. 35, n. 1, p. 373-412, 2003. ISSN 0066-4189.

ZHANG, M. et al. Exploring responses of lake area to river regulation and implications for lake restoration in arid regions. **Ecological Engineering,** v. 128, p. 18-26, 2019. ISSN 0925-8574.